The Pennsylvania State University

The Graduate School

Department of Materials Science and Engineering

EPITAXIALY STRAINED

STRONTIUM TITANATE

A Thesis in

Materials Science and Engineering

by

Michael David Biegalski

Submitted in Partial Fulfillment
of the Requirements
for the Degree of

Doctor of Philosophy

May 2006

The thesis of Michael D. Biegalski was reviewed and approved* by the following:

Susan Trolier-McKinstry
Professor of Ceramic Science and Engineering
Thesis Co-Advisor
Co-Chair of Committee

Darrell G. Schlom
Professor of Materials Science and Engineering
Thesis Co-Advisor
Co-Chair of Committee

Qiming Zhang
Professor of Electrical Engineering

Venkatraman Gopalan
Associate Professor of Materials Science and Engineering

Long-Qing Chen
Professor of Materials Science and Engineering

James P. Runt
Professor of Polymer Science
Associate Head for Graduate Studies, Materials Science and Engineering

*Signatures are on file in the Graduate School

ABSTRACT

Although $SrTiO_3$ is normally not ferroelectric at any temperature, predictions that predate this thesis based on thermodynamic analysis concluded that a biaxial tensile strain of order 1% would shift the paraelectric-to-ferroelectric transition temperature (T_c) of $SrTiO_3$ to the vicinity of room temperature. In practice, uniformly straining $SrTiO_3$ or related perovskite ferroelectrics to such strain levels is challenging. Nonetheless, using epitaxy and the misfit strain imposed by an underlying substrate, $SrTiO_3$ thin films were strained to percent levels—far beyond where they would crack in bulk. Epitaxial ferroelectric films are often grown to thicknesses greatly exceeding their critical values, resulting in undesirable relaxation toward a zero-strain state by the introduction of dislocations. Dislocation densities of $\sim 10^{11}$ cm^{-2} are common in epitaxial ferroelectric films grown on lattice-mismatched substrates, and the resulting inhomogeneous strain can smear out the ferroelectric phase transition.

High levels of strain coupled with excellent structural quality were achieved by epitaxial growth on the new substrates $DyScO_3$ and $GdScO_3$. Before this work there were no commercial substrates available with lattice parameters in the 3.90 to 3.98 Å range. Initial work focused on characterization of these substrates. The average thermal expansion coefficients of $DyScO_3$ and $GdScO_3$ were determined by high temperature x-ray diffraction to be 8.4 ppm/K and 10.9 ppm/K, respectively, and no phase transitions were detected from room temperature to 1273 K. These thermal expansion coefficients

are similar to $SrTiO_3$ (and many other perovskites) which should facilitate epitaxial growth of perovskite thin films on them.

The dielectric properties of $GdScO_3$ and $DyScO_3$ were also determined to ensure that dielectric characterization of the films would not be riddled by artifacts induced by the substrate. It was found that these materials have dielectric constants ranging from 19 to 36, depending on direction, with no dielectric anomalies from 4.2 K to 450 K and with very little temperature dependence and low losses. Thus, these substrates enable the dielectric properties of films to be measured without interference from the substrate.

The dielectric properties of the strained (001) $SrTiO_3$ thin films on (101) $DyScO_3$ and $GdScO_3$ were examined using interdigitated electrodes. The films grown on $DyScO_3$ (strain $\approx 1\%$) substrates showed a frequency-dependent permittivity maximum near 250 K that is well fit by the Vogel-Fulcher equation. Both this and the field-cooling data indicate that these films are not normal ferroelectrics, but are instead relaxor ferroelectrics. A clear polarization hysteresis is observed in these films below the permittivity maximum, with an in-plane remanent polarization of 10 $\mu C/cm^2$ at 77 K. Similar effects were found in the $SrTiO_3$ films grown on $GdScO_3$, however, the T_{max} was shifted to even higher temperatures (~350 K) due to the higher strain state (strain $\approx 1.6\%$). The polarization at room temperature was found to be nearly 10 $\mu C/cm^2$. The high T_{max} in these films is consistent with the biaxial tensile strain state, while the superimposed relaxor behavior is likely due to defects.

The strain in these films eventually decreases, as the films are grown thicker, due to the introduction of dislocations. In order to determine the critical thickness for strain

relaxation, the strain state and structural perfection of films with thicknesses ranging from 50 Å to 1000 Å were examined using x-ray scattering. The critical thickness at which misfit dislocations were introduced was found to be between 350 Å and 500 Å. Only a modest amount of relaxation was seen in films exceeding the critical thicknesses, even after high temperature annealing at 750 °C. The strain relaxed anisotropically, with more relaxation occurring along the longer in-plane axis of the orthorhombic substrate. It was also found that these films have the narrowest rocking curves (full width at half maximum) ever reported for any heteroepeitaxial oxide film (0.0018°). These $SrTiO_3$ films show structural quality more typical of semiconductor materials than perovskite materials; their structural relaxation behavior is also comparable to that of semiconductor materials.

With the discovery of the anisotropy in the in-plane strain state, the in-plane anisotropy of the dielectric properties was explored. The dielectric permittivity showed two distinct transitions along the in-plane [100] and [010] $SrTiO_3$ directions. Both transitions were sampled at intermediate in-plane directions. A switchable polarization also developed at different temperatures for the [100] and [010] directions. These factors, coupled with the asymmetry in the thermal hysteresis behavior in the permittivity and the asymmetry of field cooling data, confirm that these are two separate transitions. The in-plane anisotropy is attributed to the non-uniform biaxial strain present in these films.

TABLE OF CONTENTS

LIST OF FIGURES

LIST OF TABLES

ACKNOWLEDGEMENTS

I must start by thanking my parents and family. Without the support of my family I could not have persevered over these seven years. They have always been supportive of me and were always ready to help. I greatly appreciate all their encouragement and assistance. I must also thank my fiancée, Amy, who has cheered me on through this process and has read this thesis almost as many times as me.

I have been very fortunate in my time at Penn State to have worked with a long list of exceptional people during the course of my studies. I have to first thank the three major players who mentored me through this process. They have offered me many invaluable opportunities that very few graduate students have been afforded. They have also given of themselves going far beyond what was required for my benefit. My development as a scientist and as a person has been a direct result of the tireless efforts of these individuals. First I have to thank Susan Trolier-McKinstry. She has helped me throughout my seven years at Penn State. She has given me the support and guidance that I needed when I needed it. She has always been there to help me and I can not remember her ever refusing any request for help that I have made. I also have to thank Darrell Schlom for his dedication and unwavering efforts. We have had many late night discussions that lasted into the wee hours of the morning. Darrell has also provided me with many opportunities to grow and enhance my understanding of the subject. I also

have to thank Stephen Streiffer for his guidance in x-ray diffraction and for making my visits to Argonne National Laboratory as painless and productive as possible.

There have been many collaborators along the way that have contributed to this work. Without these contributions the knowledge gained in this work would have be significantly reduced. The collaborators in this work were (in no particular order): Alok Sharan and Arvind Rao in Prof. Goplan's group at Penn State that performed second harmonic generation experiments; Yulan Li and Prof. Chen at Penn State that did phenomenological modeling of the Strontium Titanate system; the group at Argonne National Lab that helped during all the 24/7 synchrotron experiments: Mark Zurbuchen, Jeff Eastman, Paul Fuoss, Carol Thompson, B. Stevenson and Dillon Fong, I especially have to thank Dillon for all the help in modeling and interpreting the synchrotron data; Vladimir Sherman and Prof. Tagantsev of EPFL who did the dielectric modeling of my first dielectric measurements and taught me how to do the modeling so I could model the rest of the dielectric measurements; Marylin Hawley of LANL who graciously taught me how to use her AFM's and helped me avoid the pit falls in the measurements; and Reinhard Uecker and Peter Reiche at the Institute for Crystal Growth in Berlin who grew all the substrates used in this work.

Thanks to all the people at MRL and MRI that helped me in this endeavor. The staff at MRL and MRI helped to make most of the equipment work, most of the time. Thanks to the technicians and machinist that were able to help and hurry things when we had deadlines.

And thanks to all my friends, without whom I could not have survived my time at Penn State. These people made graduate school bearable, if not a little fun. I must acknowledge the State College area with its thousands of miles of back roads and hundreds of miles of trail right at my door step. I am sad to think I will never live in a place that is as nice to ride bikes in as State College.

Chapter 1

Introduction and Statement of Work

1.1 Introduction

Ferroelectrics are technologically important for capacitors, sensors, actuators, electro-optics, and non-volatile memory. These materials have many desirable properties as electronic materials. For example, their high dielectric constant over a broad temperature range makes them very attractive for charge storage devices, i.e. capacitors. This is a multibillion-dollar industry with a production on the order of 10^{12} units per year.[1] These materials also have very high piezoelectric coefficients, making them useful as actuators and sensors. Ferroelectric films are used as actuators in many micro-electro mechanical systems (MEMS) because of the large, low hysteresis displacements achievable with modest electric fields. Bulk ferroelectrics are also employed in micropositioners, ink jet printers, fuel injectors, and high-speed valves for automotive applications.[2] Likewise, ferroelectrics are prevalent in sensors, including sonar systems, and ultrasound sensors.

In many cases the ferroelectric transition temperature is manipulated in order to optimize the desired properties. One widely utilized means of accomplishing this is chemical doping. However, another possible tool is the application of mechanical strain. Because most ferroelectrics are ferroelastic, they are strongly affected by strain.[3-13] It has been shown for many materials undergoing cooperative phenomena that boundary

constraints and surfaces can induce very different properties in thin films as compared to bulk materials. For example, a ferromagnetic spin can be induced in thin films of $LaFe_{0.5}Cr_{0.5}O_3$, a material that in its bulk form is always paramagnetic.[14] Significant property changes have also been found in high temperature superconductors where the critical temperature of $(La_{1.9}Sr_{0.1})CuO_4$ can be doubled in thin films.[15] In ferroelectric materials, surface and boundary constraint effects are also important.[3-6,8,13,16,17] Large changes in the dielectric constant, ferroelectric transition temperature, transition order, and piezoelectric coefficients are all manifested. Through epitaxy, homogeneous strains can be induced in thin films at such high levels that they would lead to mechanical failure in bulk materials.

Given its high dielectric constant and low losses, $SrTiO_3$ has been investigated as a tunable dielectric for microwave applications.[18] $SrTiO_3$ is an incipient ferroelectric that does not undergo a ferroelectric transition but approaches one as it is cooled towards 0 K. Pertsev *et al.* predicted that strain would have a large effect on $SrTiO_3$.[3] They predicted that bi-axial strain could not only induce a ferroelectric state, but also move the paraelectric to ferroelectric transition to room temperature.[3] In this work we examine the effects of epitaxial strain on $SrTiO_3$ films. Of interest was verification of the thermodynamic predictions on the stability of the ferroelectric phase, as well as an understanding of the property consequences.

1.2 Statement of Problem

In order to utilize epitaxial strain, new substrates had to be developed since there were no commecial substrates with lattice constants close to $SrTiO_3$. Thus the first part of the work was to characterize candidate substrates to ensure that high quality epitaxial

films can be grown and that electrical characterization is possible. This entails determining the thermal expansion of the substrate to ensure there are no anomalies that would cause problems with the growth of commensurate epitaxial films. The dielectric properties of these materials also must be determined to ensure that no artifacts from the substrates complicate interpretation of the measurements made on epitaxial films. The effectiveness of these materials as substrates for most of the perovskite films will also be determined.

The nature of the induced transition in $SrTiO_3$ on $DyScO_3$ shown by Haeni *et al.* (Fig. 1.1) also needs to be determined to fully characterize the effects of strain on the ferroelectric properties of $SrTiO_3$. It has been shown that there is a peak in the permittivity at 260 K and a breaking of the local symmetry in this same temperature region detected by secondary harmonic generation. However, ferroelectricity of the system has not been directly measured. In this work the switching of the polarization will be investigated to determine if the material is a ferroelectric. The frequency dielectric permittivity as a function of temperature, nature of the phase transitions, and the effects of strain and applied dc bias on the permittivity and polarization of the system will be evaluated.

Although strained films may have extremely good properties and many potential applications, there is a limit to the thickness that the films can be grown and remain homogeneously strained. Once the films reach a critical thickness the strain energy becomes high enough to introduce misfit dislocations. These misfit dislocations serve to reduce the strain state of the material. Therefore, in this work the critical thickness is determined, and the amount of strain relation is determined for thicker films. The manner

of this strain reduction is also explored to determine how quickly these strains are reduced and the effects of the structural relaxation on the properties.
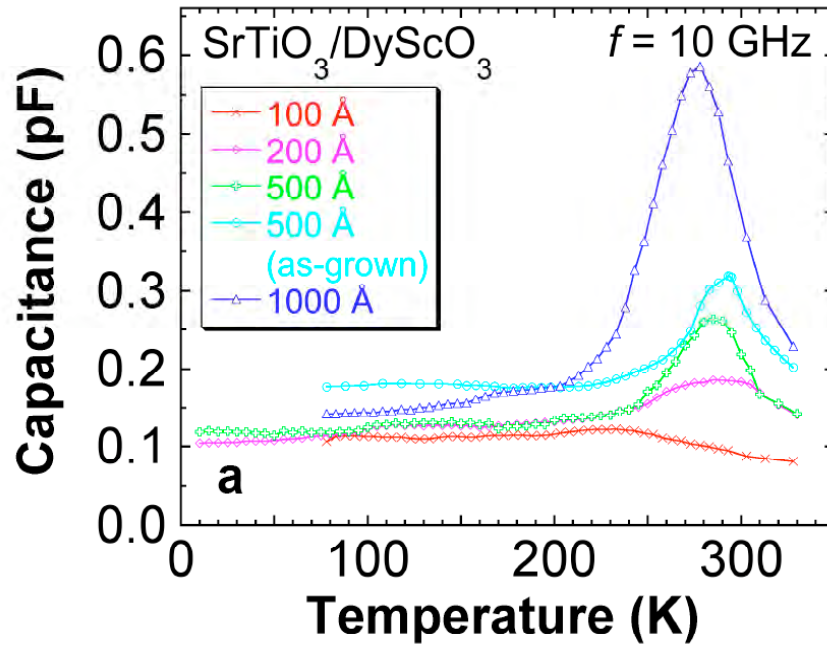
Fig. 1.1 Capacitance, measured at 10 GHz, as a function of temperature for various thicknesses of $SrTiO_3$ grown on $DyScO_3$ substrates. The films were annealed at 700 °C for 1 h in 1 atm of air after growth, except the one marked "as-grown." [13]

References

[1] M. Randall. KEMET Electronics (Private Communication).

[2] Robert Bosch GmbH, Stuttgart, Germany.

[3] N. A. Pertsev, A. K. Tagantsev, and N. Setter, Phys. Rev. B **61**, R825 (2000); **65**, 219901(E) (2002).

[4] A. F. Devonshire, Phil. Mag Suppl. **3**, 85 (1954).

[5] H. Uwe and T. Sakudo, Phys. Rev. B **13**, 271 (1976).

[6] N. A. Pertsev, A. G Zembilgotov, and A. K. Tagantsev, Phys. Rev. Lett. **80**, 1988 (1998).

[7] K. Abe, N. Yanase, K. Sano, M. Izuha, N. Fukushima, and T. Kawakubo, Integr. Ferroelectr. **21**, 197 (1998).

[8] S.K. Streiffer, J.A. Eastman, D.D. Fong, C. Thompson, A. Munkholm, M.V. Ramana Murty, O. Auciello, G.R. Bai, and G.B. Stephenson, Phys. Rev. Lett. **89**, 067601 (2002).

[9] Q. Gan, R. A. Rao, C. B. Eom, J. L Garrett, and M. Lee, Appl. Phys. Lett. **72**, 978 (1998).

[10] J. M. Lock, Proc. R. Soc. Lond. A **208**, 391 (1951).

[11] H. Sato, and M. Naito, Physica C **274**, 221 (1997).

[12] I. Bozovic, G.Logvenov, I. Belca, B. Narimbetov and I. Sveklo, Phys. Rev. Lett. **89**, 107001 (2002).

[13] J. H. Haeni, P. Irvin, W. Chang, R. Uecker, P. Reiche, Y. L. Li, S. Choudhury, W. Tian, M. E. Hawley, B. Craigo, A. K. Tagantsev, X. Q. Pan, S. K. Streiffer, L. Q. Chen, S. W. Kirchoefer, J. Levy, and D. G. Schlom, Nature **430**, 758 (2004).

[14] K. Ueda, H. Tabata, and T. Kawai, Science **280**, 1064 (1998).

[15] J.-P. Locquest, J. Perret, J. Fompeyrine, E. Machler, J.W. Seo, and G. Tendeloo, Nature **394**, 453 (1998).

[16] K. J. Choi, M. Biegalski, Y. L. Li, A. Sharan, J. Schubert, R. Uecker, P. Reiche, Y. B. Chen, X. Q. Pan, V. Gopalan, L.-Q. Chen, D. G. Schlom, and C. B. Eom, Science, **306**, 1005 (2004).

[17] J.-F. Li, D.D. Viehland, T. Tani, C.E. Lakeman, and D.A. Payne, J. Appl. Phys. **75** 442 (1994).

[18] K.A. Muller, W. Berlinger, and H. Bukard, Phys. Rev. B **19**, 3593 (1973).

Chapter 2

Background

2.1 Ferroelectric Materials

A material is considered to be ferroelectric when it has a spontaneous polarization that can be permanently reoriented between crystallographically defined directions with a realizable electric field.[1,2,3] This definition requires that ferroelectrics are a subset of the pyroelectric crystal classes, meaning that they will possess a temperature-dependent spontaneous electric dipole moment. Valasek first discovered ferroelectric materials in the 1920's.[1] He found that the polarization of Rochelle salt ($NaKC_4H_4 \cdot 4H_2O$) could be reversed by the application of an electric field. He also observed that many of the dielectric properties of this crystal were similar in nature to the ferromagnetic properties of iron, and hence the name ferroelectrics. Proper ferroelectric materials show both a polarization-electric field hysteresis loop and a large temperature dependent maximum in the dielectric constant.[2] The temperature at which this dielectric maxima occurs is the Curie temperature; above this temperature the material is a paraelectric, and below the Curie temperature the material is ferroelectric. In the paraelectric state the temperature dependence of the dielectric constant, K, obeys the Curie-Weiss law:

$$K = \frac{C}{T - T_0} \qquad \qquad \text{Eq. 2.1}$$

where C is the Curie constant, and T_0 is the Curie-Weiss temperature.[2] In materials that undergo a second order transition the Curie-Weiss temperature agrees very well with the

transition temperature T_C. However, in ferroelectrics that undergo a first order transition T_C is larger than T_0 (Fig. 2.1). The classification of these transitions as first or second order is defined by the partial derivative of the Gibbs free energy (G) at the phase transition.[1,4] For a second order transition the polarization changes continuously at the phase transition, but for a first order transition the polarization and strain change discontinuously, for an nth order phase transition the nth order derivative of G is discontinuous at the transition temperature.[2]

Ferroelectrics are characterized by their reorientable electric dipoles. In the presence of an electric field of sufficient magnitude, these dipoles will tend to align in a direction close to that of the applied electric field (though constrained by the symmetry and structure of the crystal). The regions where the dipoles are all aligned in the same direction (sometimes with some modulation) are called domains, in analogy to magnetic domains. Starting with a material that has randomly oriented dipoles as seen in Fig. 2.2 in the line segment 1-2, in the presence of an electric field they are aligned as well as possible at point 2. In section 2-3, the material has all the domains aligned and the slope is proportional to the high-field dielectric constant. When the field is removed from the sample the polarization does not go to zero but returns to point 4, and many dipoles are still aligned in the positive direction. The polarization value at point 4 is called the remanent polarization. When a negative field is applied to the sample, the dipoles begin to switch towards the negative direction. The electric field at which the net polarization is zero (point 5) is called the coercive field and is representative of how difficult it is to switch the polarization. Under larger negative fields the polarization is again saturated,
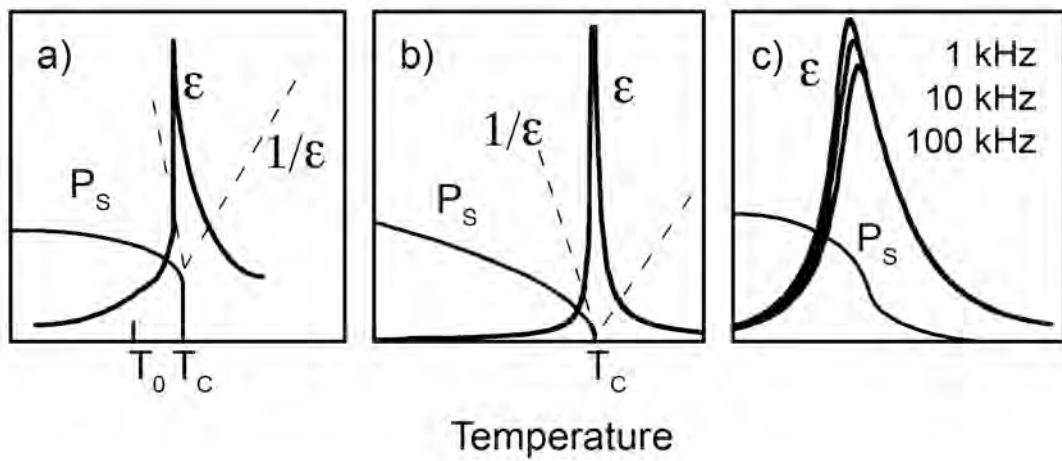
Fig. 2.1 Schematic of the temperature dependence of the polarization, and dielectric constant (ε) for a) first order, b) second order, and c) relaxor ferroelectric transition.[4]
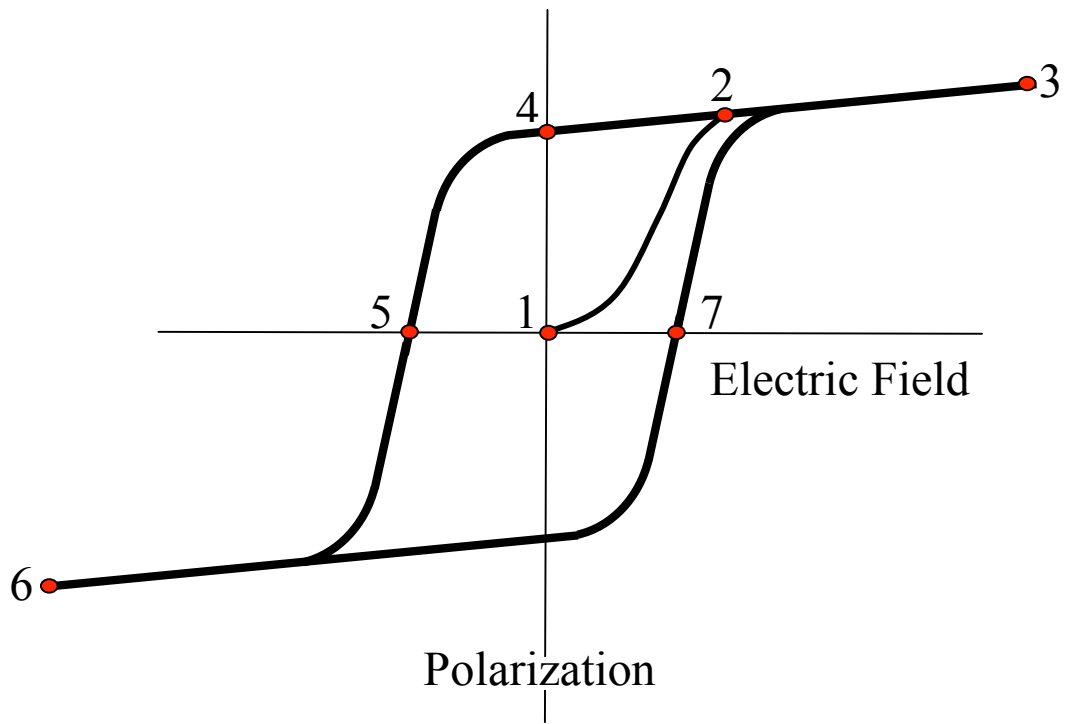
Fig. 2.2 Schematic of polarization-electric field hysteresis loop.

but in the negative direction at point 6. Reversal of field to positive causes the reversal of the net domain orientations and brings the material through point 7 to point 3 for high enough fields. Because domain reversal requires nucleation and growth it is a hysteretic process as shown in Fig. 2.2. The polarization-electric field hysteresis loop is one of the main characteristics of ferroelectrics and separates them from other polar materials.

The prototypical structure for most commercially important ferroelectrics is the perovskite structure (Fig. 2.3). These materials have the general formula ABX_3 where A and B are cations, and X is an anion. At high temperatures, perovskite ferroelectrics have a cubic structure. The structure has A atoms at the cube corners sites, the B atoms at the center site, and the X atoms in the face centered sites. However, when the material is in its ferroelectric state the atoms are all slightly displaced, giving it a permanent dipole moment.

In addition to the distortion of the perovskite due to the spontaneous polarization there can be several distortions by rotation of the BO_6 octahedra (seen in Fig. 2.4(a)).[5] The perovskite structure can be viewed as a series of corner sharing octahedra. These octahedra can rotate, distorting the crystal structure (Fig. 2.4(b)).[6,7] Since the octahedra are attached, tilting of one octahedron affects the surrounding octahedra. If two adjacent octahedra tilt along the same tilt axis, this is called an in-phase-tilt, but if these octahedra tilt in opposite directions this is called an anti-phase-tilt. Glazer, who derived a notation to describe these changes, outlined these types of distortions.[6,7] This notation is based on the relation between the lattice constant and the distortion of an octahedra. For example, $SrTiO_3$ has the notation $a^0b^0c^0$. The sequence of the symbols corresponds to the crystallographic axes, i.e. the first tilt is along a, the second tilt is along b and the third tilt
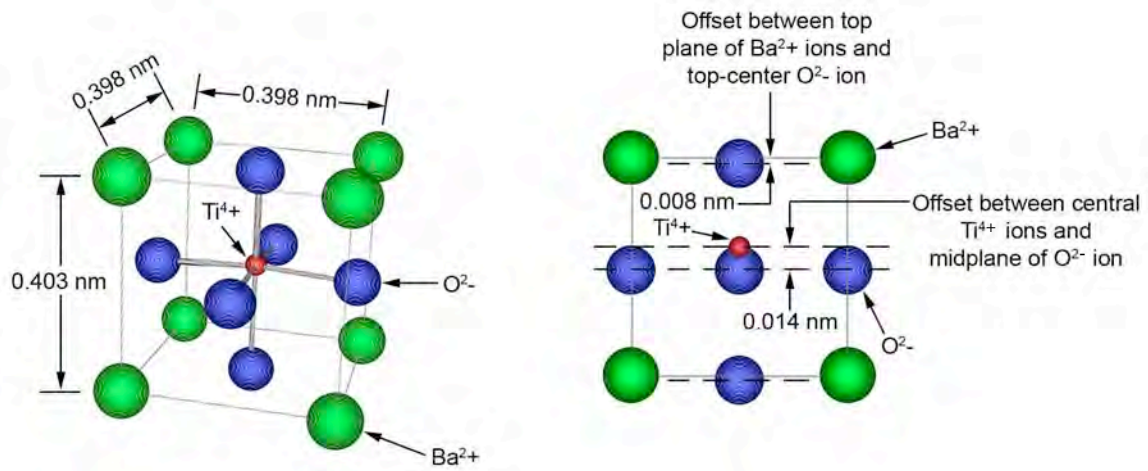
Fig. 2.3 Schematic of ionic displacements for tetragonal BaTiO$_3$ at room temperature.[1]

(a)

Oxygen   Strontium

(b)
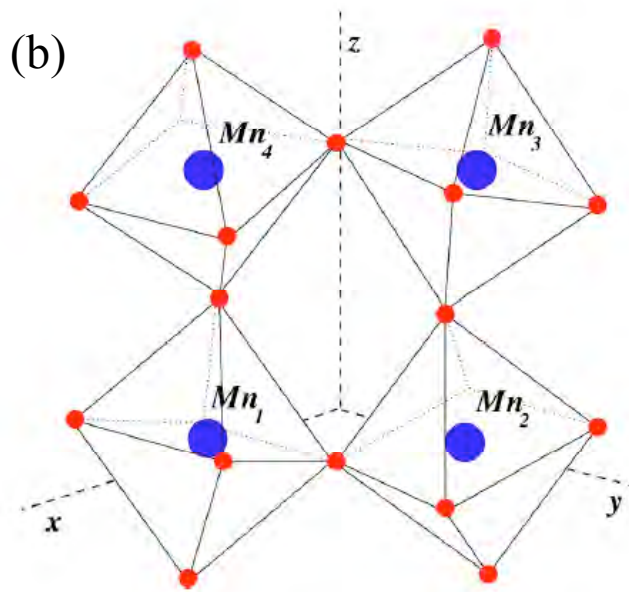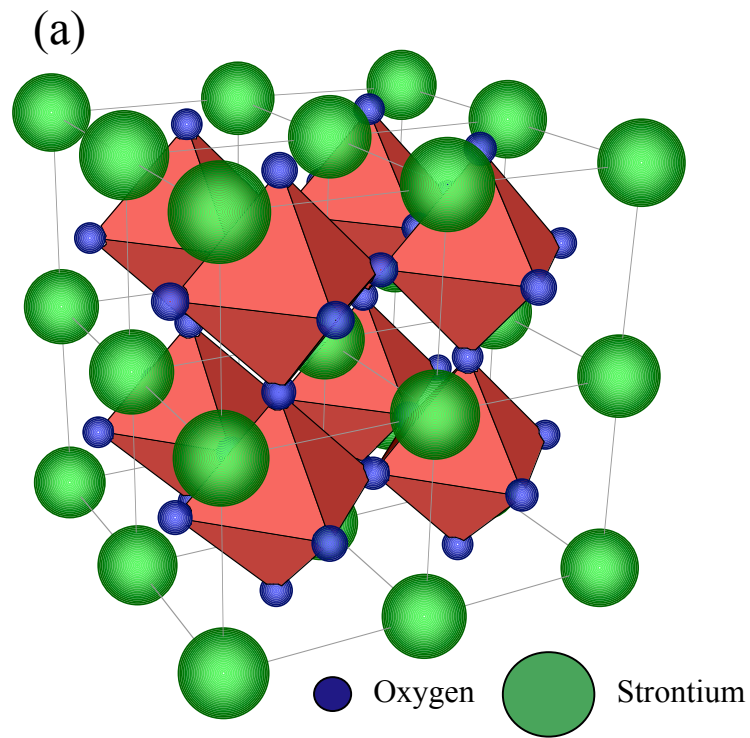
Fig. 2.4 (a) Crystal structure of cubic SrTiO$_3$ at room temperature with the BO$_6$ octahedra shown around the Ti atom. (b) Structure of octahedra for Pr$_{0.6}$Ca$_{0.4}$MnO$_3$ with the GdFeO$_3$ Structure.[5]

is along c. The superscripts describe the type of tilt of subsequent octahedra: 0 for zero tilt, + for in-phase tilt and − for anti-phase-tilting. Thus for the cubic $SrTiO_3$ the 0 in all the subscripts means there are no tilts along any axis. The tilt system shown by $GdFeO_3$ is very common for perovskites with small tolerance factors. $GdFeO_3$ is orthorhombic, with a tilt of $a^+b^-b^-$. This means that it has an in-phase tilt along the a-axis as well as two anti-phase-tilts of equal magnitude along the b axis.[6,7]

For materials that are already ferroelectric, these rotational distortions can also be ferroelastic. A ferroelastic transition is one in which a crystal can switch from one stable distortion into another by the application of a mechanical stress along an appropriate direction.[1-4] When $BaTiO_3$ is cooled through its cubic to tetragonal transition, a spontaneous strain develops due to the off centering of the Ti atom, making this a ferroelastic transition as well as a ferroelectric transition.

2.2 Relaxor Ferroelectrics

In the late 1950's a new type of perovskites was discovered by the Soviets.[8] These perovskites generally had the chemical formula $A^{2+}\left(\left(B_I^{5+}\right)_{\frac{2}{3}}\left(B_{II}^{2+}\right)_{\frac{1}{3}}\right)O_3$, for example $Pb(Mg_{2/3}Nb_{1/3})O_3$.[9] These materials were referred to as relaxor ferroelectrics. Soon thereafter many more relaxors were discovered. Most relaxors are characterized by mixed occupancy of one of the sites. Relaxor behavior was also found in materials with the tungsten bronze crystal structure.[10] Key features of relaxors are: (1) a strong frequency dependence of the dielectric constant below the temperature of the permittivity maxima (T_{max}), (2) no evidence of structural macroscopic breaking of the center of symmetry at

T_{max} and no spontaneous polarization just below T_{max}, and (3) ferroelectric-like behavior on field cooling to temperatures much lower than T_{max}.[11,12]

Relaxor ferroelectrics differ from normal ferroelectrics in many ways, as demonstrated in Fig. 2.5. The four typical differences are: (1) they have slim hysteresis loops just below T_{max}, (2) they exhibit some switchable polarization above the dielectric maximum (T_{max}), (3) the temperature dependent permittivity shows a broad peak with strong frequency dependence below T_{max}, and (4) relaxors have no sudden change in properties such as birefringence, index of refraction, or volume at T_{max}.[13]

Several models have been proposed to explain relaxor behavior. These include compositional inhomogenieties,[9] superparaelectricity,[12] spin-glass-like behavior,[14] a breathing mode model,[15] and a random local field model.[16,17] There are considerable discrepancies between these models, and it is still controversial as to which best describes the behavior of relaxors. The most rudimentary model was originally proposed by Smolenskii and was based on compositional disorder.[9] This model attributes the breadth of the dielectric peak to "the presence of different kinds of ions in the same crystallographic positions," i.e. cation disorder.[11] The cation disorder leads to fluctuations of the composition that cause a range of Curie temperatures. Thus, in this model the material near the transition temperature consists of polar and non-polar regions. This combination of polar and non-polar regions leads to a smearing of the ferroelectric phase transition. While this model is consistent with the observation that relaxor ferroelectricity often appears in materials with some compositional heterogeneity, it does not explicit account for the interaction between individual dipoles.[11]

15

Normal Ferroelectric		Relaxors
P_R P P_S — P-E hysteresis loop — E_C E • Macro-size FE domains	(a)	P_R — P-E loop — E_C E • Nano-size polar domains
P P_S or P_R — curve — T T_C • No polar domains above T_c	(b)	P — curve — T T_m • Nano-size polar domains persist well above T_m
ε', $1/\varepsilon'$ vs T (K), peak at T_C •sharp narrow transitions •ε'(T) follows Curie-Weiss law •No frequency dispersion	(c)	PBZT-Bi, 1 bar, $\varepsilon'' \times 10^{-4}$ vs T (K) 10^3 Hz, 10^4 Hz, 10^5 Hz • very broad ε'(T) peaks • strong deviation from Curie-Weiss law • strong frequency dispersion
• 1st - or 2nd - order phase transition with macroscopic symmetry change at T_c • Strong optical anisotropy across T_c		• No structural phase transition across T_m • Critical slowing down of dipolar motion below T_m • No optical anistropy across T_m

Fig. 2.5 Differences in properties between normal ferroelectrics (left) and relaxor ferroelectrics (right) (a) P-E hysteresis loops (b) Polarization as a function of temperature (c) Temperature dependence of the permittivity.[13]

Another approach to describing the diffuseness of the phase transition is the presence of nano-polar domains. Since ferroelectricity is a cooperative phenomenon, the volume of the ferroelectric regions will affect the transition. When the volume of the ferroelectric region is reduced down to a region of near 1000 nm^3, the energy barrier separating polar and non-polar regions will be on the order of kT (the thermal energy). Thus, if the polar nano-regions are on the order of this size, the transition to a non-polar state would be expected. Furthermore, if a distribution of sizes and stoichiometry of these regions existed, this would result in a broadening of the transition and the frequency dependence of the permittivity.[12] Nano-polar regions on the order of this size would also not be detectable by long range characterization probes, such as x-ray diffraction and optical birefringence, as seen in relaxor ferroelectrics.

Compositional disorder or nano-polar regions alone do not fully describe the appearance of the frequency dependence of the dielectric permittivity in the temperature range below T_m. Another approach that describes the frequency response accounts for the environment around the nano-polar domains. If the material close to a nano-polar domain is not uniform, then the free energy in different polar directions will not be equal. Thus, there would be an interaction between the polarization and the surrounding environment that will cause a lower free energy along one of the polar directions. This will in turn cause the potential well in this direction to be lower, and the polarization will spend more time in this direction.[18] Thus the dispersive behavior of the low-field permittivity could originate from a difference in the residence times of various polar orientations.[12] In the case of no or limited interactions, this model should converge to superparaelectricity and

the dielectric maxima should be described by a simple Debye equation. However, fits to the Debye equation give physically unrealistic values for thermally activated polarization fluctuations (7 eV and 10^{40} s^{-1} for the activation energy and pre-exponential factor).[19]

Alternatively, Viehland *et al.*[14] suggested that the dispersive behavior of ferroelectric relaxors resulted from the dielectric analog to the spin glass state in magnetization. In spin glasses the disorder in the local magnetic moment is believed to be due to competing ordering interactions between neighboring clusters leading to frustration.[20] Thus, Viehland *et al.* suggested that the dielectric dispersion could be described by the Vogel-Fulcher relationship:

$$ f = f_0 \exp\left(\frac{-E_a}{k(T_m - T_f)} \right) \qquad \text{Eq. 2.2} $$

where f_0 is the characteristic frequency, E_a is the activation energy, and T_f is the freezing temperature, typical values for these variables are given in

Table 2.1. In this equation, E_a represents the activation energy for polarization fluctuations of an isolated cluster. The temperature dependence of the equation can be attributed to the development of the short range order between neighboring clusters with an interaction energy of kT_f.[14] The physical model this suggests is polar clusters with random distributions of polar orientations, similar to the state of the magnetization in spin glasses. When cooled, the polar clusters form a preferred polar orientation due to long-range interactions between the polar clusters. However, long range ordering is suppressed by the frustrated interactions during the freezing process.[21]

Table 2.1 Values for Vogel-Fulcher relation for several relaxor materials.

Material	f_0 (Hz)	E_a (meV)	T_f (K)	Reference
$(Sr_{0.9}Bi_{0.1})TiO_3$	4.12×10^{12}	25	95.5	22
$Pb(In_{0.5}Nb_{0.5})O_3$	1.21×10^{11}	29	313	23
$0.75\ Pb(Mg_{0.33}Nb_{0.66})O_3–0.25\ PbTiO_3$	9.03×10^{11}	17.3	109	24
$0.90\ Pb(Mg_{0.33}Nb_{0.66})O_3–0.10\ PbTiO_3$	1.03×10^{12}	40.7	291.5	14
$(Pb_{0.92}La_{0.08})(Zr_{0.65}Ti_{0.35})O_3$	1.72×10^{13}	117	230	25
$(Pb_{0.90}5La_{0.095})(Zr_{0.65}Ti_{0.35})O_3$	1.51×10^{13}	89.5	230	25
$Pb(Zr_{0.33}Nb_{0.66})O_3$	3.47×10^{12}	19.5	290	26
$0.90\ Pb(Zr_{0.33}Nb_{0.66})O_3–0.10\ PbTiO_3$	1.58×10^{12}	16.5	297	26
$Ba(Ti_{0.7}Zr_{0.3})O_3$	1.54×10^{10}	210	200	27
$Ba(Ti_{0.9}Ce_{0.1})O_3$	1.45×10^{11}	7.6	320	28
$Ba(Ti_{0.8}Ce_{0.2})O_3$	1.06×10^{8}	27	139	28

The existence of polar nano-regions was demonstrated by Randall *et al.*[29] In those experiments, transmission electron microscopy was used to directly image polar nano regions in several $Pb(B',B'')O_3$ compounds. It was also found that the dimensions were on the order of 50 Å, which corresponded to the predictions of earlier studies.[30] The inhomogeneity models were further strengthened by work in the $PbSc_{1/2}Ta_{1/2}O_3$ system.[31,32] This work showed that when the Sc and Ta atoms were randomly arranged on the B site of the material, the material exhibited relaxor ferroelectric behavior. However,

through annealing the Sc and Ta could be ordered on the B site and the material would exhibit normal ferroelectric behavior.

Nonetheless, there are still questions about these descriptions. Reports by Davies *et al.* indicated the original local ordering proposed for the B site ions is incorrect.[33] Annealing of $Pb(Mg_{1/3}Ta_{2/3})O_3$ doped with Zr demonstrates that 90% ordering does not eliminate the frequency dispersion of the dielectric permittivity. In this case, the ordering was not as proposed by the Smolenskii but rather it was hypothesized that the ordering was of planes of B atoms, where planes with a random arrangement of 2/3 B^{+2} and 1/3 B^{+5} alternated with planes of B^{+5}. Another complication is that Dmowski *et al.* have shown by a combination of neutron and x-ray diffraction that there is not a detectable local displacement of the B cation from the cube center in $Pb(Sc_{1/2}Ta_{1/2})O_3$ even for the ordered normal ferroelectric state.[34] It should be noted that this is inconsistent with the case found in PZN and PMN where there are local displacements.[35]

Recently two new models have been proposed that are consistent with the key characteristics of relaxors, the random field model and the breathing model. The random field model assumes that there is disorder inherent in relaxor ferroelectrics with random orientations and positions for electric dipoles, lattice defects, and unavoidable impurities. This disorder leads to a distribution of random fields, which means different ions are affected by different local fields. This is in contrast to the typical description of ferroelectrics where a homogeneous field from the surrounding atoms is assumed. Essentially, this theory describes relaxors as dipolar glasses where random fields and random interactions between polar regions lead to the freezing transition into a glassy

state. This model predicts the frequency dependence of the permittivity and freezing of the domains as a function of temperature.

The breathing model is based on the concept of frozen nano polar domains. Originally proposed by Isopov in 1950's[36-38] it was not until it was formalized by Glazounov and Tagantsev [15,39,40] that much attention was paid to the model. In the breathing model, the relaxor behavior of a single domain or polar nano-region is associated with the oscillations and movement of domain walls, i.e. the "breathing" of the domain in an ac electric field. This model is capable of describing the frequency dependence of the first and third harmonics of PMN. However this model ignores the interactions between polar regions that must occur when the domains begin to percolate through the material.[38]

A major difference between the random field models and the breathing model is the behavior of the third harmonic of the dielectric permittivity. More precisely, the non-linear susceptibility of the third harmonic may differentiate between these two models. The non-linear susceptibility of the third harmonic (a_3) is:

$$a_3 = \chi_3 / \chi_1^4 \qquad \text{Eq. 2.3}$$

where χ_3 and χ_1 are the third order and first order dielectric susceptibilities as defined by:

$$P = \chi_1 E - \chi_3 E^3 + \chi_5 E^5 \ ... \qquad \text{Eq. 2.4}$$

where P is the polarization, E is the electric field and χ_i are the ith order dielectric susceptibilities. The random field model suggests that there is a peak in a_3 at the freezing temperature while the breathing model does not produce this feature.[40,41] Both models are able to describe the non-linearity of the third harmonic above the freezing temperature.[39,40] Though, no peak in a_3 at the freezing temperature has been observed by

some researchers.[40,42] others have observed a peak in the a_3.[17,43] Thus, there is no definitive conclusion as to which model is more accurate. Application of this approach to a wide variety of materials may be useful in determining the validity various models.

Cooling a relaxor ferroelectric in the presence of a dc bias electric field aligns the nano-polar domains and can lead to conventional domain structures. Under a large enough field, long-range order can be established to induce a normal ferroelectric state.[44] Thus, the occurrence of this nano to macro domain transition is a balance between the bias field, thermal fluctuations, and the strength of the dipolar interactions.[45] The remanent effect of the bias field can easily be seen in the dielectric constant vs. temperature data. Fig. 2.6 shows a comparison of the typical frequency dependence of the real part of the permittivity after exposure to different dc biases. Fig. 2.6(a) shows a typical response for zero field heating (ZFH) or zero field cooling (ZFC) without prior biasing. Fig. 2.6(b) depicts data for a sample that was ZFC then field heated (FH). In this case there are four distinct regions. In region I, the randomly oriented domains are frozen and are characterized by a freezing temperature T_F. Below T_F there is not enough thermal energy to re-align the polarization with the field with a small oscillating voltage. Above T_F is region II, where there is enough thermal energy to align and grow the nano-domains into macrodomains. Upon further heating, the thermal energy is high enough to disturb the ordering induced by the bias field, region III. This results in the appearance of frequency dispersion. As the temperature is increased further, the material approaches the paraelectric like state, region IV, where the nano-domains undergo rapid thermal fluctuations until the Burn's temperature is reached (T_d). The Burn's temperature is the point where the nano-polar domains nucleate, and above T_d there is no local polarization.
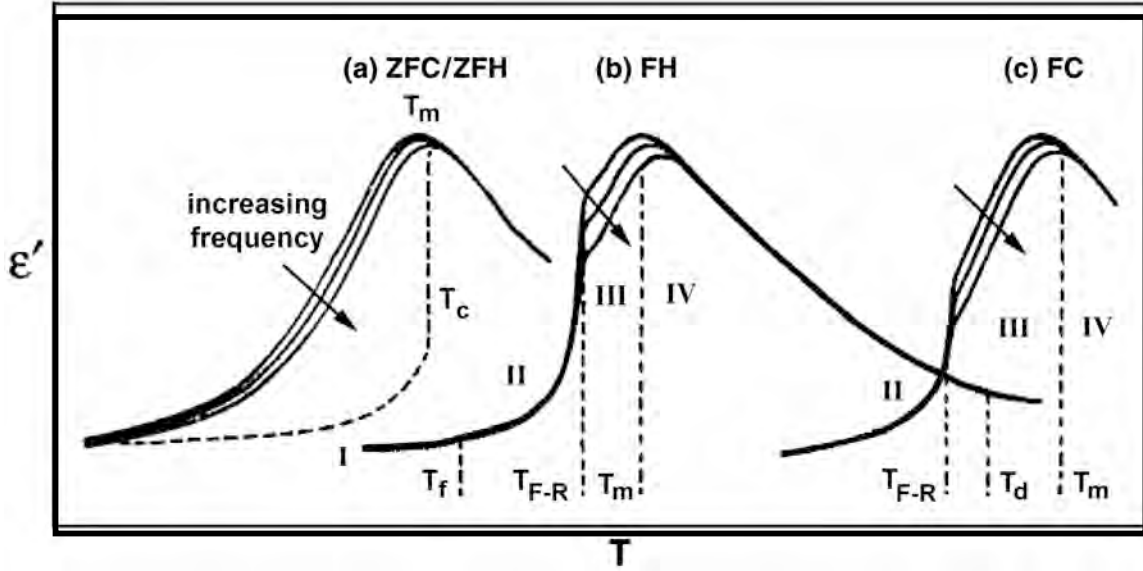
Fig. 2.6 Schematic of the real part of the permittivity of a relaxor ferroelectric as a function of temperature for: (a) no applied field on heating and cooling (b) heating with an intermediate applied bias field, and (c) cooling with an intermediate applied bias field. Where T_m is the temperature of the maximum permittivity, T_f is the temperature at which the polarization is frozen, T_{F-R} is the temperature at which the frequency dispersion begins, and T_d is the Burn's temperature, above which there is no polarization. [45]

Unlike a normal ferroelectric, there is no large dielectric anomaly at T_d. Instead, the Burn's temperature can be detected by changes in properties that depend on the square of the polarization such as the refractive index or the lattice parameter. Fig. 2.6(c) shows the same behavior but under field cooling (FC) after ZFH conditions. Region III is different; here the field aligns and then grows the nano-domains into macro-domains which remain down to the lowest temperatures. It is also important to note that T_m is usually increased under the applied bias field, because the field acts to stabilize the ferroelectric state.[13]

2.3 SrTiO$_3$

This material has been of considerable interest due to its low temperature properties. At room temperature SrTiO$_3$ has the cubic prototypical perovskite Pm3m structure, but when cooled below 105 K the material undergoes an antiferrodistortive transition to an I4/mcm tetragonal phase.[46-48] This transition can be described in terms of its tilts; in the cubic phase SrTiO$_3$ has no tilting of the oxygen octahedra. Using the Glazer notation, as discussed earlier, cubic SrTiO$_3$ has an $a^0a^0a^0$ tilt system. The transformation into the tetragonal crystal structure is due to a coupled tilting of the oxygen octahedra along the c axis to $a^0a^0c^-$. The c axis is approximately doubled due to the out-of-phase tilting of the oxygen octahedra.[49] This makes the phase transition at 105 K a displacive one.[46]

SrTiO$_3$ was the first material in which a high dielectric constant at low temperature was associated with a low frequency optical mode.[46] This observation also led to the first clear measurement of a "soft" ferroelectric mode in a study of the phase transition of SrTiO$_3$.[48] This soft mode represents a transverse optical mode that

corresponds to the vibration of the central atom with respect to the oxygen octahedra. Hardening (or freezing to zero) of this mode indicates the central atom is fixed off center and the material has a spontaneous dipole. This soft mode freezing is a signature of many ferroelectric materials. The soft mode behavior in $SrTiO_3$ gave the first direct evidence to prove the Lyddane-Sachs-Teller relation.[50] $SrTiO_3$ has also been shown to possess many special properties such as superconductivity (when doped).[51,52] $SrTiO_3$ has also been shown to exhibit quantum paraelectric behavior,[53] and a large field-induced piezoelectric effect at low temperatures.[54]

The dielectric properties of $SrTiO_3$ are qualitatively similar to those of the paraelectric phase of typical perovskite ferroelectrics like $BaTiO_3$. In these materials there is a soft transverse optical mode whose frequency tends to zero with decreasing temperature (Fig. 2.7).[55,56] This leads to increase in the permittivity of $SrTiO_3$ when the material is cooled, but levels off near 30 K and remains approximately constant at lower temperatures (Fig. 2.8).[53] The temperature dependence of the permittivity and soft mode frequency follow the Curie-Weiss law with a Curie temperature near 40 K.[57] However, $SrTiO_3$ does not undergo a ferroelectric transition. This is attributed to quantum fluctuations in the material at low temperatures that suppress the ferroelectric transition. Hence $SrTiO_3$ is sometimes called a quantum paraelectric.[53,58,59] This quantum paraelectric state, however, is very sensitive to perturbations of the lattice, and a ferroelectric transition has been induced in $SrTiO_3$ by small levels of impurities or doping,[60-68] applied electric fields (here the polar state is not stable at zero
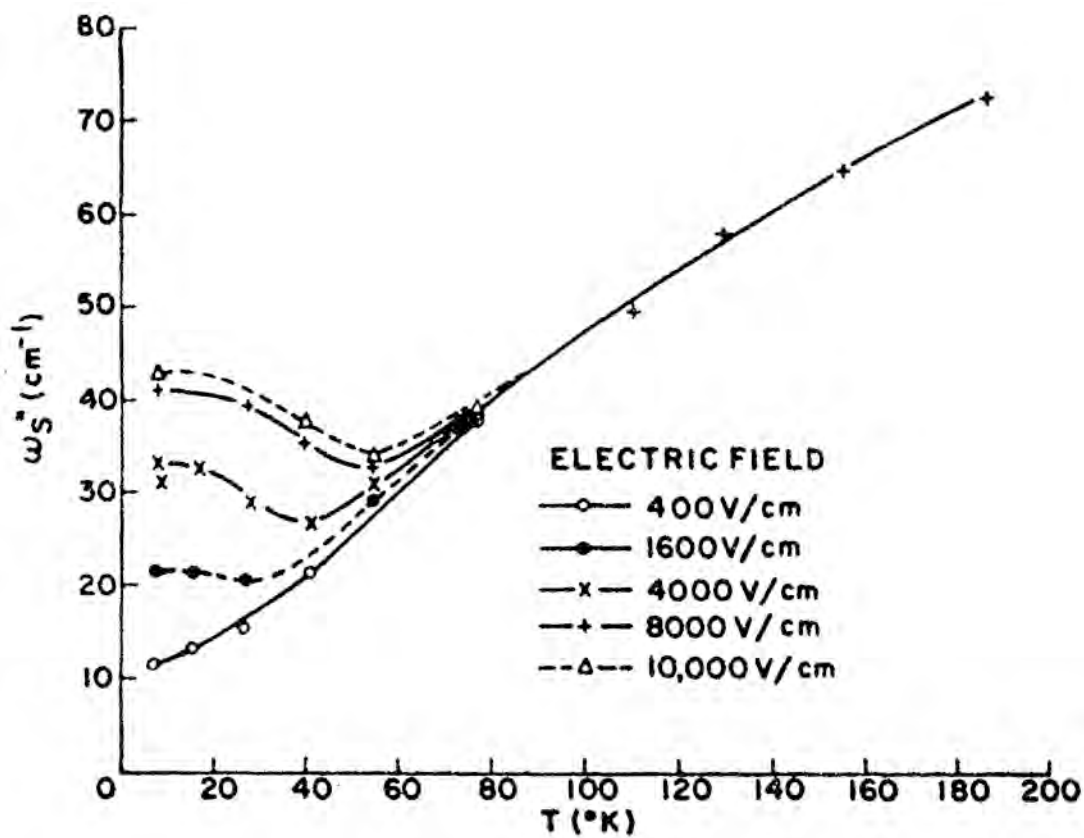
Fig. 2.7 Temperature dependence of the ferroelectric soft modes in $SrTiO_3$ as a function of temperature for several applied fields.[55]
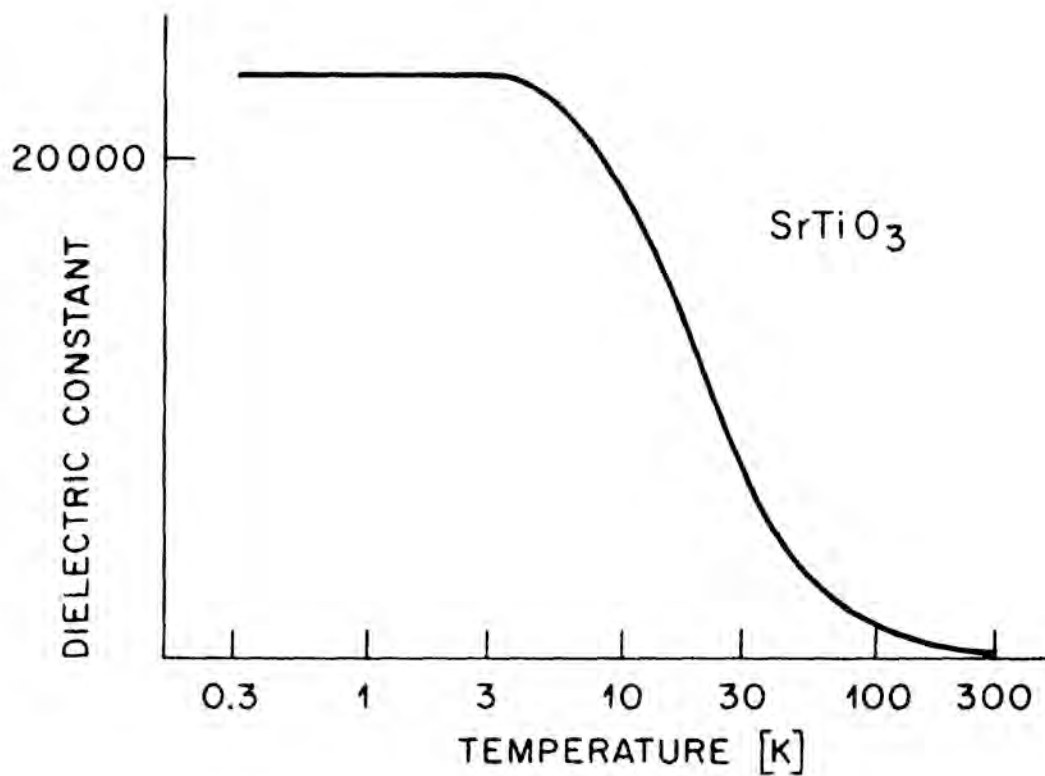
Fig. 2.8 Dielectric constant of SrTiO$_3$ as it is cooled towards 0 K.[53]

field),[69-72] ^{18}O substitution,[73] and mechanical stress.[74,75]

Doping of SrTiO$_3$ with other cations is one of the most direct methods to introduce ferroelectricity into SrTiO$_3$. This has been shown most clearly on doping SrTiO$_3$ with Ca or Bi (Fig. 2.9).[60-68] The reason for this impurity-induced ferroelectric phase transition is still not completely clear. However, one likely explanation entails an off-center impurity ion moving in a multi-site potential well.[58] The interaction between the impurity ion dipole moments through the soft polar transverse optical mode gives rise to both the formation of a dipole glass phase and a transition to the ferroelectric state.[64] It is intriguing that there is a dipolar moment due to the off-centered position of the cation, even for an isovalent substitution (the case of Ca substituting for Sr).[66] However the position of the Ca impurity atoms is still in question; they can sit on either the A-site or B-site.[74] If the Ca^{2+} occupies the B-site, it will necessitate an impurity-oxygen vacancy pair defect for charge neutrality. However, theoretical modeling suggests that the A site is more likely for the case of Ca^{2+} doping.[76] Fig. 2.9(b) shows the permittivity versus temperature data for Bi-doped SrTiO$_3$ ceramics. A small amount of dopant increases the low temperature permittivity without significantly altering the shape of the curve. In addition, it was found that at these lower levels of doping the material undergoes dielectric relaxation.[62] At higher dopant concentrations SrTiO$_3$ becomes a relaxor ferroelectric with a non-zero T_{max}.[67] The main reason given for this was that the impurities in the highly polarizable SrTiO$_3$ matrix create local dipoles. These dipoles nucleate nano-polar domains. At lower dopant concentrations these nano-domains are
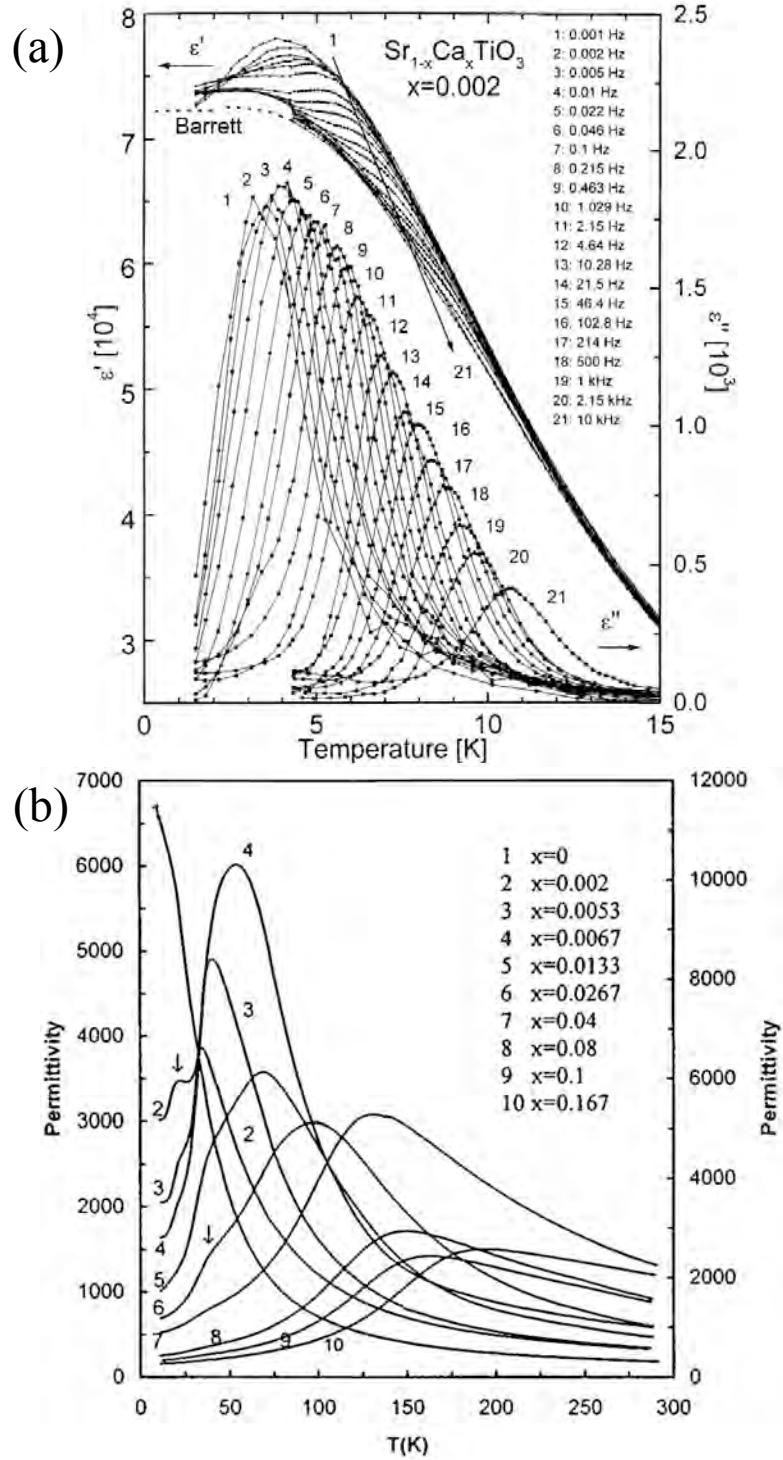
Fig. 2.9 Permittivity as a function of temperature for (a) 0.2% Ca Doped SrTiO$_3$[64]

and (b) Sr$_{1-x}$Bi$_x$TiO$_3$[68] showing an induced ferroelectric transition for doped SrTiO$_3$

spaced far enough apart so that they do not interact with one another. Once a critical doping concentration is reached, the nano-polar domains begin to interact with one another to form a relaxor ferroelectric state.[45,60,61]

Even without doping it is possible to induce a permittivity peak in $SrTiO_3$ by an applied dc bias field. Hemberger *et al.* showed this originally.[69] They claimed that the DC field suppresses the quantum fluctuations and allows for the onset of a coherent tunneling ground state. Fleury later confirmed this with Raman studies.[70] Fuchs *et al.* studied this effect in $SrTiO_3$ thin films.[72] They found that $SrTiO_3$ develops a well-defined hysteresis loop when under DC bias and observed the characteristic dielectric susceptibility change associated with a ferroelectric at low temperatures.[72] However, it is important to note that the field-induced ferroelectric state differs from a normal ferroelectric in that the polarization is not stable at zero field.

A ferroelectric phase transition in $SrTiO_3$ has also been induced by the partial exchange of ^{16}O by the isotope ^{18}O, yielding a low temperature ferroelectric state.[73] This effect is not predicted by classical approximations that depend on harmonic force constants; it is quantum mechanical in nature.[45,58,77] It is believed that the quantum mechanical zero point vibrations contribute to atomic force constants enough to stabilize the soft transverse optical mode in pure $SrTiO_3$ and suppress the ferroelectric phase even at 0 K, as stated previously. However, this zero-point vibration depends on the atomic masses, as does the phonon frequency. An increase in the atomic mass (such as ^{18}O substitution) can suppress this zero-point vibration and induce a low temperature ferroelectric phase (or rather prevent the zero-point vibrations from suppressing the low temperature ferroelectricity). The nature of the ferroelectric state still seems to be

controversial. Bussmann-Holder and colleagues[77,78] and Kvyatkovskii[79] have predicted a displacive soft-mode mechanism for the phase transition into a ferroelectric state. However, Yamada *et al.* claim that in ^{18}O modified $SrTiO_3$, the transition is into a three state quantum order-disorder system. This order-disorder nature was first suggested by Zhang *et al.* [80] and seems to be supported by recent work of Dec, Kleeman, and Itoh.[81]

Though hydrostatic pressure was not found to change the quantum paraelectric state,[82] uniaxial pressure was found by Uwe and Sakudo[74] to induce the ferroelectric phase. This was attributed to the electrostrictive effect producing an electric field that induced a ferroelectric transision.[74] More recently the effects of biaxial strain in epitaxial thin films were examined by Pertsev, Tagantsev, and Setter.[83] It was predicted from Landau-Ginzsburg-Devonshire theory that due to the coupling between the strain and the polarization in $SrTiO_3$ it was possible to induce ferroelectricity in epitaxial $SrTiO_3$ films. They also were able to determine the equilibrium single domain ferroelectric phase through minimization of the Hemholtz free energy, as depicted in Fig. 2.10. What is interesting is that these predictions show that true ferroelectric phases, FTI and FOI, are present for films under sufficient compressive and tensile strains, respectively. This predictions was confirmed later by Haeni *et al.* for the tensile case of epitaxial $SrTiO_3$ films grown on $DyScO_3$ substrates.[83,84] Likewise, Dalberth *et al.* found for compressively strained $SrTiO_3$ grown $LaAlO_3$ a peak in the dielectric constant at 35 K that was consistent with a ferroelectric transitions.[85] Results from Astafiev *et al.* also, showed much lower transition temperatures using only thermal expansion mismatch that were attributed to non-stoichiometry of their films instead of the mechanical constraints.[86,87]
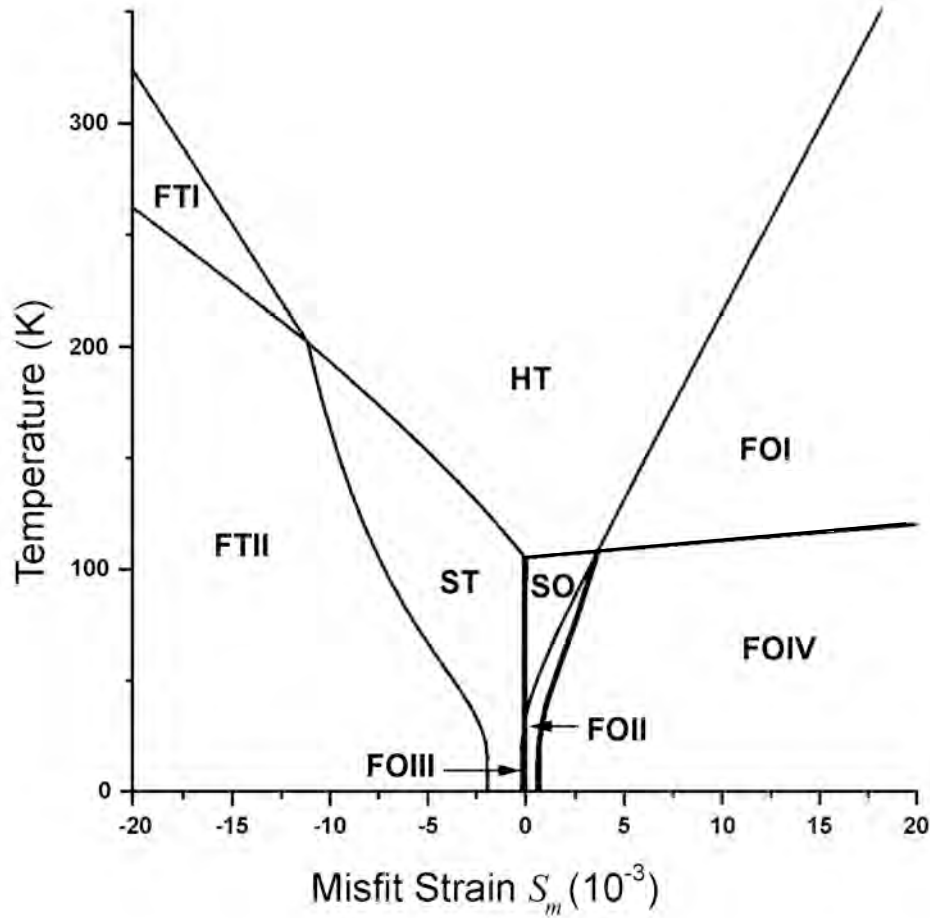
Phase	HT	ST	SO	FTI	FTII	FOI	FOII	FOIII	FOIV
P				P_3	P_3	$\|P_1\|=\|P_2\|$	P_1 or P_2	$\|P_1\|=\|P_2\|$	$\|P_1\|=\|P_2\|$
q		q_3	q_1 or q_2		q_3		q_1 or q_2	q_3	$\|q_1\|=\|q_2\|$

Fig. 2.10 Calculated phase diagram for single domain, epitaxial $SrTiO_3$ films with different misfit strains where F denotes ferroelectric, S is a structural, distorted perovskite O and T represent orthorhombic and tetragonal phases respectively, and HT represents the high temperature cubic phase. The accompanying table shows order parameter q_i (which describes tilting of the octahedra along different directions) and P_i (the polarization directions) present for each phase.[83]

Reference

[1] M. E. Lines and A. M. Glass, *Principles and Applications of Ferroelectrics and Related Materials* (Oxford: Pergomon Press, New York, 1977).

[2] F. Jona and G. Shirane, *Ferroelectric Crystals* (Dover Publications Inc. New York, 1993).

[3] IEEE Standard on Ferroelectrics, IEEE Trans. Ultrason. Ferroelectr. Freq. Control. **50**, 1 (2003).

[4] D. Damjanovic, Rep. Prog. Phys. **61**, 1267 (1998).

[5] S. Grenier, J. P. Hill, Doon Gibbs, K. J. Thomas, M. V. Zimmermann, C. S. Nelson, V. Kiryukhin, Y. Tokura, Y. Tomioka, D. Casa, T. Gog, and C. Venkataraman, Phys. Rev. B **69**, 134419 (2004).

[6] A. M. Glazer, Acta Crystallographica B **28**, 3384 (1972).

[7] A. M. Glazer, Acta Crystallographica A **31**, 756 (1974).

[8] G. A. Smolenskii, A .I. Agranovskaya, and S. N. Popov, Sov. Tech. Phys. **28**, 2152 (1958).

[9] G. A. Smolenskii, V. A. Isupov, A. I. Agranovskaya, and S. N. Popov, Sov. Phys. Solid State, **2** 2906 (1960).

[10] G. A. Smolenskii, A. I. Agranovskaya, V. A. Isupov, and S. N. Popov, Sov. Phys. Solid State, **2** 2584 (1961).

[11] G. A. Smolenskii, V. A. Bokov, V. A. Isupov, N. N. Krainik, R. E. Pasynov and A. I. Sokolov, *Ferroelectric and Related Materials*, edited by G.A. Smolenskii (Gordon and Breach, New York, 1984).

[12] L. E. Cross, Ferroelectrics **76**,241-267 (1987).

[13] W. Kleemann, G. A. Samara, and J. Dec, in *Polar Oxides: Properties, Characterization, and Imaging*, edited by R. Waser, U. Böttger, and S. Tiedke (Wiley-VCH, Weinheim, 2005), pp. 275-301.

[14] D. Viehland, S. J. Jang M. Wuttig, and L. E. Cross, J. Appl. Phys. **68**, 2916 (1990).

[15] A. E. Glazounov and A. K. Tagansev, Ferroelectrics **221**, 57 (1999).

[16] W. Kleemann and A. Clossner, Ferroelectrics **150**, 35 (1993).

[17] R. Pirc and R. Blinc, Phys. Rev. B **60**, 13470 (1999).

[18] J. P. Maria, Ph.D. Thesis, The Pennsylvania State University, 1998.

[19] V. Kirillov and V. Isupov, Ferroelectrics **5**, 3 (1973).

[20] K. Binder and K. Schroder, Solid State Commun. **18**, 1361 (1976).

[21] L. E. Cross, Ferroelectrics **151**, 305 (1993).

[22] C. Ang. Z. Jing, and Z. Yu, Phys. Rev. B **61**, 957 (2000).

[23] A. A. Bokov, M. A. Leshchenko, M. A. Malitskaya, and I. P. Raevski, J. Phys.: Condens. Matter **11**, 4899 (1999).

[24] A. A. Bokov and Z.-G. Ye, J. Phys: Condens Matter **12**, L541 (2000).

[25] S. Kamba , V. Bovtun, J. Petzelt, I. Rychetsky, R. Mizaras, A. Brilingas, J. Banys, J. Grigas and M. Kosec, J. Phys.: Condens. Matter **12**, 497 (2000)

[26] S. Kamba and J. Petzelt in *Piezoelectric Single Crystals and Their Applications* ed. S. Trolier-McKinstry, L. E. Cross and Y. Yamashita, (University Park, PA, S. Trolier-McKinstry) (2004).

[27] Z. Yu, C. Ang, R. Guo, and A. S. Bhalla, J. Appl. Phys. **92**, 2655 (2002).

[28] C. Ang, Z. Jing, and Z. Yu, J. Phys.: Condens. Matter **14**, 8901 (2002).

[29] C. A. Randall and A. S. Bhalla, Jpn. J. Appl. Phys. **29**, 327 (1990).

[30] C. A. Randall, A. S. Bhalla, T. R. Shrout, and L. E. Cross, J. Mat. Res. **5**, 829 (1989).

[31] N. Setter and L. E. Cross, J. Mat. Sci. **15**, 2478 (1980).

[32] C. G. F Stenger, F. L. Scholten, and A. J. Burggraaf, Solid State Comm. **32**, 989 (1979).

[33] M. A. Akbas and P. K. Davies, J. Am. Ceram. Soc. **80**, 2933 (1997)

[34] W. Dmowksi, M.K. Akbas, P.K. Davies, and T. Egami, J. Phys. Chem. Solids. **61**, 229 (2000).

[35] I. Grinberg and A. M. Rappe, Phys. Rev. B **70**, 220101 (2004)

[36] G. A Smolensky and V. A. Isupov, Zhurn Tekhn. Fiz. **24**, 1375 (1954).

[37] V. A Isupov, Fiz. Tverd. Tela **5**, 1912 (1956)

[38] V. A. Isupov, Ferroelectrics **289**, 131 (2003).

[39] A. E. Glazounov, A. K. Tagantsev, and A. J. Bell, Phys. Rev. B **53**, 11281 (1996).

[40] A. E. Glazounov and A. K. Tagantsev, Phys. Rev. Lett. **85**, 2192 (2000).

[41] J. Hemberger, H. Ries, R. Böhmer, and A. Loidl, Phys. Rev. Lett. 78, 2863 (1997).

[42] J.-H. Ko1, F. Jiang, S. Kojima1, T. A. Shaplygina and S G Lushnikov, J. Phys.: Condens. Matter **13**, 5449 (2001).

[43] Z. Kutnjak, V. Bobnar, C. Filipic and A. Levstik, Europhys. Lett., **53**, 673 (2001).

[44] G. B. Schmidt, H. Arndt, G. Borchardt, J. V. Cieminski, T. Petzsche, K. Bormann, A. Sternberg, A. Zirnite and A. V. Isupov, Phys. Status Solidi A **63**, 501 (1981)

[45] G. A. Samara, J. Phys.: Condens. Matter **15**, R367 (2003).

[46] K. A. Müller, W. Berlinger, C. H. West and P. Heller, Phys. Rev. Lett. **32**, 160 (1974)

[47] H. Unoki and T. J. Sakudo, J. Phys. Soc. Jpn. **23**, 546 (1967).

[48] G. Shirane and Y. Yamada, Phys. Rev. **177**, 858 (1969).

[49] M. A. Geday and A. M. Glazer, J. Phys.: Condens. Matter **16**, 3303 (2004).

[50] C. Kittel, *Introduction to Solid State Physics, 7th Edition*, (Wiley, New York 1996).

[51] J. F. Schooley, W. R. Hosler and M. L. Cohen, Phys. Rev. Lett. **12**, 474 (1964).

[52] F. Pan and C. T. Rogers, Phys. Rev. B **72**, 094520 (2005).

[53] K. A. Müller and R. Burkard, Phys Rev. B **19**, 3593 (1979).

[54] D. E. Grupp and A. M. Goldman, Science, **276**, 392 (1997).

[55] P. A. Fleury and J. M Worlock, Phys. Rev **174**, 613 (1968).

[56] H. Vogt, Phys. Rev. B **51**, 8046 (1995).

[57] R. Viana, P. Lunkenheimer, J. Hemberger, R. Böhmer, and A. Loidl, Phys. Rev. B **50**, 601 (1994).

[58] O. E. Kvyatkovskii, Solid State Commun. **117**, 455 (2001).

[59] W. Zhong and D. Vanderbilt, Phys. Rev. B **53**, 5047 (1996).

[60] J. G. Bednorz and K. A. Müller, Phys. Rev. Lett. **52**, 2289 (1984).

[61] W. Kleemann, J. Dec, Y. G. Wang, P. Lehnen, and S. A. Prosandeev, J. Phys. Chem. Solids **61**, 167 (2000).

[62] C. Ang, Z. Yu, P. M. Vilarinho, and J. L. Baptista, Phys. Rev. B **57**, 7403 (1998).

[63] W. Kleeman, A. Albertini, M. Kuss, and R. Lindner, Ferroelectrics **203**, 57 (1997).

[64] W. Kleemann, J. Dec, Y. G. Wang, P. Lehnen, and S. A. Prosandeev, J. Phys. Chem. Solids **61**, 167 (2000).

[65] G. A. Samara, J.Phys.: Condens. Matter **15**, R367 (2003).

[66] B. E. Vugmeister and M. D. Glinchuk, Rev. Mod. Phys. **62**, 993 (1990).

[67] C. Ang and Z. Yu, J. Appl. Phys. **91**, 1487 (2002)

[68] C. Ang, Z. Yu, and Z. Jing, Phys. Rev. B **61**, 957 (2000).

[69] E. Hegenbarth, Phys. Status Solidi **6**, 333 (1964).

[70] P. A. Fleury and J. M. Worlock, Phys. Rev. **174**, 613 (1968).

[71] J. Hemberger, P. Lunkenheimer, R. Viana, R. Bohmer, and A. Loidl, Phys. Rev. B **52**, 13159 (1995).

[72] D. Fuchs, C. W. Schneider, R. Schneider, and H. Rietschel, J. Appl. Phys. **85**, 7362 (1999).

[73] M. Itoh, R. Wang, Y. Inaguma, T. Yamaguchi, Y-J. Shan, and T. Nakamura, Phys. Rev. Lett. **82**, 3540 (1999).

[74] H. Uwe and T. Sakudo, Phys. Rev. B **13**, 271 (1976).

[75] H.-C. Li, W. Si, R.-L. Wang, Y. Xuan, B. T. Liu, and X. X. Xi, Mater. Sci. Eng. B **56**, 218 (1998).

[76] K. Leung, Phys. Rev. B **61**, 134415 (2001).

[77] A. Bussmann-Holder and H. Büttner, Phys. Rev. Lett. **41**, 9581 (1990).

[78] A. Bussmann-Holder, H. Büttner, and A. R. Bishop, J. Phys.: Condens. Matter **12**, L115 (2000).

[79] O. E. Kvyatkovskii, Solid State Commun. **117**, 455 (2001); Phys. Solid State **43**, 1401 (2001).

[80] L. Zhang, W. Kleemann, J. Dec, R. Wang, and M. Itoh, Euro. Phys. B **28**, 163 (2002).

[81] J. Dec, W. Kleemann, and M. Itoh, Phys. Rev. B **71**, 144113 (2005).

[82] R. P. Lowndes and A. Rastogi, J. Phys. C **6**, 932 (1973).

[83] N. A. Pertsev, A. K. Tagantsev, and N. Setter, Phys. Rev. B **61**, R825 (2000); **65**, 219901(E) (2002).

[84] J. H. Haeni, P. Irvin, W. Chang, R. Uecker, P. Reiche, Y. L. Li, S. Choudhury, W. Tian, M. E. Hawley, B. Craigo, A. K. Tagantsev, X. Q. Pan, S. K. Streiffer, L. Q. Chen, S. W. Kirchoefer, J. Levy, and D. G. Schlom, Nature **430**, 758 (2004).

[85] M. J. Dalberth, R. E. Stauber, J. C. Price, D. Galt, and C. T. Rogers, Appl. Phys. Lett. **72**, 507 (1998).

[86] K. Astafiev, V. Sherman, A. Tagantsev, N. Setter, P. Petrov, T. Kaydanov and D. Ginley, S. Hoffmann-Eifert, U. Böttger, and R. Waser, Integr. Ferroelectr. **59**, 1371 20003.

[87] T. Yamada, K. F. Astafiev, V. O. Sherman, A. K. Tagantsev,P. Muralt, and N. Setter, Appl. Phys. Lett. **86**, 142904 (2005).

Chapter 3

Experimental Procedure

Although a brief discussion of the approaches taken and techniques utilized will be included in each chapter, a more detailed overview will be covered here. This chapter discusses the film growth procedure, as well as the methodology employed for structural and electrical characterization.

3.1 Molecular Beam Epitaxy

The film growth approach used through this thesis was molecular beam epitaxy (MBE). The MBE tool utilized in this work employs thermal evaporation of high purity elemental sources in a high vacuum environment. These sources generate beams of molecules that react at the sample surface to form the desired materials. A high vacuum is necessary to prevent scattering of these molecular beams by ambient gases. This technique has an advantage over many thin film growth techniques in that it has the ability to control the deposition of films on an atomic level. It also has the advantage in that the process entails very little bombardment of the surface. This technique has been used since the 1960's for the deposition of III-V semiconductors.[1,2]

The $SrTiO_3$ films were grown using elemental molecular beams of strontium, titanium, and oxygen in an Applied Epi 930 MBE chamber.[3] The strontium source was a Veeco low temperature effusion cell loaded with 99.99% pure strontium metal premelted into a titanium crucible.[4] The titanium source was a Ti-Ball[5] sublimation pump.[6] To

oxidize the films a molecular beam consisting of a mixture of oxygen and ozone (~10% O_3) was used. The mixture was produced by passing 99.994% pure oxygen through an ASTeX AX8401 ozone generator.[7] Its output flowed continuously into the chamber through a Nupro SS-4BMW leak valve[8] from a continuously pumped loop of the oxygen-ozone mixture (to prevent the ozone from decomposing). Once past the leak valve the oxygen/ozone mixture travels down a water-cooled electropolished stainless steel tube (6 mm diameter) that is directed perpendicular to the substrate surface and ends 64 mm from the front of the substrate. During growth, the background pressure of the chamber was increased with this O_2/O_3 mixture from a base pressure of ~5×10^{-9} to 3×10^{-6} torr. This pressure was maintained after growth until the sample had cooled to room temperature to limit oxygen vacancies in the deposited film.

There are two basic approaches (with many variations) to multi-component MBE film growth: co-deposition and shuttered growth techniques. In co-deposition all the constituent molecular beams are deposited on the substrate surface simultaneously. In this case the fluxes of the individual molecular beams are adjusted to obtain the correct stoichiometry. The thickness is controlled by the length of time these molecular beams are incident on the substrate surface. The other technique, shuttered growth, implements alternating molecular beams, so that only one element is being deposited at any given time. This shuttered growth technique is very similar to migration enhanced epitaxy of GaAs, proposed in the late 1980's.[9] In the shuttered growth technique only one shutter is actuated at a time and the total dose of an element deposited is the product of the time the shutter is open and the flux of the molecular beam. The relative doses of each element are adjusted, usually through the time the shutter is open, to deposit a single stoichiometric

monolayer. For this work the shuttered growth technique was used exclusively and shall be the focus from here onward. For the specific case of $SrTiO_3$ growth, the heated substrate is exposed to alternating monolayer doses from strontium and titanium molecular beams under a steady flux of oxygen/ozone. The fluxes of the strontium and titanium molecular beams and the stability of the source were determined using a quartz crystal monitor placed in front of the substrate. The temperature of the strontium and titanium sources are adjusted to give a flux of $\sim 4 \times 10^{13}$ atoms/cm^2, yielding an average growth rate of about 7 Å/min. Reflection high-energy electron diffraction (RHEED) was implemented to optimize the stoichiometry of the growing $SrTiO_3$ film in real time and monitor the growth.[10] A calibration sample was used for RHEED optimization before the growths to ensure the correct stoichiometry at the beginning of the growth.

MBE deposition of certain materials requires that the elemental sources be supplied to the surface in the correct ratio to create a film of the desired stoichiometry. This can be a challenging task, especially for multi-component materials. The stoichiometry control, to the first order, is calibrated using a quartz crystal microbalance (QCM) that is placed in front of the substrate. This microbalance determines the fluxes of the individual molecular beams and is also used to check the stability of the individual sources. The temperature of the sources is adjusted using the QCM so that the fluxes of the individual molecular beams correspond to a 15 to 20 seconds for one monolayer coverage of the substrate. Calibration with the QCM typically gives an accuracy of ±5%. For higher accuracy, (which is essential in multicomponent oxide dielectrics) in-situ reflection high-energy electron diffraction (RHEED) is utilized. RHEED is well matched to MBE growth, and its development has been inseparably connected to MBE.[11]

Compared to other diffraction techniques RHEED offers many advantages, such as high surface sensitivity and grazing-incidence geometry that is compatible with film deposition. Since the discovery of RHEED oscillations in 1980, RHEED has been used as a convenient way to measure growth rates in MBE. A RHEED oscillation corresponds to growth of one monolayer and in this way it is possible to ascertain the growth rate, thickness and composition of the film.[11]

The RHEED oscillation technique to optimize oxide growth is summarized in Haeni, Theis, and Schlom,[10] but will be elaborated as it applies to this work. This technique is based on monitoring the oscillations of intensity of RHEED diffraction patterns. In this technique, 10 kV electrons are forward scattered from a surface at a grazing angle of ~0.5 to 3.0° using a Staib EK-12-R electron source with a RH-15 RHEED gun[12]. The electrons are then detected on a phosphorous screen revealing the reciprocal space diffraction pattern. For real time analysis a CCD camera is used to detect the RHEED pattern and K-space KSA 400[13] software was used for analysis. Due to the angle of incidence and the small escape depth of the scattered electrons, this technique is very surface sensitive, on the order of a few monolayers, so the diffracted image can be considered a diffraction from the 2-D plane.[14] This 2-D constraint causes points in reciprocal space to become infinite rods and the diffraction condition is the intersection of these rods with the Ewald sphere.[14] For an ideal crystal, this can be viewed as spots on an arc. This technique's sensitivity to the surface structure due to the small escape depth of electrons. This can be exploited to give information on the growth and help guide real time adjustment of the sources during growth.[10]

A description of the growth of $SrTiO_3$ illustrates the features of the technique. Using this technique, the average intensity of the first order diffraction spot is monitored along the [110]. The first order diffraction spot usually gives a more consistent RHEED oscillation than the zero order diffraction or specular spot, and its average intensity is monitored as a function of time. These oscillations referred to here are not the typically RHEED oscillations due to growth, but are actually due to the opening and closing of the shutters. In a RHEED oscillation for $SrTiO_3$, the oscillation can be seen to reach a maximum intensity after a monolayer of SrO has been deposited and a minimum intensity after a monolayer of TiO_2 has been deposited (Fig. 3.1). With full monolayers being deposited, the RHEED intensities at the maxima and minima of the oscillation will remain the same after several layers of $SrTiO_3$ are deposited (Fig. 3.1(a)). However, a change in the stoichiometry can be detected as a change in the oscillation shape, along with an upward or downward trend in the oscillations. If the $SrTiO_3$ being deposited is Ti rich, then the RHEED oscillations can be seen to trend downward. In addition, for this case when the strontium shutter is opened, the intensity will drop, although this effect is often smaller in most growths than that depicted in Fig. 3.1(b). The rate of decrease is dependent on how far the deposition deviates from the stoichiometry; the further off-stoichiometry the film is, the fewer oscillations are needed to recognize the trend. Thus, for small deviations (<1%) it can require many oscillations to see this change. When the $SrTiO_3$ is titanium-poor, the oscillations trend upward at first then after a small amount of time a double peak will appear, as in Fig. 3.1(c). This double peak does not appear as soon as the material is titanium-rich; rather, after a few layers it becomes apparent.
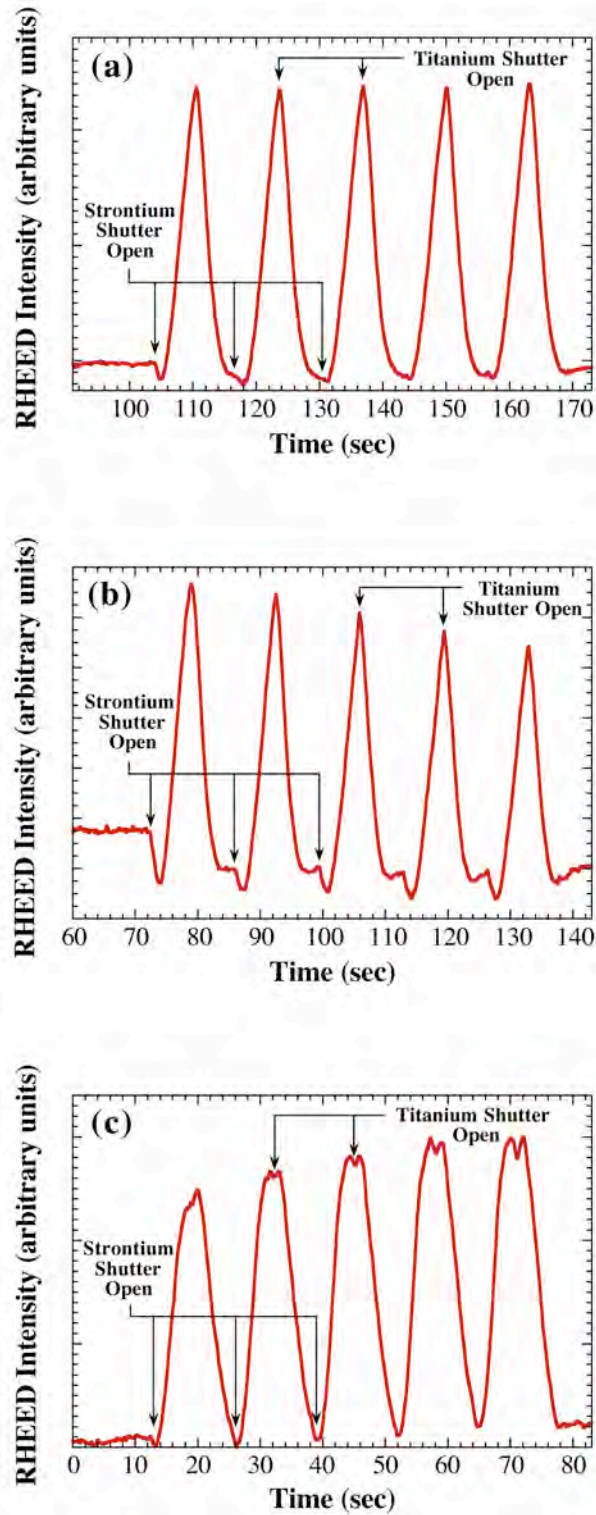
Fig. 3.1 RHEED oscillations for different stoichiometries of $SrTiO_3$; (a) Ideal 1:1 Sr:Ti

stoichiometry; (b) 3% Ti rich composition; (c) 3% Ti deficient.[10]

Therefore, through optimization of the peak shape and maintenance of the same intensity level the stoichiometry can be optimized during growth. Instability in the fluxes of the sources over time can also be identified and compensated for through the continuous monitoring of the RHEED oscillations and real time adjustments of the sources.

The next aspect that must be controlled is the correct monolayer coverage or dose. Again, for perfect monolayer coverage, the RHEED oscillations will not change over many oscillations (Fig. 3.2(c)). However, if coverage is not 100%, a beat wave will become apparent. The frequency of this beat wave is proportional to how far the deposition deviates from monolayer coverage. As indicated by Fig. 3.2, with approximately 85% or 115% deposition of the correct monolayer coverage, the beat frequency is 6 to 7 oscillations. Likewise 90% or 110% of the correct dose per monolayer results in a beat frequency of 10 oscillations. It is apparent that there is no gauge as to which direction the monolayer coverage must be adjusted; too much material per monolayer and too little per monolayer have the same effect. This must be determined by trial and error, although the times determined from the QCM are typically within a few seconds of the optimal times. In this manner, there is a path through which one can determine the correct dose and stoichiometry for film growth through optimization of the RHEED oscillations. Typically a calibration sample is used to determine the correct stoichiometry and dose for a growth and a new substrate is used to grow the desired film.

These changes in RHEED pattern follow the aforementioned observations only under the most ideal circumstances, i.e. homoepitaxy on perfectly terminated substrates. There are many pitfalls in this technique; the first and most difficult to overcome is the

45
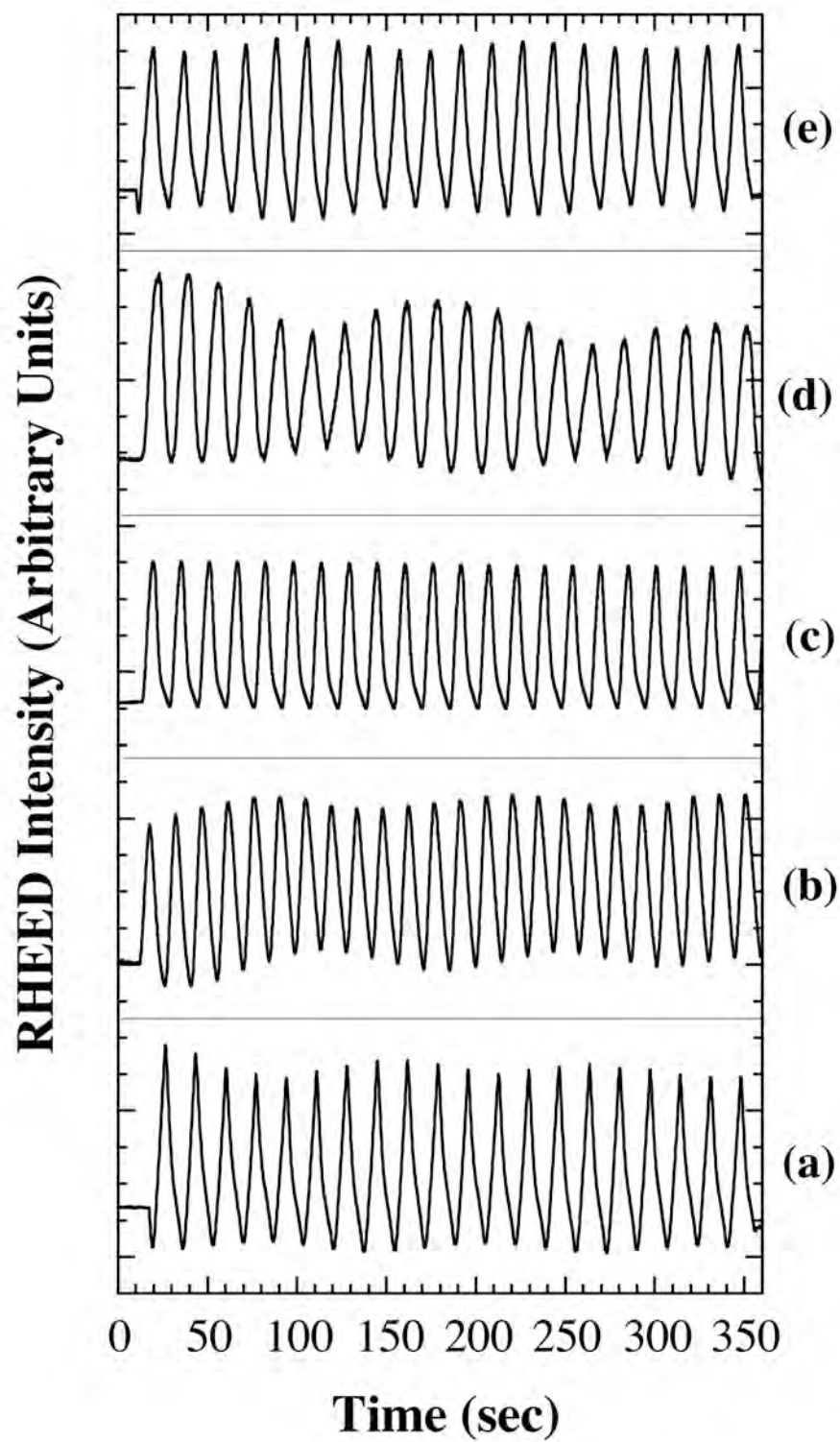
Fig. 3.2 RHEED oscillations for various monolayer coverages of Sr and Ti. (a) 85% (b) 90% (c) 100% (d) 110% (e) 115%.[10]

substrate termination. If the termination of the substrate is not perfect then the RHEED data will not show smooth oscillations. Poor substrate surface quality usually mimics a titanium rich sample, with a sharp decrease when the strontium shutter is opened, but it can have many other effects as well. This also tends to cause large problems at the beginning of the growth. For this reason, it was found that it is better to grow the first few monolayers manually, instead of using the computer control. In this way the termination can be fixed by adding additional amounts of the constituent elements and the calibrated times can be cross-checked. If this problem is not fixed early the entire growth can become quite difficult and the oscillations difficult to interpret. The next biggest problem is the so-called history effect. The RHEED is not completely surface sensitive, it detects the structure over a few monolayers, and typically growth is done at elevated temperatures where diffusion of elements is not negligible. This leads to a time lag in any changes made to the stoichiometry or dose. So the changes made during growth are not instant, typically these changes progress over a few monolayers. This effect can occur over many monolayers if the changes are subtle, as in the final stages of calibration. This can be seen in Fig. 3.3, where the doses were adjusted and it takes several monolayers before the oscillations become regular. So it is ideal to make gradual changes and observe how the oscillations change over time.

During heteroepitaxial growths, films will relax once they get beyond a critical thickness. This can be observed in RHEED by the diffraction spots becoming more diffuse. This can lead to an increase in the intensity of the RHEED oscillations. Though one might expect the integrated intensity of the diffraction rod should be the same
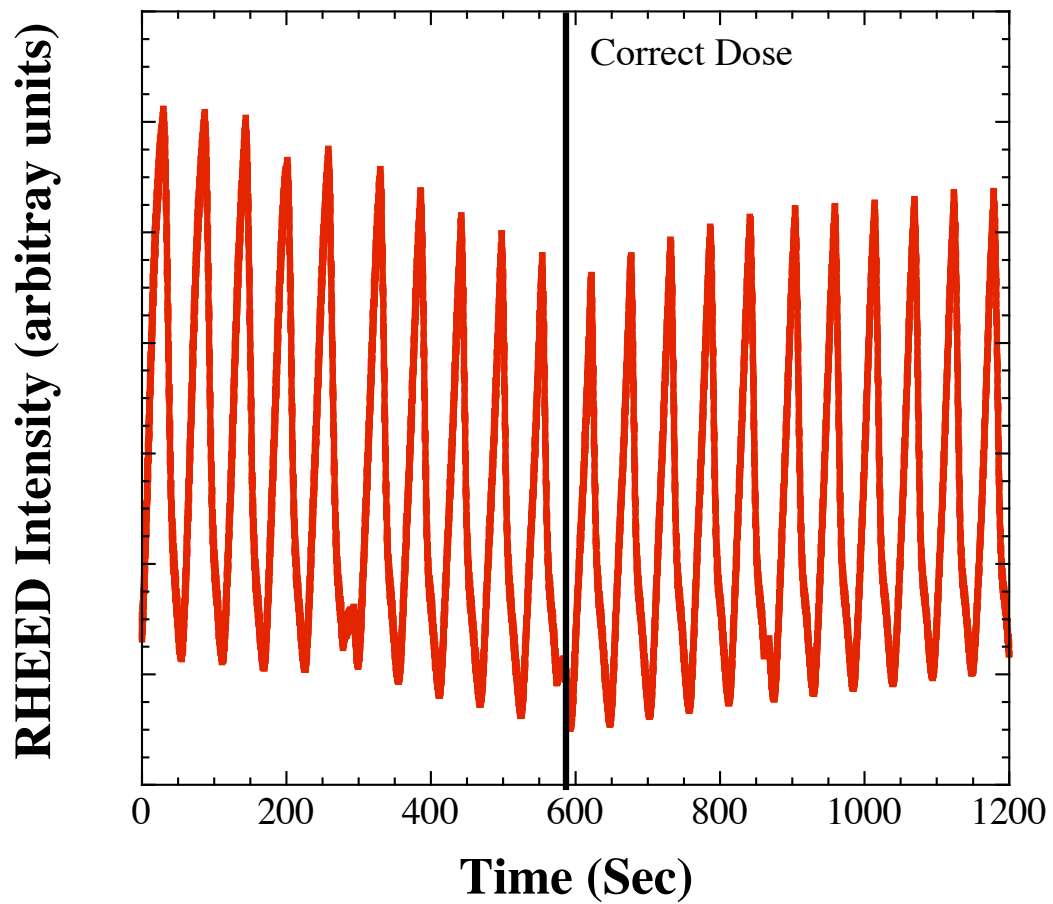
Fig. 3.3 RHEED oscillations during growth of $SrTiO_3$ on (110) $NdGaO_3$ substrates when

the dose was corrected (at vertical line) and the oscillations eventually become regular

.

regardless of how diffuse the spot is, this does not occur in practice. This is mainly due to the fact that the pixels are saturated when near the maximum intensity. So a slight decrease in the maximum intensity is not observed in the averaged intensity of the diffracted spot, but the increase in the surrounding pixels from the broadening of the spot contributes to the average intensity. This becomes very important for systems that relax slowly, and this increase in the intensity can be confused with a titanium-deficient stoichiometry. There are also some circumstances when the rods will change shape as the film grows. This has to be accounted for when making adjustments of the stoichiometry based on changes in the intensity.

Other problems that can occur relate more to stability. When growing in ozone, the sources tend to oxidize and their fluxes will change over time. To compensate for the reduced flux, the time for the shutter to be open changes. Background pressure can also change the intensity of the oscillations and the background pressure often drifts during the first few hours of growth. The increase in background pressure causes the intensity of the RHEED to decrease due to increased scattering of the electrons. The RHEED itself is not always particularly stable; the alignment of the RHEED tool can drift during a growth, especially if it is several hours long. This can also lead to decrease in the intensity of the RHEED.

Also of note, for this research it was rarely found that for heteroepitaxy the incorrect dose would give RHEED oscillations as nice as those of Fig. 3.2. These beat frequencies are not always observed. Rather, a decrease in intensity as shown in Fig. 3.3 was a more typical result. This decrease in intensity is not always recoverable and is probably due to a roughening of the film. The beat wave is also rarely a perfect envelope

wave; it often only affects the top or bottom of the peaks. This can be very difficult to discern under non-ideal conditions and can easily be mistaken as a stoichiometry problem.

One final point, the deconvolution of all the different factors can be very difficult. Different combinations of stoichiometry, dose errors, instabilities in the sources, termination problems and other problems can yield very similar results over a few oscillations. An ideal growth is achieved through trial and error, and so is a function of experience with the materials and equipment. Generally if the growth is proceeding poorly, the intensity of the RHEED oscillations will decrease. If there is any large deviation the intensity of the oscillations will decrease rapidly and extra spots can appear, signifying that the film is getting rough or there is a second phase. However, if growth parameters are perfect the oscillations will be very stable and consistent. High-quality growths do not always have the best RHEED patterns and low-quality films do not always have bad RHEED patterns. There are many challenges with this technique, but without it accurate growth of high quality multicomponent oxide films by MBE would be even more difficult.

3.2 X-ray Diffraction

X-ray diffraction is a tool that can yield information about the structure of a material. This generally consists of reflecting monochromatic x-rays from a sample and measuring the intensity of the x-rays reflected from the sample as a function of angle. This technique is based on Bragg's law: [15]

$$n\lambda = 2d \ \sin(\theta)$$
<div style="text-align: right;">Eq. 3.1</div>

where λ is the wavelength of the x-rays, d is the layer spacing, and θ is the angle and is depicted in Fig. 3.4. In this work a four circle diffractometer was needed. (However, in additional experiments on the synchrotron a grazing incident and a six circle x-ray diffractometer were used. The fundamentals are the same, except that the angle of incidence for these setups is kept near 1°.) The extra degrees of rotation, over a standard powder diffractometer, are necessary for probing epitaxial films. Whereas the θ and 2θ angles are needed to probe the crystal planes oriented parallel to the surface, the ϕ and χ angles must be used to examine planes not perpendicular to the surface.

For most of this work, a Phillips X'pert MRD[16] four-circle x-ray diffractometer was used with a hybrid monochromator (combined Gutmann mirror and a 4-bounce Ge (220) monochromator) on the incident side and a triple axis 2 bounce (220) Ge analyzer crystal. For higher intensity only the Gutmann mirror was used in place of the hybrid on the incident side. Additional measurements were made using synchrotron radiation at the BESSRC beamline 12-ID at the Advanced Photon Source located at Argonne National Laboratory. In these experiements a Huber grazing incident diffractometer[17] was used to study the in-plane lattice constants and a Huber six circle diffractometer17 was used for oxidation studies[18]. The optics arrangement at the APS is outlined in Fig. 3.5. The source at the APS was a 3.3 cm period, 2.4 m length undulator, which is typically operated to produce 24 keV photons using the third harmonic. The monochromator is a cryogenically cooled Si (1 1 1) crystal, located 30 m from the source. A singly bent mirror at 66 m focuses the beam onto a 10 μm vertical slit just before the sample chamber.19 The intensity passing through this slit (typically 10^{12} cps) is monitored and stabilized using a
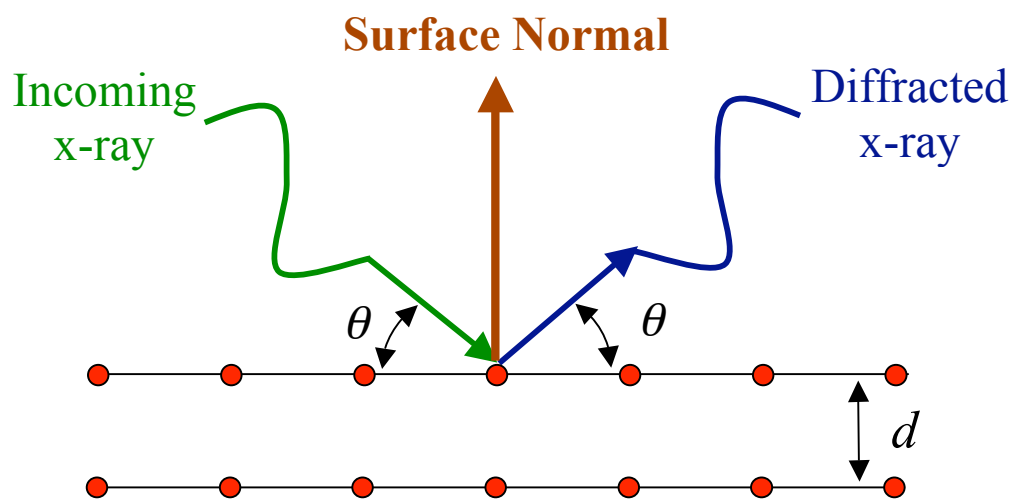
Fig. 3.4 Schematic of Bragg's law depicting the angle of reflection θ and the d-spacing.

Diffracted-
beam bicron
or CCD

Reflected
-beam TV
monitor

PIN diode
monitor —————— Feedback

SiO$_2$-wall
chamber
(2 mm thick)

10 µm slit

Piezo
±1 µrad

Undulator A
3.3 cm 2.4
m 3rd
harmonic 24

Sample
(72 m)

Vertically
Focusing
Mirror
(66 m)

Si (111)
Mono
(30 m)
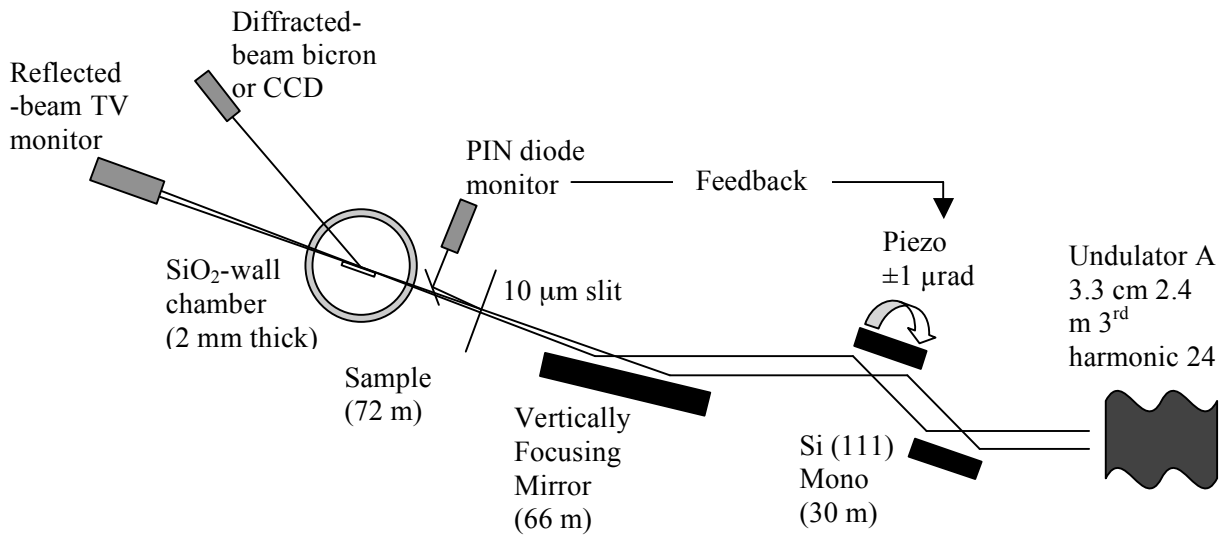
Fig. 3.5 Schematic of beamline optics at BESSERC 12-ID at the APS. (Note: the diagram

is not to scale.)[19]

feedback loop controlling the exact angle of the second monochromator crystal. Because of the focusing geometry, the angle changes required (<1 μrad) are much smaller than the Darwin width of the monochromator crystals. Typical signal levels are 10^5 cps in a crystal truncation rod. [19]

The four circle diffractometers were used in a Bragg-Brentano geometry to obtain symmetric reflections of planes with spacings between ~0.9 Å and 30Å, with a standard Cu anode. [20] With the four circle diffractometer there are four angles with which the diffractometer can move, 2θ, θ, ϕ, and χ. A schematic of these angles is given in Fig. 3.6 and the sample rotations for these angles are described in Fig. 3.7. Scanning the 2θ and θ circles together allows for the measurement of plane spacings. [15] This can give information on the planes parallel to the surface of the sample, and is very useful in identifying phase and out of plane orientation. Another piece of information on the crystalline quality of the film can be obtained by scanning only the θ circle with the 2θ circle fixed at an angle that satisfies Bragg's law. The difference between the $2\theta/2$ and θ is referred to as ω and these scans are often referred to as ω scans. [21] In practice this can be seen as rocking the sample about the center of the diffractometer; thus the scans can also be referred to as rocking curves. The width of the peak measured in the ω scan can be used to determine the mosaicity in the film. The wider the peak, the larger the volume of material with an orientation tilted away from the substrate normal. [21] This scan can also reveal if there is more than one orientation in the film (i.e. crystallites), seen as multiple peaks, which are usually templated from the substrate. This can also be done with the χ circle, but typically χ has lower resolution than the θ circle and is not used.
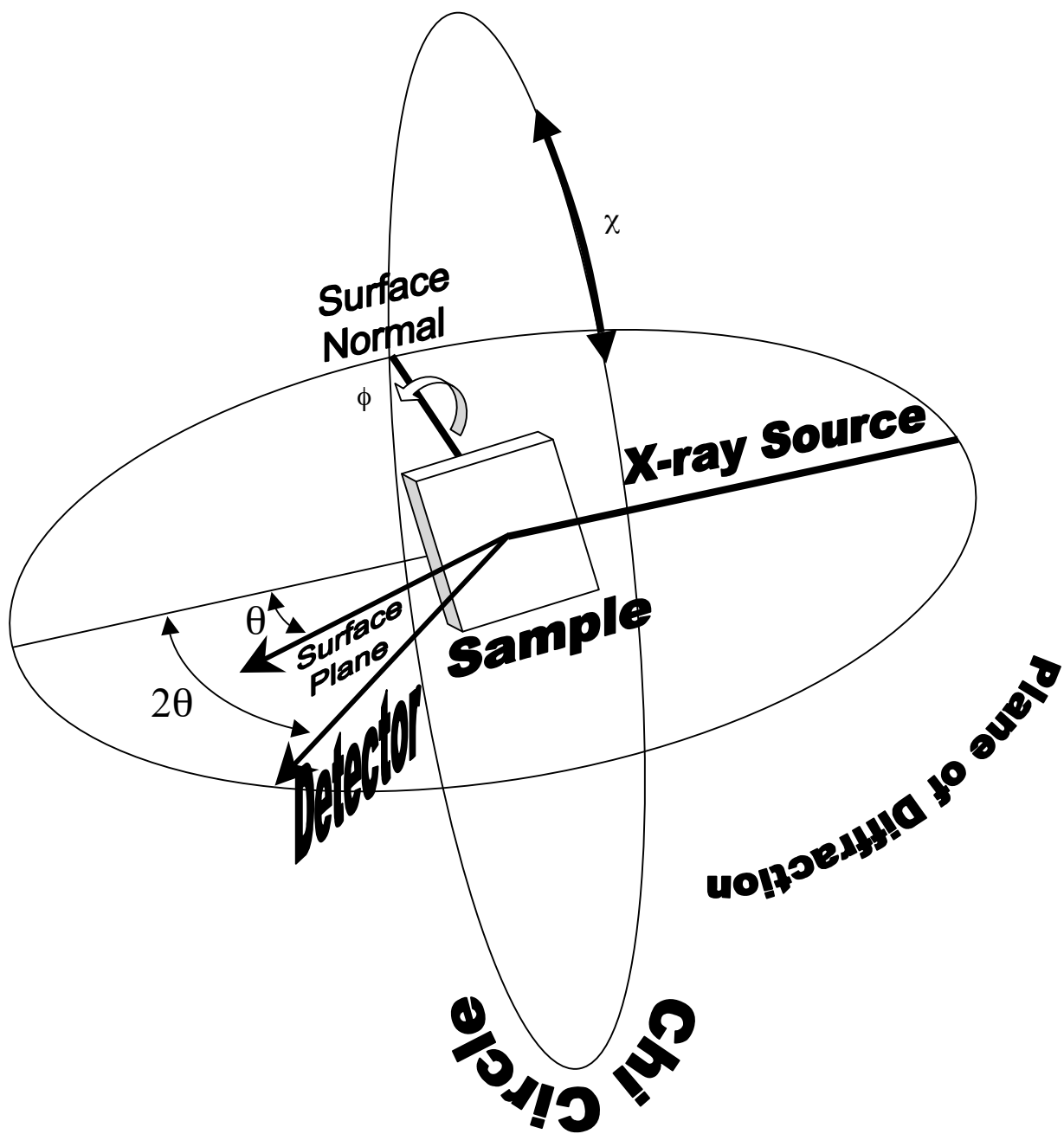
Fig. 3.6 Schematic of angles in a 4-circle diffractometer where the sample is represented

as the plate in the middle of the picture.
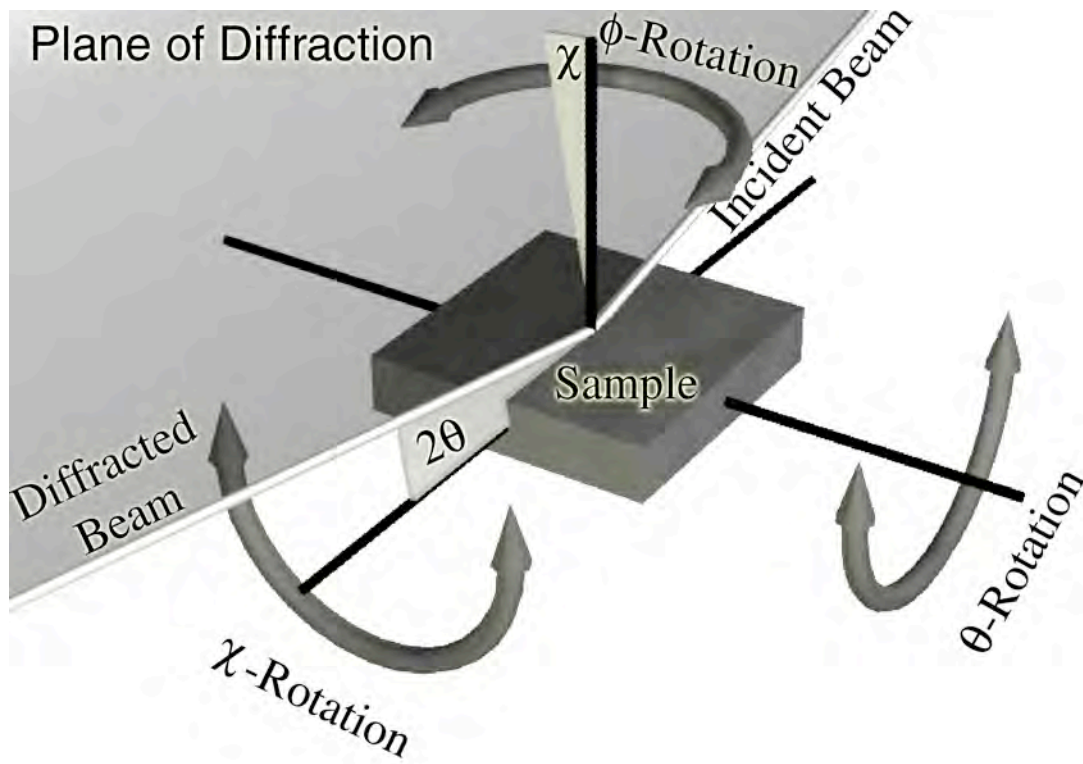
Fig. 3.7 Schematic of sample rotations for 4-circle diffractometer geometry defined in the previous figure (Fig. 3.6).

To examine off-axis crystallographic planes, (those that are not parallel to the surface of the film) the χ and ϕ circles must be rotated from their normal positions of 90° and 0° respectively. This is necessary to determine information about the epitaxy and in-plane lattice constants of the films. As an example, the (111) plane of a cubic crystal, such as unstrained bulk SrTiO$_3$ at room temperature, is shown in Fig. 3.8. If it is desired to bring the (111) into the surface of diffraction (nominally the (001) for on-axis scans), the χ must be rotated to 32.7° and the ϕ must be rotated to 45°. With a scan about the ϕ axis, information on the epitaxy and crystal structure can be determined. For cube on cube epitaxy, the 111 reflection will have four peaks in a 360° scan of the ϕ axis. When there are twins in the film, there will be a set of four peaks for each orientation. If the film had random orientation in plane, such as fiber texture, the ϕ scan will show a constant, non-zero intensity throughout the scan. Rocking curves can also be used off-axis to get an idea of the crystalline misorientation in-plane.

The 2θ position of on-axis and off-axis peaks was used to determine the size of the unit cell. For most of this work the 100, 011 and 101 peaks were measured to give the unit cell dimensions. The lattice parameters are related to the measured d spacings via the following equation:[15]

$$\frac{1}{d^2} = \frac{h^2}{a^2} + \frac{k^2}{b^2} + \frac{l^2}{c^2}$$

Eq. 3.2

and Bragg's law (Eq. 3.1) is used to get the d spacing for the respective reflections.

To minimize errors in the measurement of d a Nelson-Riley fit was used to extract systematic errors.[22] This technique was originally developed for the Debye-Scherrer
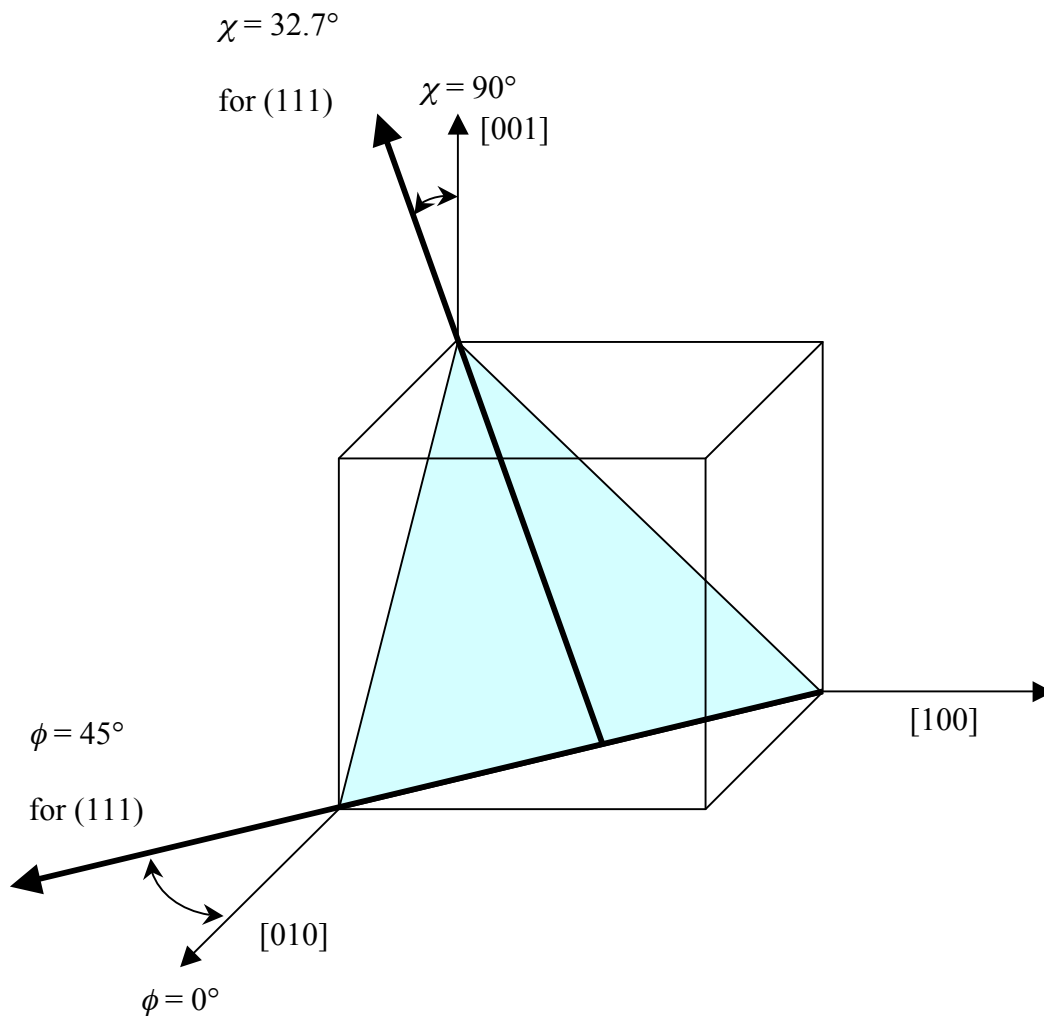
Fig. 3.8 Schematic of angles χ and ϕ (defined in 3.6) to probe the (111) with the x-ray beam for a cubic crystal. The x-rays probe to the (001) in a cubic crystal for the normal alignment, (i.e. $\chi = 90°$ and $\phi = 0°$). To probe the (111) the crystal must be rotated so that $\chi = 32.7°$ and $\phi = 45$ to allow for the diffraction from the (111) plane.

camera and includes a second term to account for anomalies in the specimen suspended in a capillary and anomalies in the radius of the camera. Thus the second term was ignored and only the first part was utilized in this fitting:

$$\frac{\Delta d}{d} = K\left(\frac{\cos^2\theta}{\sin\theta}\right)$$

Eq. 3.3

Thus plotting the calculated lattice parameter as a function of $\frac{\cos^2\theta}{\sin\theta}$ for a series of higher order planes and extrapolating this to zero yields the true lattice constant (Fig. 3.9).[22] It should be noted that this fitting is only completely valid for parafocusing geometries, but would be useful in other geometries for removing any systematic errors.[22] This also serves to give an idea of the accuracy of the determined lattice constant since a better linear fit indicates small random errors and a small slope indicates less systematic error.

3.3 Electrical Property Measurements

The capacitance measurements in this work were made using a HP 4284a LCR meter with various probes. The cryogenic data was measured in either a Delta Design D900 oven equipped with liquid nitrogen cooling or a Desert Cryogenics probe station.[23] Room temperature measurements were made using Cascade[24] or Micromanipulator[25] probe stations with cascade DCM 100 probes.[24] Ferroelectric measurements (P-E Hysteresis loops) were made using an Aixacct TF 2000 ferroelectric analyzer[26] or a Radiant Technologies RT-66a ferroelectric tester[27] with the probe stations described previously.
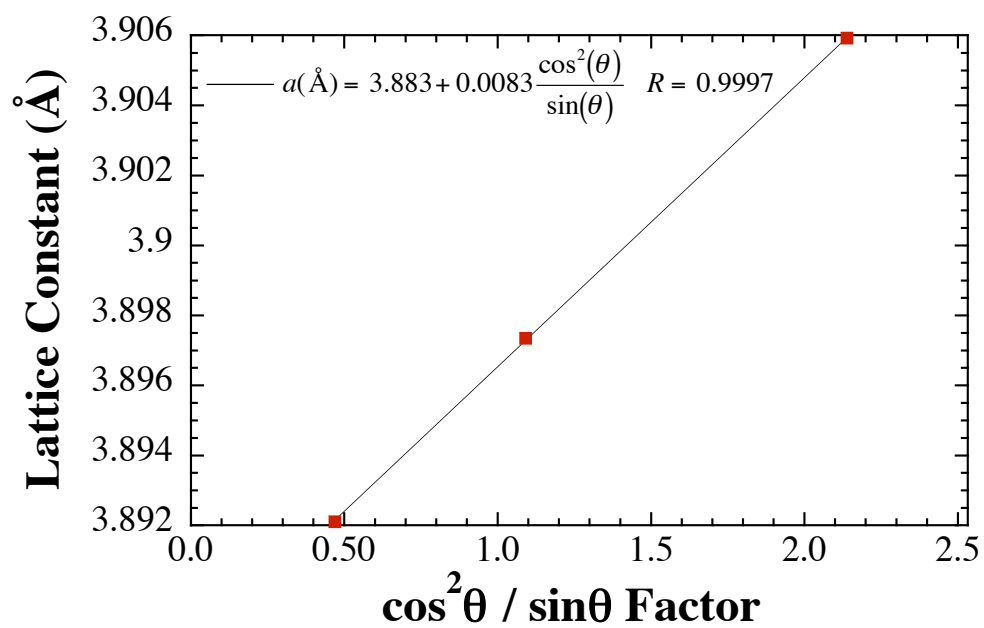
Fig. 3.9 Nelson-Riley fit of 00l peaks for a 250Å $SrTiO_3$ film grown on $DyScO_3$.

In this work the electric properties were all measured without a bottom electrode. This was necessary to avoid changing the strain state of the film as well as to avoid problems with the integrity of electrodes under MBE growth conditions. This necessitated the use of interdigitated electrodes (IDT) that are pictured in Fig. 3.10. These electrodes were made of thermally evaporated 1000 Å Au with a 100 Å Cr adhesion layer. They were patterned using a photolithographic lift off process with Shipley AZ nLOF 2020 photoresist.[28] A Karl Suss MA-6[29] contact aligner was used in hard contact mode to pattern the photoresist. The details are summarized in Table 3.1. The Au/Cr electrodes were then deposited using a Kurt J. Lesker thermal evaporator.[30] The photoresist was removed in a MicroChem NanoRemover PG bath[31], rinsed in deionized water, and blown dry with nitrogen.

Table 3.1 Summary of electrode photolithography parameters.

Spin parameters	Photoresist Thickness	Soft Bake	Exposure Time	Post Exposure Bake	Development Time	Hard Bake	Au Thickness	Cr Thickness
2500 rpm 40 sec	~1.5 μm	110 °C, 75 sec	2-3 sec	110 °C 75 sec	60 sec	110°C 1 min	1000 Å	100 Å

With IDT electrodes, the dielectric constant cannot be directly extracted from the measured capacitance. This is due to the non-uniform distribution of the electric field. To calculate the capacitance it is necessary to use conformal mapping.[32,33] This method can be quite involved, but a brief review of the basics will be presented. In this method the planar capacitor is transformed into a rectangular sandwich capacitor by the Christoffel-Schwarz transformation.[32-34] This allows for the calculation of the capacitance by:

$$C = \frac{1}{2}\varepsilon\varepsilon_0 \frac{K(k)}{K(k')} \qquad k' = \sqrt{1-k} \qquad \text{Eq. 3.4}$$

where C is the capacitance per unit length, ε_0 is the permittivity of free space and ε is the permittivity of the layer, $K(x)$ is the total elliptical integral of the first kind and k is a geometric factor that is dependent on the geometry of the electrode. For the case outlined in Fig. 3.11(a) k is:

$$k = \frac{\tanh\left(\dfrac{\pi \ s}{4h}\right)}{\tanh\left(\dfrac{\pi \ l}{4h}\right)} \qquad\qquad \text{Eq. 3.5}$$

where s is the gap between the fingers, l is the length of the gap, and two fingers are as defined in Fig. 3.11.[33] This is similar to the equation derived by Gevorgian $et\ al$, except, Gevorgian takes into account the fringing fields of neighboring strips for electrodes, electrode ends, and finite terminal thickness for interdigitated electrodes, as in Fig. 3.10.

In order to account for composite layers, as in the case of the films and utilized (Fig. 3.11(b)), the partial capacitance method must be employed.[35] This allows the measured capacitance ($C_{measured}$) to be modeled as three simple planar capacitors for the air (C_{air}), film (C_{film}) and substrate ($C_{substrate}$) connected in parallel:[33]

$$C_{measured} = C_{air} + C_{film} + C_{substrate} \qquad\qquad \text{Eq. 3.6}$$

with the permittivities modified as follows:[33]

$$\varepsilon^{*}_{film} = \varepsilon_{film} - \varepsilon_{substrate} \qquad\qquad \varepsilon^{*}_{substrate} = \varepsilon_{substrate} - 1 \qquad\qquad \text{Eq. 3.7}$$

Using these equations the dielectric permittivity of the film can be calculated from the known constants by:

$$\varepsilon_{film} = \varepsilon_{substrate} + \frac{C_{measured}}{A} - \frac{C_{air} + C_{substrate}}{A} \qquad\qquad \text{Eq. 3.8}$$

where C_{air} and $C_{substrate}$ are calculated using the formula in Eq. 3.6 (or the equivalent as described by Gevorgian $et\ al.$), and A is a constant that is calculated from the geometry of
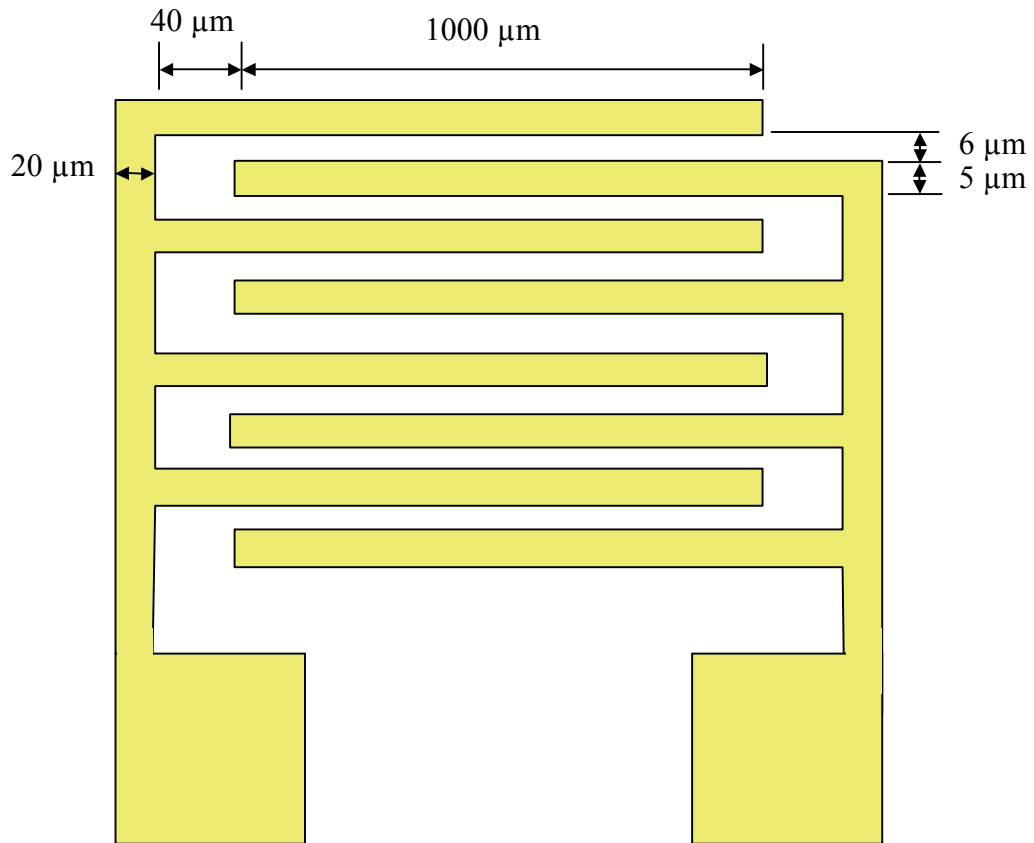
Fig. 3.10 Schematic of interdigitated electrode used for electrical measurements. Note that figure is not to scale and 35 or 48 fingers were used in this work to increase the capacitance.

the electrode.[32,33] It is important to note that the correct method is that described by

Gevorgian *et al.* that takes into account the fringe fields, the contributions from the

terminals, and end of the fingers. However, the IDT structure was designed to minimize

these effects it was found that the method described by Vendik et al. gives the same

results for the geometry of the electrodes used in this work as illustrated in Table 3.2. The

IDT electrodes do sample part of the out-of-plane component of the permittivity, but the

design of the IDT electrode was also designed to minimize these effects and they should

be negligible. It is also important to note that for very high contrasts between the

dielectric constants of the film and the substrate empirical models, such as those derived

by Farnell *et al.*[36] can give solutions that are within 10%, or better in some cases.[37-39]

Table 3.2 Comparison of different modeling methods to extract the dielectric constant

from the measured capacitance using Eq. 3.8 and the electrode structure used in this

work. (Note: Farnell's method cannot be used to calculate A, only the total capacitances)

Method	*Vendik[33]*	*Gevorgian[35]*	*Farnell[36]*
A (pF)	0.00242	0.00243	--
$C_{air}+C_{substrate}$ (pF) *(from third term in eq. 3.8)*	5.482	4.592	5.133
ε for 20 pF capacitance, for electrode geometry in Fig. 3.9	6179	6376	6006

3.4 Other Techniques

Other techniques utilized include high temperature x-ray diffraction, atomic force

microcopy (AFM), and transmission electron microscopy.

(a)
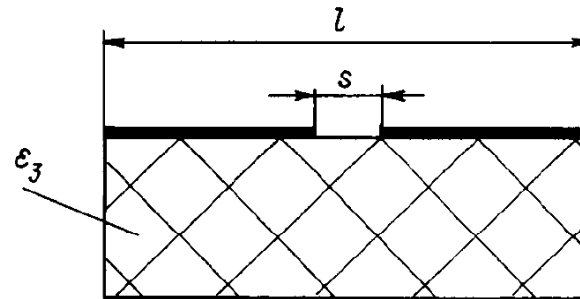
(b)
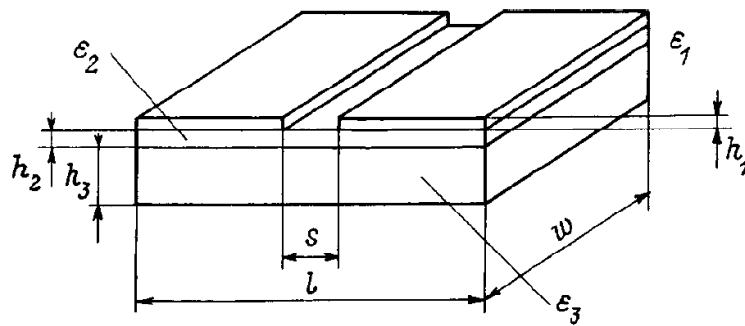
Fig. 3.11 Schematics of planar electrodes for (a) the simplest case of infinite strips on a bulk material and (b) strip electrodes on a substrate with a film.[33]

High temperature x-ray diffraction was performed on a Scintag X2 θ-2θ x-ray diffractometer.[40] This instrument was equipped with a Buehler HDK-2[41] horizontal hot stage with a 10% Rh-platium strip heater clamped to water cooled electrodes. A type S thermocouple is spot welded at the bottom-center of the strip, for both temperature measurement and heating control. Temperature control was through a Micristar Research[42] dual-input/dual-output programmable controller operated by DMSNT software from Scintag, Inc.[40]

AFM images were taken using a Metrology IIIA scanning probe instrument[43] equipped with a Si tip in intermittent contact mode at 0.6 Hz. All AFM measurements were made with the assistance of Marilyn Hawley at Los Alamos National Laboratory.

High resolution TEM images were aquired at the University of Michigan in Prof. Xiaoqing Pan's group. These measurements were made using a JEOL 4000[44] with a field emission source (see Sun *et al.* for details).[45]

References

[1] J. R. Arthur, J. Appl. Phys. **39**, 4032 (1968).

[2] A. Y. Cho, Surf. Sci. **17**, 494 (1969).

[3] Veeco Instruments, Inc., Edina, MN.

[4] Alpha Aesar, Ward Hill, MA.

[5] Varian, Inc., Palo Alto, CA.

[6] C. D. Theis and D. G. Schlom, J. Vac. Sci. Technol. A **14**, 2677 (1996).

[7] MKS Instruments, Wilmington, MA.

[8] Swagelok Corp., Solon, OH.

[9] Y. Horikoshi, M. Kawashima. and H. Yamaguchi, Japan J. Appl. Phys. **27**, 169 (1988).

[10] J. H. Haeni, C. D. Theis, and D. G. Schlom, J. Electroceram. **4**, 385 (2000).

[11] W. Braun, *Applied RHEED, Reflection High-Energy Electron Diffraction During Crystal Growth*, (Springer, Berlin, 1999).

[12] Staib Instrumente GmbH, Langenbach Germany.

[13] K-Space Associates, Inc., Ann Arbor, MI.

[14] A. Ichimiya and P. I. Cohen, *Reflection High Energy Electron Diffraction*, (Cambridge University Press, Cambridge, 2004).

[15] B. D. Cullity, *Elements of X-Ray Diffraction*: *Second Edition* (Addison-Wesley, Reading Massachusetts, 1978).

[16] PANalytical B.V, Almelo, Netherlands.

[17] Huber Diffraktionstechnik GmbH & Co. KG, Rimsting, Germany.

[18] P. H. Fuoss, J. A. Eastman, L. E. Rehn, P. M. Baldo, G.-W. Zhou, D. D. Fong, and L. J. Thompson, APS Science **5**, 119 (2005).

[19] G. B. Stephenson, D. D. Fong, M. V. Ramana Murty, S. K. Streiffer, J. A. Eastman, O. Auciello, P. H. Fuoss, A. Munkholm, M. E. M. Aanerud, and Carol Thompson, Physica B: Conden. Matter, **336**, 81 (2003).

[20] H. P. Kulug and L. E. Alexander, *X-ray Diffraction Procedures for Polycrystalline and Amorphous Materials* (John Wiley & Son,s Inc., New York, 1974).

[21] B. E. Warren, *X-ray Diffraction* (Dover Publications, Inc., New York, 1990).

[22] J. B. Nelson and D. P. Riley, Proc. Phys. Soc **57**, 160 (1945).

[23] Lake Shore Cryotronics, Inc., Columbus OH.

[24] Cascade Microtech, Inc., Beaverton, Oregon.

[25] The Micromanipulator Co., Inc., Carson City, NV.

[26] AixACCT Systems GmbH, Aachen, Germany.

[27] Radiant Technologies, Inc., Albuquerque, NM.

[28] Rohm and Haas Electronic Material, Philadelphia, PA.

[29] SUSS MicroTec Lithography GmbH, Munich, Germany.

[30] Kurt J. Lesker Company, Inc., Clairton, PA.

[31] MicroChem Co., Newton, MA.

[32] S. S. Gevorgian, T. Martinsson, P. L. Linner and E. L. Kollberg, IEEE Trans. Microwave Theory Tech. **44**, 896 (1996).

[33] O. G. Vendik, S. P. Zubko and M. A. Nikolskii, Zh. Tekh. Fiz. **69**, 1 (1999) [Sov. Phys. Tech. Phys. **44**, 349 (1999)].

[34] R. Schinzinger and P.A. Laura, *Conformal Mapping: Methods and Applications*, (Elsevier, Netherlands, 1991).

[35] S. S. Gevorgian, L. J. P. Linner, and E. L. Kollberg, IEEE Trans. Microwave Theory Tech. **43**, 772 (1995).

[36] G. Farnell, I. Cermak, P. Silverster, and S. Wong, IEEE Trans. Sonics and Ultrasoncis, **SU-17**, 188 (1970).

[37] K. Prume, S. Hoffmann and R. Waser, Integr. Ferroelectr., **32**, 63 (2001).

[38] J. Jin, S. T. Quek, and Q. Wang, Proc. R. Soc. Lond. A **459**, 1117 (2003).

[39] M. W. Otter, Sens. Actuators, A **96**, 140 (2002).

[40] Scintag, Inc., Cupertino, CA

[41] Buehler Co., Lake Bluff, IL.

[42] TMC Servies, Inc., Elk River, MN.

[43] Veeco Metrology, LLC, Santa Barbara, CA.

[44] JEOL Ltd., Tokyo, Japan.

[45] H. P. Sun, W. Tian, X. Q. Pan, J. H. Haeni, and D. G. Schlom, Appl. Phys. Lett. **84**, 3298 (2004).

Chapter 4

Characterization of DyScO$_3$ and GdScO$_3$ Substrates[*]

4.1 Abstract

The thermal expansion coefficients of DyScO$_3$ and GdScO$_3$ were determined from 298 K to 1273 K using x-ray diffraction. The average thermal expansion coefficients of DyScO$_3$ and GdScO$_3$ are 8.4 ppm/K and 10.9 ppm/K, respectively. No phase transitions were detected over this range, though the orthorhombicity decreased with increasing temperature. These thermal expansion coefficients are similar to other oxide perovskites (e.g., BaTiO$_3$ or SrTiO$_3$), making these rare earth scandates promising substrates for the growth of epitaxial thin films of many oxide perovskites that have similar lattice spacing and thermal expansion coefficients. These materials have dielectric constants ranging from 19 to 36 depending on direction with no dielectric anomalies from 4.2 K to 450 K, very little temperature dependence and low losses. Thus the materials enable dielectric measurements of thin films.

4.2 Introduction

The rare earth scandates are of interest as candidate substrates for the epitaxial growth of perovskite and perovskite-related films.[1,2] These scandates have pseudocubic lattice constants in the range of 3.93 to 4.05 Å. This range is devoid of commercially available perovskite substrates suitable for high temperature epitaxial film growth.[3] This is of particular importance to the growth of ferroelectric perovskites such as $(Ba,Sr)TiO_3$ and $Pb(Zr,Ti)O_3$ or electron-doped cuprate superconductors like $Sr_{0.9}La_{0.1}CuO_2$.[2] An important aspect for the growth of films on these substrates is knowledge of their thermal expansion coefficients. The only rare earth scandate whose thermal expansion behavior has been reported to date is $NdScO_3$.[4] The temperature range however, over which its thermal expansion behavior was reported, 1000°C to 2000°C,[4] is higher than the typical growth temperatures for perovskite thin films.

The rare earth scandates have the chemical formula $ReScO_3$, where Re is a rare earth element. At room temperature all $ReScO_3$, with Re = Ho to La, have the orthorhombic GeFeO$_3$ crystal structure (space group 62-*Pnma*).[3-10,*] They are isostructural with the commercial perovskite substrate materials $NdGaO_3$ and $YAlO_3$, as well as the conducting

---

[*] Throughout this manuscript we use the standard setting of space group #62, *Pnma*, to describe the crystallography of $DyScO_3$ and $GdScO_3$. Although some authors use this setting,[5,6,15] many others use the non-standard setting *Pbnm* to describe the crystallography of $DyScO_3$, $GdScO_3$, and other perovskites with the GdFeO$_3$ crystal structure.[1,3,4,7-10] The conversion from axes *a,b,c*, directions [*a b c*] or planes (*a b c*) in *Pnma* to *a′,b′,c′*, [*a′ b′ c′*], or (*a′ b′ c′*) in *Pbnm* is given by *a′=c, b′=a,* and *c′=b*.[6]

perovskite SrRuO$_3$,[11] which is commonly used as an epitaxial electrode in epitaxial perovskite thin film heterostructures.[8] This structure contains four formula units per unit cell, and hence, four pseudo-cubic perovskite subcells (Fig. 4.1). These materials have a distorted perovskite crystal structure consisting of near ideal corner-sharing ScO$_6$ oxygen coordination octahedra with distorted ReO$_{12}$ polyhedra. The Sc-O-Sc angles between octahedra are 139°-144°, where the ideal cubic perovskite has Sc-O-Sc angles of 180°.[5] This crystal system can be described using Glazer's notation as a$^-$b$^+$a$^-$.[12,13] For the orthorhombic system this equates to a tilt system of a$^-$b$^+$c^0, since Glazer described the tilts in terms of the pseudo cubic cell.[14] Thus, the symmetry of the system can be described by two tilts of the oxygen octahedra, one in-phase tilt along the a axis, as illustrated in Fig. 4.2(a), and an antiphase tilt along the a-axis as shown in Fig. 4.2(b).

Many perovskites including BaTiO$_3$, (Ba$_{1-x}$Sr$_x$)TiO$_3$, Pb(Zr$_{1-x}$Ti$_x$)O$_3$, and SrRuO$_3$ have pseudocubic lattice constants in the range of 3.9 to 4.1 Å (Fig. 4.3).[7-16] There are very few perovskite single crystals with lattice constants in this range that are grown in sufficient size to be used as substrates (i.e., with dimensions ≥10 mm×10 mm). The substrates that do exist in this range have problems with volatility or phase transitions (i.e., KTaO$_3$ or BaTiO$_3$).[17] This complicates epitaxial growth of high quality films of perovskite or perovskite–related materials with pseudocubic lattice constants in the 3.9 to 4.1 Å range. The rare earths scandates have the potential to alleviate this problem. Their pseudo-cubic perovskite lattice constant can be tailored in approximately 0.01 Å steps from 3.93 Å (for HoScO$_3$) to 4.05 Å (for LaScO$_3$) by varying the rare earth.[3] Unfortunately HoScO$_3$ does not melt congruently,[18] but DyScO$_3$, GdScO$_3$, SmScO$_3$, and NdScO$_3$ all melt congruently at about 2100 °C.[18,19] This makes production of large single

(a)

(b)

c

a

b

Rare Earth   Scandium   Oxygen
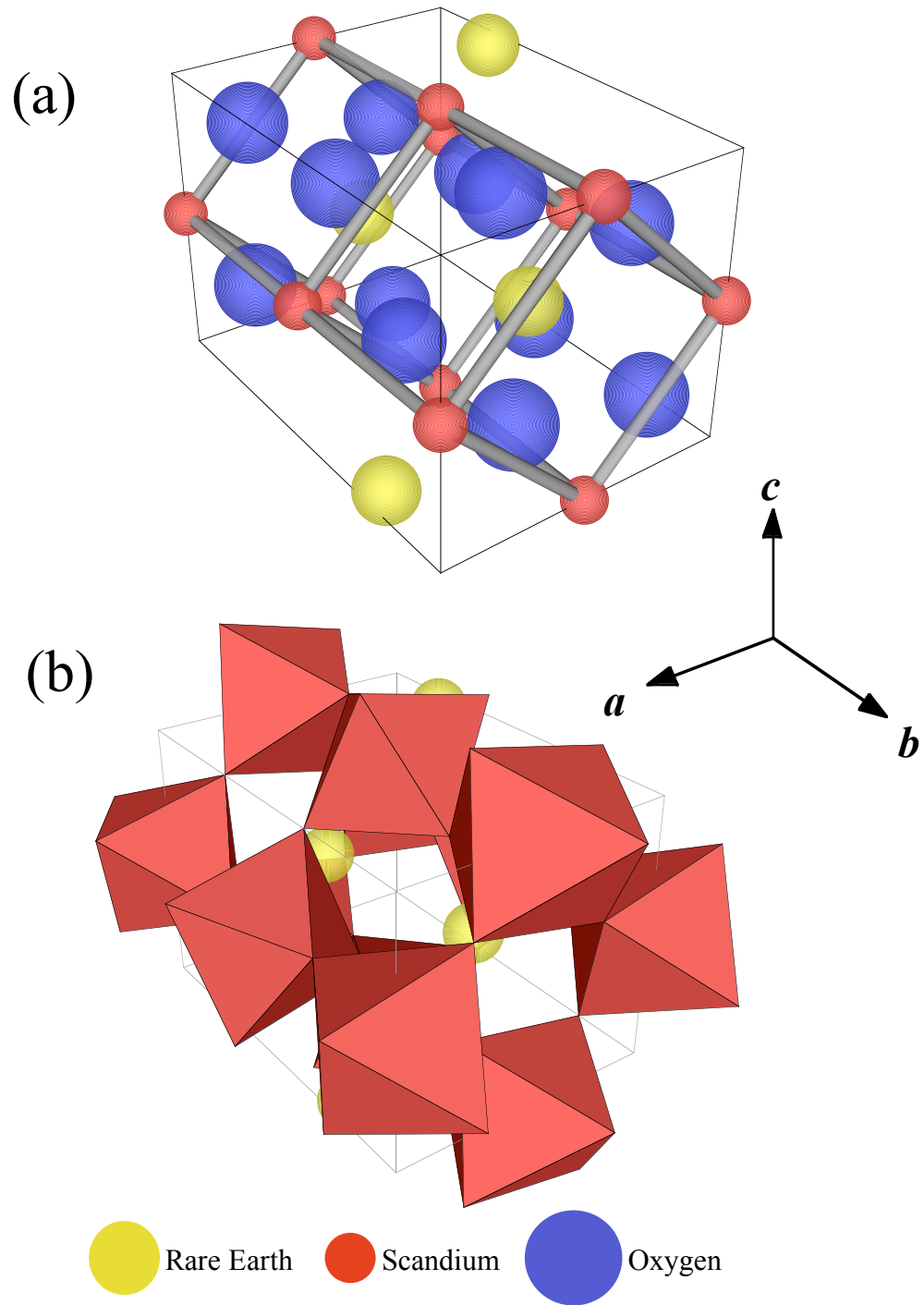
Fig. 4.1 Orthorhombic GdScO$_3$ crystal structure showing (a) pseudo-cubic cells inside an orthorhombic unit cell and (b) the tilting of the ScO$_6$ oxygen coordination octahedra.[5] The GdScO$_3$ structure data is from Ref. 5.
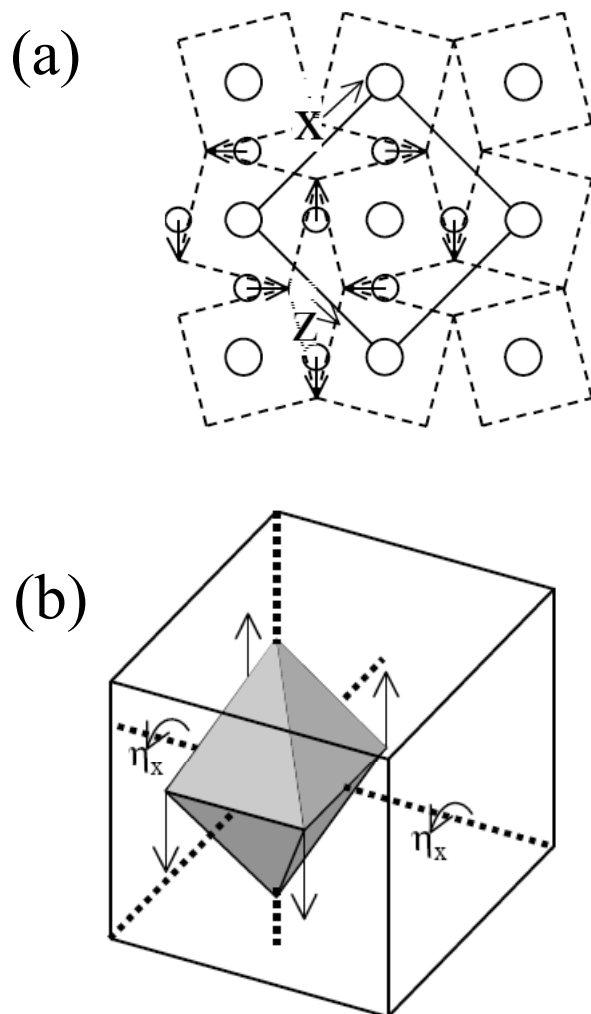
Fig. 4.2 Schematics of the tilts in the Pnma orthorhombic system. (a) Sketch of the a-c plane with the tilt about the b axis showing the displacements of the oxygen atoms from their cubic positions (Oxygen are smaller atoms, Sc are larger atoms). (b) Schematic of tilt around the a axis of the oxygen octahedra (η_x), illustrating the movement of the ScO_6 octahedra.[14]
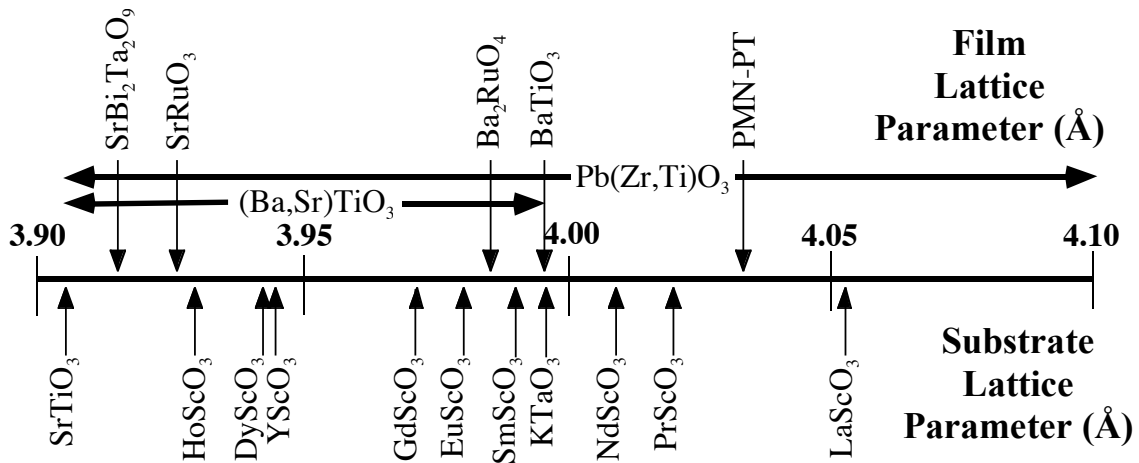
Fig. 4.3 Pseudo-cubic lattice constants from Refs. 3 and 8-16 for the rare earth scandates and other perovskites and perovskite-related oxides at room temperature. (PMN-PT is a 70% $PbMg_{0.33}Nb_{0.66}O_3 - 30\%$ $PbTiO_3$ solid solution).

crystals by the Czochralski method viable. The availability of such single crystals would allow for the growth of perovskite thin films not only on lattice-matched substrates, but also on substrates with chosen mismatch to precisely control the strain in the perovskite films.

Strain induced in a film by the underlying substrate can have significant effects on the properties and microstructure of perovskite thin films.[20–32] The influence of a substrate on residual strains arises from epitaxial strain due to lattice mismatch, thermal expansion strain (arising from the difference in thermal expansion coefficients between film and substrate) and other factors, including crystallite coalescence.[33] As mentioned earlier in this section, the only rare earth scandate whose thermal expansion behavior has been determined is $NdScO_3$.[4] Therefore, in this work the thermal expansion coefficients of two more rare earth scandates, $DyScO_3$ and $GdScO_3$, are examined over a temperature range of 298 to 1273 K (the temperature range of interest for perovskite thin film growth) using x-ray diffraction.

4.3 Experimental Procedure

Single crystals of $DyScO_3$ and $GdScO_3$ were grown by the float-zone method as described elsewhere.[34] These crystals were then powdered in a mortar and pestle to pass through a 120 mesh sieve, pressed into thin pellets, and sintered at 1200 °C for 3 h. The pellets were then polished to remove impurities from processing and to each a small amount of MgO powder was added to the surface to serve as a calibration standard.

X-ray diffraction data were taken on a Scintag X2 θ-2θ x-ray diffractometer. This instrument was equipped with a Buehler HDK-2 horizontal hot stage with a 10% Rh-platium strip heater clamped to water cooled electrodes. A type S thermocouple is spot

welded at the bottom-center of the strip, for both temperature measurement and heating control. Temperature control was through a Micristar Research Inc. dual-input/dual-output programmable controller operated by DMSNT software from Scintag, Inc. The data were collected over a 2θ range of 20-115° with a scan rate of 0.25°/min. The samples were heated at a rate of 10 °C/min and equilibrated for 10 min every 100 °C before x-ray data were acquired. The temperature stage was able to maintain its temperature within 1 °C of the set point.

Cell parameters for the powders were calculated utilizing the Pawley method, with whole pattern fitting in JADE software (Materials Data Inc., Livermore, CA). All refinements had R_{wp} values less than 15.[‡] The MgO was used as a standard for analyzing the pattern to account for the systematic errors due to specimen displacement typical in metal strip heaters. The pseudo-Voigt peak fitting function was used to fit the peak profile of the x-ray diffraction pattern and a cubic-spline function was used to describe the background.

For dielectric measurements, single crystals of DyScO$_3$ and GdScO$_3$ were grown by Czochralski and cut along the principal directions, and polished. Au electrodes were thermally evaporated on the surface of the crystal. The crystals were then cut into roughly 7x7 mm squares. The dielectric constants of these squares were measured using a HP 4284a LCR meter and a Delta Design 9000 oven over the temperature range of 150 K to 450 K and a He dipper rod was used to measure down to 4.2 K.

[‡] Values of R_{wp} of 15 are generally regarded as accurate fits, however values less than 10 are needed to extract atomic positions. Thus, atomic positions are not presented here.

4.4 Results and Discussion

4.4.1 Thermal Expansion

An internal MgO standard was used to examine the accuracy of the measurements. The room temperature lattice constant of MgO was determined to be 4.210 ± 0.003 Å, in good agreement with the literature value of 4.2117 ± 0.0002 Å.[35] The MgO thermal expansion data also agreed within experimental error to values reported by other researchers (Fig. 4.4). [36]

The lattice parameters of $DyScO_3$ and $GdScO_3$ were determined from the x-ray data (Fig. 4.5). The room temperature lattice constants of $DyScO_3$ were $a=5.720 \pm 0.003$ Å, $b=7.890 \pm 0.003$ Å, and $c=5.442 \pm 0.003$ Å, which agree well with the reported lattice parameters of $a=5.713$ Å, $b=7.887$ Å, and $c=5.440$ Å.[9] The $GdScO_3$ lattice parameters also agreed well with reported values. The room temperature lattice constants determined in this study were $a=5.755 \pm 0.003$ Å, $b=7.936 \pm 0.003$ Å, and $c=5.489 \pm 0.003$ Å (ICDD values: $a=5.746 \pm 0.003$ Å, $b=7.934 \pm 0.003$ Å, and $c=5.488 \pm 0.003$ Å).[10] These values were within the errors of the measurement except for the a axis. This difference might be attributed to stoichiometry differences between the samples, as has been noted in other $GdFeO_3$-type compounds.[37]

The x-ray data were fit using a *Pnma* space group as described previously.[5] The space groups $R\bar{3}c$, *Cmcm* and *I4/mcm* were also used to model the data, but resulted in poorer fits. The *Pnma* space group described all the peaks in the data and matched the intensities of the pattern. No change in space group was observed over the 298-1273 K
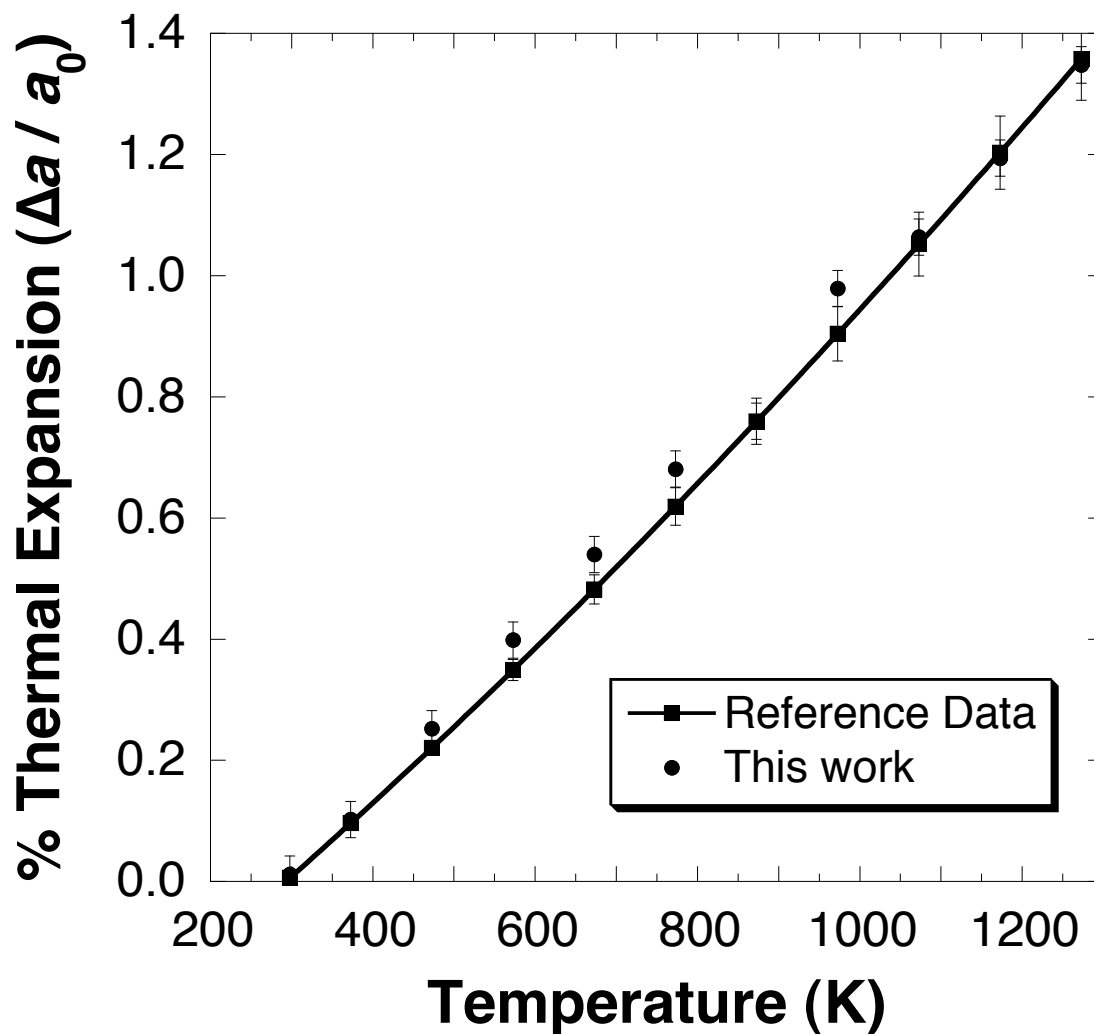
Fig. 4.4 Thermal expansion for MgO, $\Delta a / a_0$ where a_o is at 293 K, compared to reference

data from Ref. 35. The error bars for the MgO data reflect the 90% confidence interval

for three different data sets.
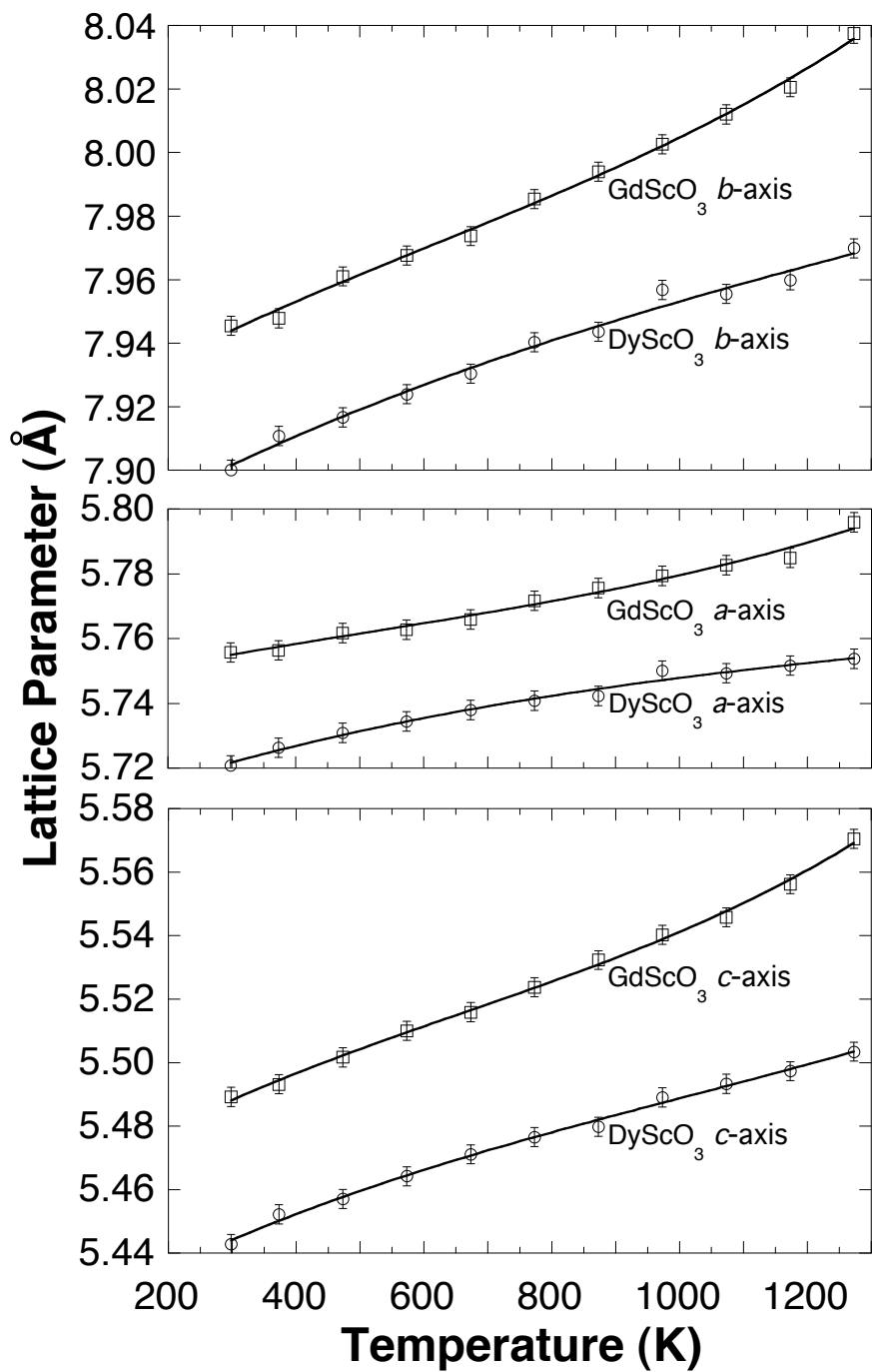
Fig. 4.5 Lattice parameters, in Å, as a function of temperature from 298-1273 K for

DyScO₃ and GdScO₃. The curves through the data points are polynomial fits.

temperature range. This absence of a transition agrees with measurements of capacitance as a function of temperature over the 4 K–523 K range for $DyScO_3$ and $GdScO_3$.[34] The lattice parameter data were fit to a fourth degree polynomial to obtain the lattice constants as a function of temperature.

For $DyScO_3$ the lattice parameters' dependence on temperature (T) in (K) were:

$$a = 5.682 + 2.105 \times 10^{-5} T - 3.400 \times 10^{-8} T^2 + 2.833 \times 10^{-12} T^3 + 8.7484 \times 10^{-14} T^4 \text{ Å}, \qquad \text{Eq. 4.1}$$

$$b = 7.880 + 5.011 \times 10^{-5} T + 1.067 \times 10^{-7} T^2 - 1.2872 \times 10^{-10} T^3 + 4.458 \times 10^{-14} T^4 \text{ Å}, \qquad \text{Eq. 4.2}$$

and $c = 5.397 + 2.3052 \times 10^{-4} T - 3.128 \times 10^{-7} T^2 + 2.460 \times 10^{-10} T^3 - 7.142 \times 10^{-14} T^4 \text{ Å}$ Eq. 4.3

For $GdScO_3$ the fit to the temperature dependence of the lattice constants was found to be:

$$a = 5.780 - 1.938 \times 10^{-4} T + 5.017 \times 10^{-7} T^2 - 4.609 \times 10^{-10} T^3 + 1.521 \times 10^{-14} T^4 \text{ Å}, \qquad \text{Eq. 4.4}$$

$$b = 7.948 - 1.072 \times 10^{-4} T + 4.435 \times 10^{-7} T^2 - 4.278 \times 10^{-10} T^3 + 1.483 \times 10^{-13} T^4 \text{ Å}, \qquad \text{Eq. 4.5}$$

and $c = 5.494 + 1.150 \times 10^{-4} T + 4.523 \times 10^{-7} T^2 - 4.479 \times 10^{-10} T^3 + 1.575 \times 10^{-13} T^4 \text{ Å}$. Eq. 4.6

The thermal expansion can be accounted for in two ways: (1) the elongation of the bonds and (2) the tilting of the ScO_6 octahedra. Rotation of the octahedra is possible without changing the space group.[7,38] $DyScO_3$ and $GdScO_3$ are distorted perovskites in which the oxygen octahedra is rotated around their three–fold axes by an angle Φ.[7,38] This tilting of the octahedra does not affect the principle axes equally, yielding an orthorhombic structure. When the material is heated, the crystal structure goes towards a higher symmetry structure; this reduces rotation of the octahedra.[39] Thus, the thermal expansion is expected to be anisotropic.[39,40] This is reflected by the linear thermal expansions in Table 4.1 and is consistent with the thermal expansion anisotropy observed in other $GdFeO_3$-type materials,[41,42] including $NdScO_3$.[4] The thermal expansion anisotropy is also

found to follow the order $\alpha_{33} > \alpha_{22} > \alpha_{11}$ in other GdFeO$_3$ type materials.[4,37,40-42] This anisotropy for the GdFeO$_3$-type materials stems from the crystal structure. Fig. 4.6 shows projections along the [100] and [001] directions of the GdScO$_3$ unit cell. From this figure, it can be seen that tilting of the octahedra affects the length of the *b* and *c* axes of the unit cell much more than the *a* axis. Thus, the thermal expansion along the *a* axis is expected to be much closer to the thermal expansion of the Sc-O bonds and therefore smaller than the thermal expansion along the *b* and *c* axis, where the rotation of the octahedra has a more pronounced effect.

 Table 4.1 Linear thermal expansion coefficients over the range of 293-1273 K, showing the anisotropy of the thermal expansion.

	DyScO$_3$ (10^{-6}/K)	GdScO$_3$ (10^{-6}/K)
α_{11}	5.7	6.7
α_{22}	8.6	11.5
α_{33}	11.0	14.5
Average	8.4	10.9

Fig. 4.6 Orthographic view of the orthorhombic GdScO$_3$ unit cell at room temperature along the (a) [100] and (b) [001]. The ScO$_6$ units are represented by octahedra. The GdScO$_3$ structure data is from Ref. 5.

The approximation of the thermal expansion along the *a* axis being due only to the Sc-O bond expansion can be examined using the model described by Zhao and Weidner[40] for the thermal expansion of distorted perovskites. If we assume the ScO_6 octahedra are regular, and the thermal expansion due to tilting of the octahedra and expansion of Sc-O bonds are decoupled, then the volumetric thermal expansion α_V can be broken into two parts:[39,43]

$$\alpha_V = \alpha_{Vo} + \alpha_\Phi, \qquad \text{Eq. 4.7}$$

where α_{Vo} is the volumetric expansion of the cubic structure due to the expansion of the Sc-O bonds and α_Φ is the thermal expansion due to the tilting of the ScO_6 octahedra. By comparing the volumetric thermal expansion to the one calculated from Eq. 4.7, the accuracy of the assumption that the thermal expansion of the *a* axis is due to the expansion of the Sc-O bonds can be examined. The tilting as a function of temperature was calculated using a geometrical factor (Fig. 4.7):[40]

$$\cos\Phi = \frac{\sqrt{2} \cdot a^2}{b \cdot c}. \qquad \text{Eq. 4.8}$$

This gives an α_Φ of 0.70×10^{-5} K^{-1} and 1.05×10^{-5} K^{-1} for DyScO$_3$ and GdScO$_3$, respectively. If we assume that the thermal expansion along the *a* axis is due only to extension of the Sc-O bonds, then we can calculate α_{Vo} from the thermal expansion of the *a* axis. This gives $\alpha_{Vo}=1.72\times10^{-5}$ K^{-1} for DyScO$_3$ and $\alpha_{Vo}=2.02\times10^{-5}$ K^{-1} for GdScO$_3$. Applying Eq. 4.7 yields $\alpha_V=2.42\times10^{-5}$ K^{-1} and $\alpha_V=3.07\times10^{-5}$ K^{-1} for DyScO$_3$ and GdScO$_3$, respectively, which are very close to the measured values of $\alpha_V=2.55\times10^{-5}$ K^{-1}
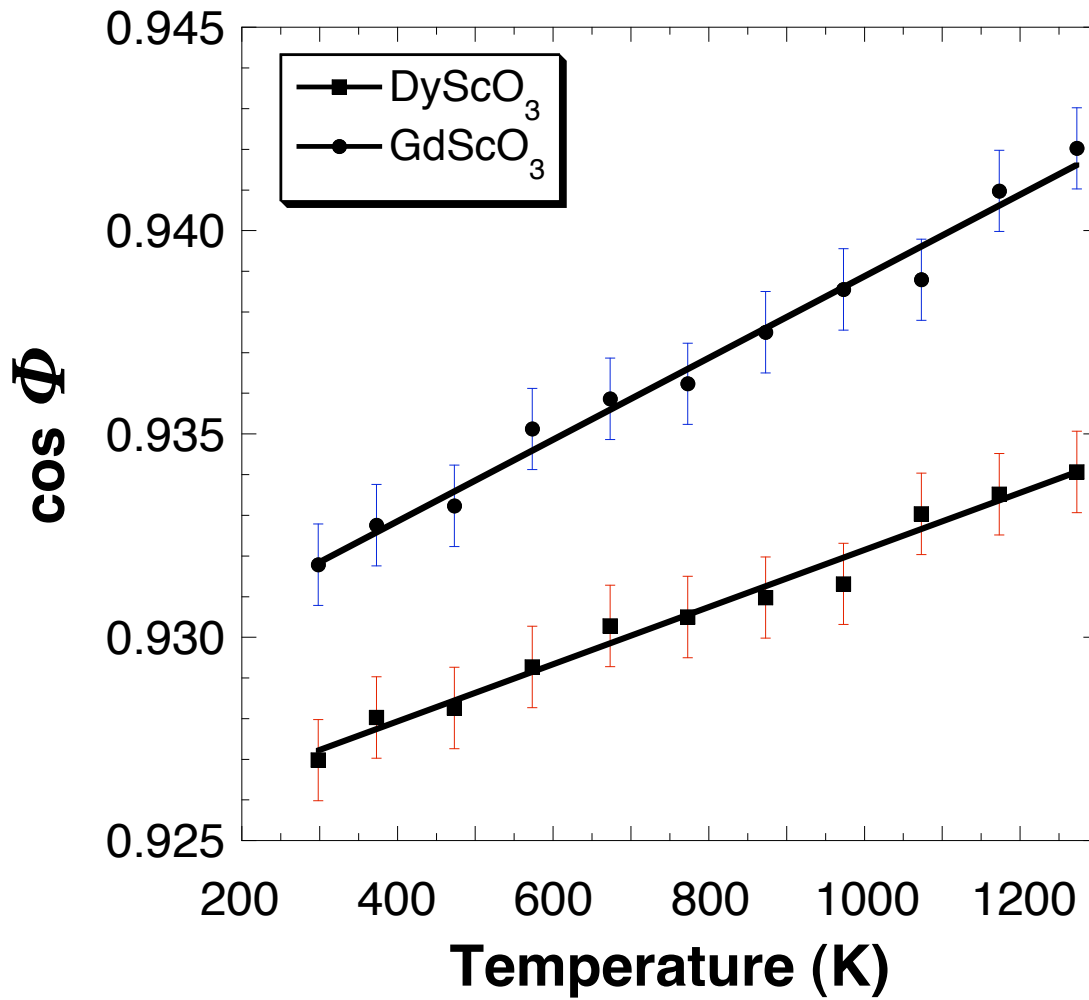
Fig. 4.7 Plot of *cos Φ* as a function of temperature for DyScO₃ and GdScO₃, showing the decrease in the rotation of the octahedra as temperature is increased. (Note: error bars are for the data; the error of the calculation is dependent on the accuracy of the assumptions used to simplify the equation as defined in Ref. 6.)

for DyScO$_3$ and α_V=3.31×10^{-5} K^{-1} for GdScO$_3$. The quality of this approximation confirms that the assumptions are reasonable: that the thermal expansion along the *a* axis is due mostly to the expansion of the ScO$_6$ octahedra and the thermal expansion anisotropy is mostly due to the rotation of the octahedra.

As the temperature increases, the *c/a* ratio gets closer to unity, reducing the orthorhombicity of the cell (Fig. 4.8). This is common in other GdFeO$_3$-type crystals, where many transform to cubic or tetragonal symmetries at elevated temperatures.[11,37,40,45] It is seen from Fig. 4.7 that a transition is still far away at 1273 K for DyScO$_3$ and GdScO$_3$. This agrees with the small perovskite tolerance factors of these compounds (0.85 and 0.87, respectively, using Shannon – Prewitt radii).[46,47]

The pseudocubic lattice parameters as a function of temperature for DyScO$_3$ and GdScO$_3$ are compared to other perovskite materials in Fig. 4.9. Since each unit cell contains four formula units, the pseudo-cubic lattice constant is given by:

$$a_{pseudo} = \sqrt[3]{V/4} = \sqrt[3]{\frac{a\ b\ c}{4}}, \qquad \text{Eq. 4.9}$$

where V is the unit cell volume, *a, b,* and *c* are the unit cell lattice constants, and a_{pseudo} is the pseudo-cubic lattice constant. The thermal expansion of a_{pseudo} is close to the average linear thermal expansions of many other oxide perovskite materials.[4,11,15,48] This makes DyScO$_3$ and GdScO$_3$ good candidate substrates for the epitaxial growth of oxide perovskites.
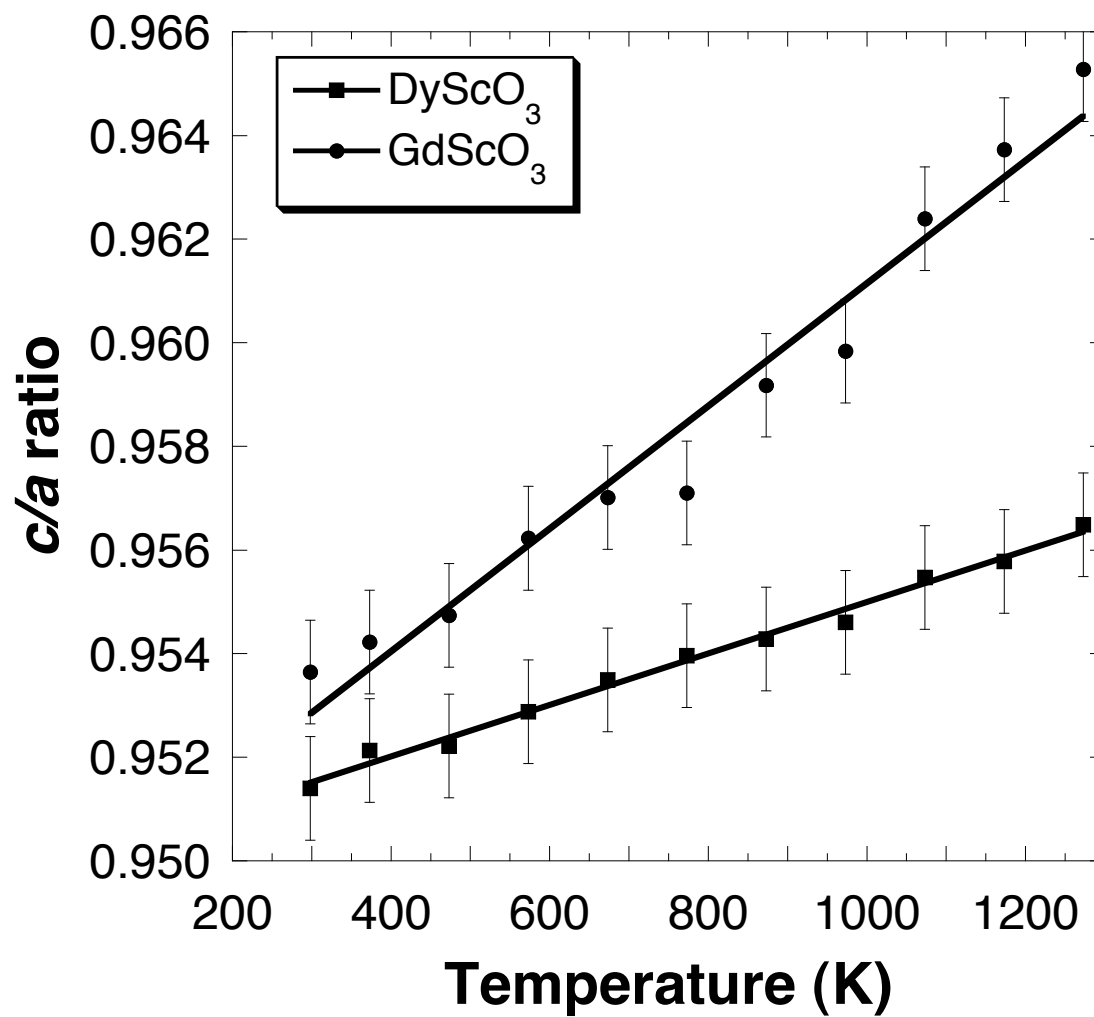
Fig. 4.8 Ratio of unit cell parameters *c* to *a* as a function of temperature, showing a

decrease in the orthorhombicity of the unit cells of $DyScO_3$ and $GdScO_3$ with

temperature.
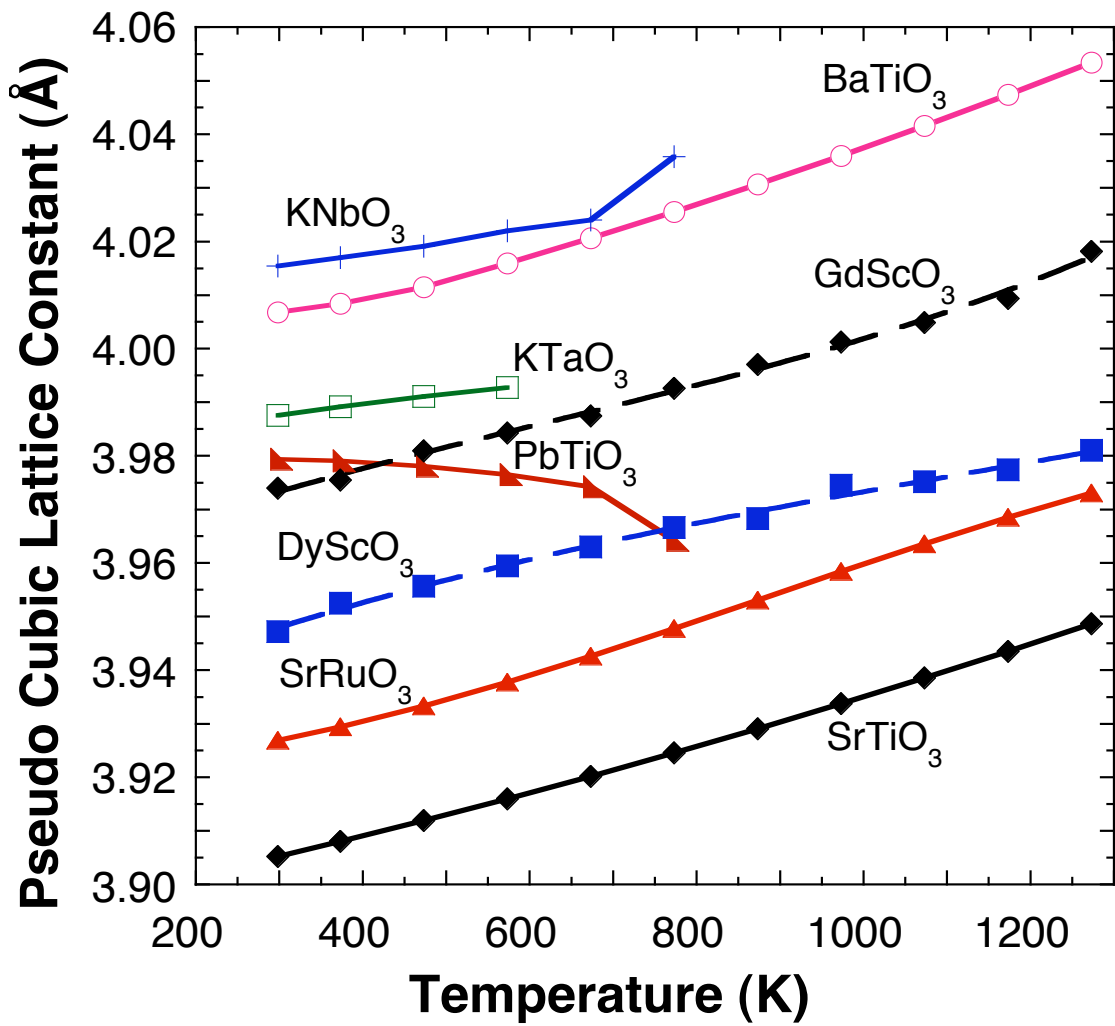
Fig. 4.9 Pseudocubic lattice parameters of oxide perovskites as a function of temperature from Refs. 8,11,15, and 48 (solid lines), and the experimental data for DyScO₃ and GdScO₃ (dashed lines).

4.4.2 Dielectric Measurements

The dielectric constants at room temperature were found to be $\varepsilon_{11} = 19.2$,

$\varepsilon_{22} = 29.5$ and $\varepsilon_{33} = 22.8$ for $GdScO_3$ and $\varepsilon_{11} = 18.8$, $\varepsilon_{22} = 35.5$ and $\varepsilon_{33} = 22.1$ for

$DyScO_3$. The dielectric loss, tan δ, was less than 10^{-4} for all samples measured.

Measurements made on (110) oriented slabs of both these crystals show a dielectric

constant of 21.4 for $GdScO_3$ and 20.5 for $DyScO_3$. The dielectric constant in the [101]

direction is comprised of components of the ε_{11} and ε_{33} tensor values, and serves as a

check of these tensor coefficients. Calculation of the dielectric constant in this direction

based on the measured ε_{11} and ε_{33} values in $GdScO_3$ gives 21.1, in close agreement with

the measured value of 21.4. The calculated value for $DyScO_3$ is 20.5, identical to the

measured value.

The temperature dependence of the dielectric tensor coefficients is shown in Fig.

4.10 for $DyScO_3$ and Fig. 4.11 for $GdScO_3$. The dielectric data shows small changes as a

function of temperature from 4.5 to 470K. The [100] and [001] directions show different

temperature dependence than the [010] direction. The [100] and [001] directions have a

linear region down to 60K for $DyScO_3$ and 100K for $GdScO_3$. Below these thresholds the

dielectric constant is much less dependent on temperature. The temperature coefficient of

capacitance (TCC) for linear regions of $DyScO_3$ were 370 ppm in both the [001] and

[100] directions. For $GdScO_3$ the TCC's were 185ppm (in the [100]) and 210ppm (in the

[001]). In the [010] direction, both materials show a small peak in the dielectric constant

and loss, at 15 and 10K for $DyScO_3$ and $GdScO_3$, respectively. However, the dielectric

constant does not change by more than 2 over this temperature range. The loss data show
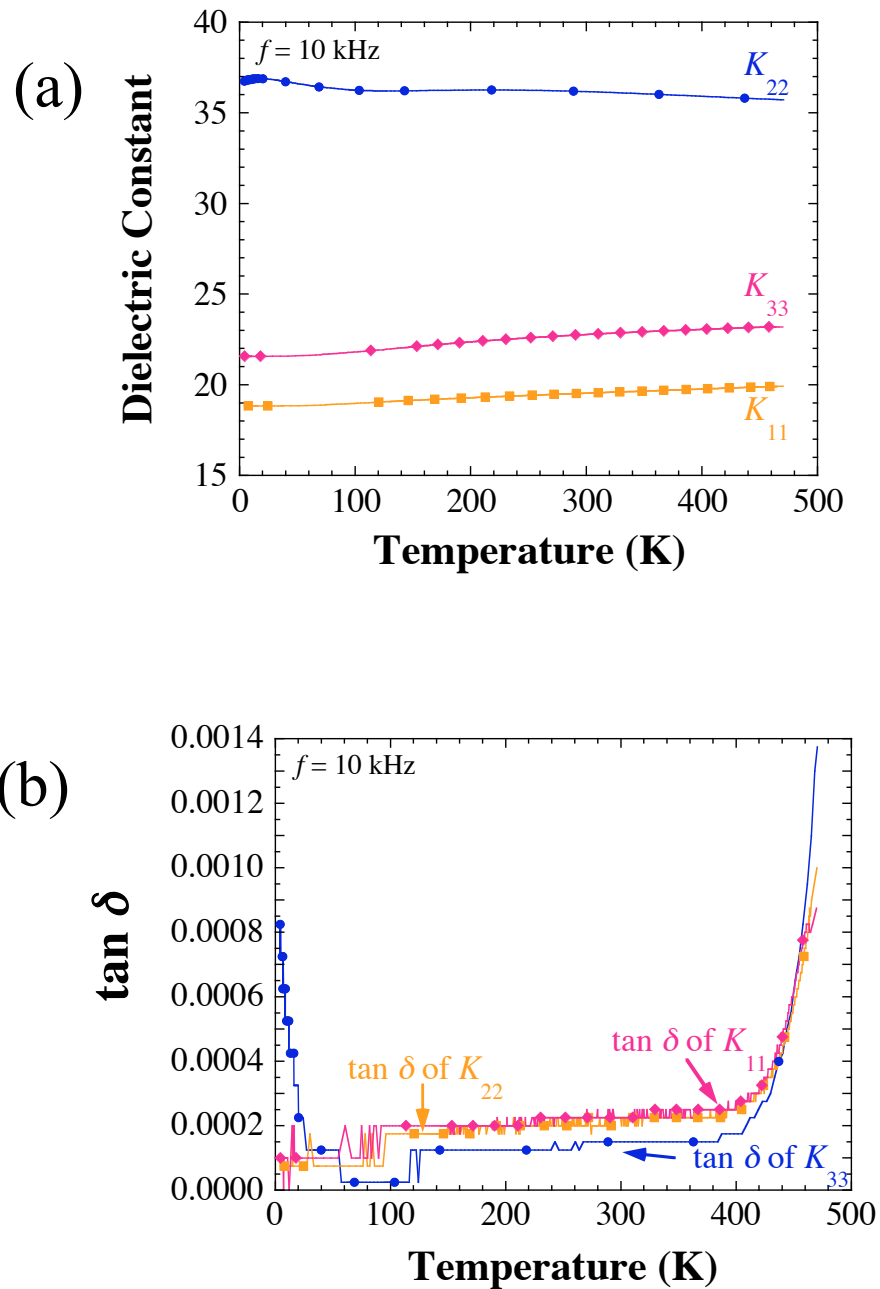
Fig. 4.10 Dielectric permittivity data for DyScO₃ measured along the three principal directions from 4.2 to 470 K (a) dielectric constant and (b) loss. Steps in the loss are associated with instumental resolution.
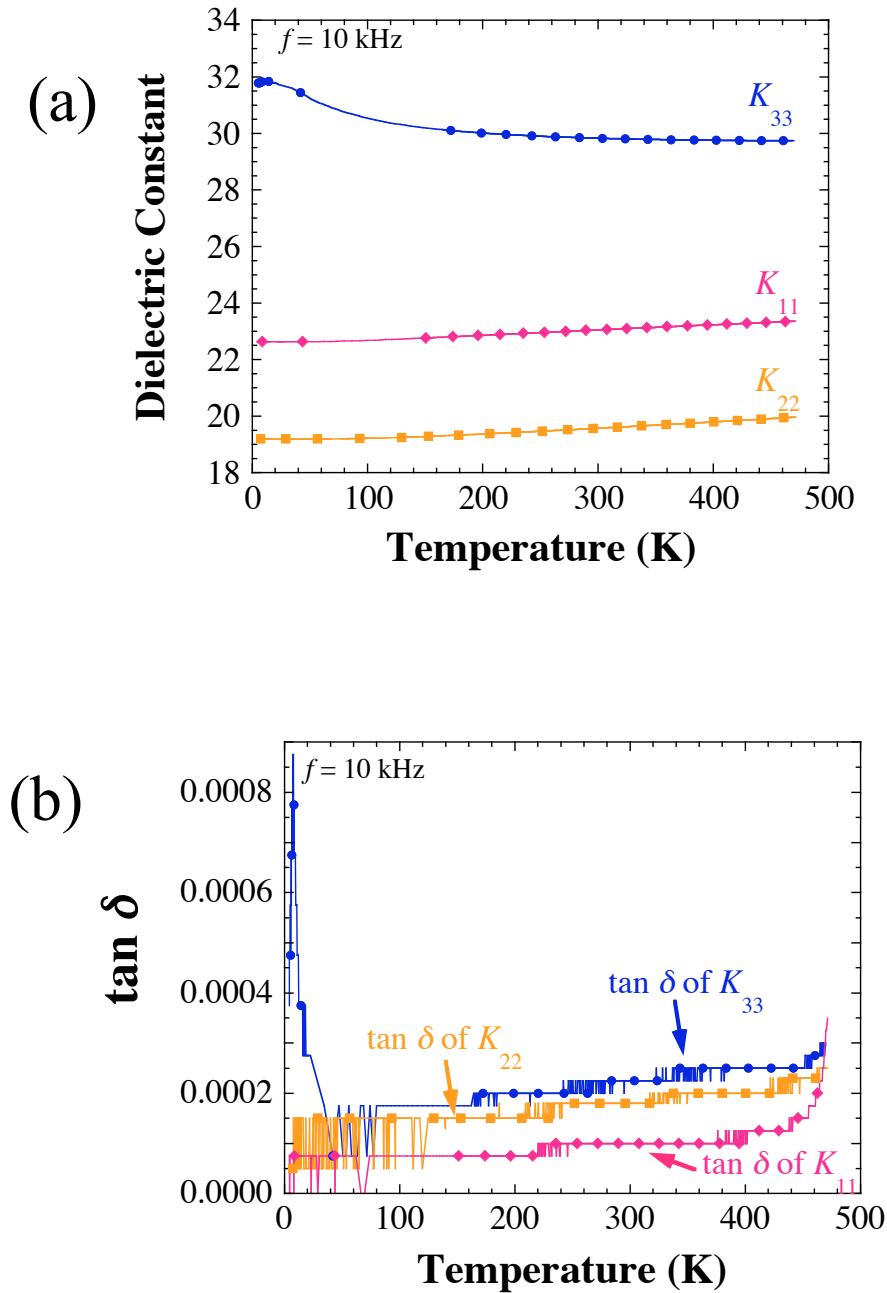
Fig. 4.11 Dielectric permittivity data for GdScO₃ measured along the three principle directions from 4.2 to 470 K (a) dielectric constant (b) loss. Steps in the loss are due to instrumental resolution

similar small temperature dependence with tan δ below 0.001 over the temperature range. It is also important to note that neither of these materials show any frequency dependence of the dielectric data from (100 Hz to 1 MHz). The low TCC, small loss and lack of large dielectric anomalies means that these materials should not interfere with electrical measurements of films grown on their surface.

4.5 Conclusions

The lattice parameters of $DyScO_3$ and $GdScO_3$ were examined as a function of temperature, from 298 to 1273 K, using x-ray diffraction. The data were best fit by the *Pnma* space group and did not show any phase transitions through the temperature range examined. $DyScO_3$ and $GdScO_3$ appear to be far away from a structural phase transition at 1273 K according to the *c/a* ratio. The thermal expansion was found to be anisotropic and this anisotropy was attributed to the rotation of the ScO_6 octahedra. The average thermal expansion coefficients deduced are close to those of other oxide perovskites. The dielectric constants are between 19 and 36, depending on direction, and have very low TCC's. The dielectric properties of these $DyScO_3$ and $GdScO_3$ will not interfere with the properties of thin films on their surface. The dielectric and thermal expansion properties of these materials, as well as the entire family of rare earth scandates, are good substrates for the epitaxial growth of oxide perovskites, particularly for those with pseudo-cubic lattice constants in the 3.93-4.05 Å range covered by the $ReScO_3$ materials.

References.

[1] J. Schubert, O. Trithaveesak, A. Petraru, C. L. Jia, R. Uecker, P. Reiche, and D.G. Schlom, Appl. Phys. Lett. **82**, 3460 (2003).

[2] S.-I. Karimoto and M. Naito, Appl. Phys. Lett. 84, 2136 (2004).

[3] *Landolt-Börnstein: Numerical Data and Functional Relationships in Science and Technology*, edited by K.-H. Hellwege and A. M. Hellwege (Springer-Verlag, Berlin, 1976), New Series, Group III, Vol. 7e, pp. 11-13.

[4] J-M. Badie, High Temp. High Pressures 2, 309 (1970).

[5] S. N. Amanyan, E. V. Antipov, V. A. Antonov, P. A. Arsen'ev, Kh. S. Bagdasarov, A. M. Kevorkov, L. M. Kovba, and A. V. Rakhmatuli, Russ. J. Inorg. Chem. 32, 1225 (1987) [Zh. Neog. Khim. 32, 2087 (1987)].

[6] *International Tables for Crystallography, Vol. A: Space Group Symmetry,* 5th edition*, edited by T. Hahn (Kluwer, Dordrecht, 2002), p. 66.

[7] H. D. Megaw, *Crystal Structures: A Working Approach* (Tech Books, Fairfax, 1973), pp. 174, 298-301, 467-469.

[8] C. B. Eom, R. J. Cava, R. M. Fleming, J. M. Phillips, R. B. van Dover, J. H. Marshall, J. W. P. Hsu, J. J. Krajewski, and W. F. Peck, Jr., Science **258**, 1766 (1992).

[9] *Powder Diffraction File: Sets 27 to 28*, edited by W. F. McClune, M .E. Mrose, B. Post, S. Weissmann, H. F. McMurdie, E. Evans, and W. Wong-Ng (International Centre for Diffraction Data, Swarthmore, 1986), p. 78. Card 27-220.

[10] *Powder Diffraction File: Sets 27 to 28*, edited by W. F. McClune, M. E. Mrose, B. Post, S. Weissmann, H. F. McMurdie, E. Evans, and W. Wong-Ng (International Centre for Diffraction Data, Swarthmore, 1986), p. 72. Card 27-204.

[11] B. C. Chakoumakos, S. E. Nagler, S. T. Misture, and H. M. Christen, Physica B **241**, 358 (1998).

[12] A. M. Glazer, Acta Crystallographica B **28**, 3384 (1972).

[13] A. M. Glazer, Acta Crystallographica A **31**, 756 (1974).

[14] B. B. van Aken, *Structural response to electronic transitions in hexagonal and ortho-manganites*, Ph.D. Thesis, Univ. of Groningen (2001).

[15] D. Taylor, Trans. J. Br. Ceram. Soc. **84**, 181 (1985).

[16] *Landolt-Börnstein: Numerical Data and Functional Relationships in Science and Technology*, edited by O. Madelung, M. Schulz, and H. Weiss (Springer, Berlin, 1982), New Series, Group III, Vol. 7b, p. 22.

[17] H. M. Christen, L. A. Boatner, J. D. Budai, M. F. Chisholm, L. A. Gea, D. P. Norton, C. Gerber, and M. Urbanik, Appl. Phys. Lett. **70**, 2147 (1997).

[18] K. L Ovanesyan, A. G. Petrosyan, G. O. Shirinyan, C. Pedrini, and L. Zhang, Opt. Mater. **10**, 291 (1998).

[19] D. G. Schlom, C. D. Brandle, and A. Ven Graitis (private communication).

[20] J. S. Speck and W. Pompe, J. Appl. Phys. **76**, 466 (1994).

[21] C. M. Foster, W. Pompe, A. C. Daykin, and J. S. Speck, J. Appl. Phys. **79**, 1405 (1996).

[22] A. E. Romanov, W. Pompe, and J. S. Speck, J. Appl. Phys. 79, 4037, (1996).

[23] H. Sato and M. Naito, Physica C **274**, 221(1997).

[24] N. A. Pertsev and A. G. Zembilgotov, J. Appl. Phys. **80**, 6401 (1996).

[25] I. Bozovic, G. Logvenov, I. Belca, B. Narimbetov, and I. Sveklo, Phys. Rev. Lett. **89**, 107001 (2002).

[26] Q. Gan, R.A Rao, C. B. Eom, J. L. Garrett, and M. Lee, Appl. Phys. Lett. **72**, 978 (1998).

[27] K. Abe, N. Yanase, K. Sano, M. Izuha, N. Fukushima, and T. Kawakubo, Integr. Ferroelectr. **21**, 197 (1998).

[28] S. K. Streiffer, J. A. Eastman, D. D. Fong, C. Thompson, A. Munkholm, M. V. Ramana Murty, O. Auciello, G. R. Bai, and G. B. Stephenson, Phys. Rev. Lett. **89**, 067601 (2002).

[29] Y. L. Li, S. Y. Hu, Z. K. Liu, and L. Q. Chen, Appl. Phys. Lett. **78**, 3878 (2001).

[30] Y. L. Li, S. Y. Hu, Z. K. Liu, and L. Q. Chen, Acta Mater. **50**, 395 (2002).

[31] Y. L. Li, S. Choudhury, Z. K. Liu, and L. Q. Chen, Appl. Phys. Lett. **83**, 1608 (2003).

[32] J. H. Haeni, P. Irvin, W. Chang, R. Uecker, P. Reiche, Y. L. Li, S. Choudhury, W. Tian, M. E. Hawley, B. Craigo, A. K. Tagantsev, X. Q. Pan, S. K. Streiffer, L. Q. Chen, S. W. Kirchoefer, J. Levy, and D. G. Schlom, Nature **430**, 758 (2004).

[33] W. D. Nix and B. M. Clemens: Crystallite coalescence, J. Mater. Res. **14**, 3467 (1999).

[34] J. H. Haeni, J. Lettieri, M. Biegalski, S. Trolier-McKinstry, D. G. Schlom, S.-G. Lim, T. N. Jackson, M. M. Rosario, J. L. Freeouf, R. Uecker, P. Reiche, A. Ven Graitis, C. D. Brandle, and G. Lucovsky (unpublished).

[35] *Landolt-Börnstein: Numerical Data and Functional Relationships in Science and Technology*, edited by O. Madelung, M. Schulz, and H. Weiss (Springer, Berlin, 1982), New Series, Group III, Vol. 7b, p. 26.

[36] *Thermophysical Properties of Matter Vol. 13: Thermal Expansion of Nonmetallic Solids*, edited by Y. S. Touloukian, R. K. Kirby, R. E. Taylor, and T. Y .R. Lee (Plenum, New York, 1977), p. 288.

[37] R. J. Hill and I. Jackson, Phys. Chem. Miner. **17**, 89 (1990).

[38] A. M. Glazer, Acta Crystallogr. Sect. B **28**, 3392 (1972).

[39] H. D. Megaw, Mater. Res. Bull. **6**, 1007 (1971).

[40] Y. Zhao and D. J. Weidner, Phys. Chem. Miner. **18**, 294 (1991).

[41] M. Sasaura, S. Miyazawa, and M. Mukaida, J. Appl. Phys. **68**, 3643 (1990).

[42] K. L. Ovanesyan, A. G. Petrosyan, G. O. Shirinyan, C. Pedrini, and L. Zhang, J. Cryst. Growth **198/199**, 497 (1999).

[43] R. M. Hazen and L. W. Finger, *Comparative Crystal Chemesitry* (Wiley, New York, 1982), pp. 115-164.

[44] X. Liu, Y. Wang, and R. C. Liebermann, Geophys. Res. Lett. **15**, 1231 (1988).

[45] T. Yamanaka, R.C. Liebermann, and C. T. Prewitt, J. Mineral. Petro. Sci. **95**, 182 (2000).

[46] R. D. Shannon and C. T. Prewitt, Acta Cryst. **B25**, 925 1969.

[47] R. D. Shannon, Acta Cryst. A**32**, 751 1976.

[48] J. L Henry and G. G. Thompson, Ceram. Bull. **55**, 281 (1976).

Chapter 5

Relaxor Ferroelectricity in Strained Epitaxial SrTiO$_3$

Thin Films on Rare Earth Substrates[§]

5.1 Abstract

The ferroelectric properties of strained, epitaxial SrTiO$_3$ films grown on DyScO$_3$ and GdScO$_3$ substrates by reactive molecular beam epitaxy are reported. Despite the near 1 % biaxial-tensile strain, the x-ray rocking curve full widths at half maximum in ω are as narrow as 7.2 arc sec (0.002°). The films show a frequency-dependent permittivity maximum near 250 K that is well fit by the Vogel-Fulcher equation. A clear polarization hysteresis is observed below the permittivity maximum, with an in-plane remanent polarization of 10 μC/cm^2 at 77 K. The high T_{max} is consistent with the biaxial tensile strain state, while the superimposed relaxor behavior is likely due to Sc diffusion from the substrate.

5.2 Introduction

Pure bulk $SrTiO_3$ is an incipient ferroelectric that approaches, but does not experience a ferroelectric phase transition as temperature is lowered towards 0 K. Single crystals and bulk ceramics show Curie-Weiss behavior of the dielectric permittivity with a maximum near 4 K.[1] In single crystals, the permittivity increases from about 300 at room temperature to near 24000 at 4 K and remains high down to lower temperatures.[2] This, coupled with the failure to develop clear polarization-electric field hysteresis loops, has led to $SrTiO_3$ being labeled an incipient ferroelectric. It has been suggested that the ferroelectric transition is suppressed due to quantum fluctuations of the Ti ions,[1] making $SrTiO_3$ a quantum paraelectric. The localized nature of the quantum fluctuations has been shown through confocal scanning optical microscopy, where on a local scale $SrTiO_3$ can exhibit ferroelectric behavior.[3] Yamanaka et al.[4] have shown the antiferrodistortive transition at 105 K (from cubic to tetragonal) is partially responsible for the suppression of the ferroelectric transitions through the interaction between the structural order parameter and the polarization.

The quantum paraelectric state is very sensitive to small perturbations that can cause the material to become ferroelectric. Ferroelectricity can be induced by small levels of impurities (e.g Ca, Bi),[5-8] applied electric fields (here the polar state is not stable at zero field),[9-12] ^{18}O substitution,[13] and mechanical stress.[14,15] Thermodynamic analysis predicts that biaxial strain can force $SrTiO_3$ films to become ferroelectric.[16,17] The ability to tailor the strain state of coherent epitaxial thin films via lattice match allows these predictions to be checked experimentally.

We examined $SrTiO_3$ films on (101) $DyScO_3$ substrates. $DyScO_3$ is a distorted perovskite with a pseudo cubic lattice constant of 3.948 Å at room temperature. This material has been shown to be orthorhombic with a low dielectric constant, a thermal expansion comparable to $SrTiO_3$, no phase transitions from 25-1273 K, and no dielectric anomaly from 100-423 K.[18,19] $DyScO_3$ offers the unique opportunity to grow high quality, commensurate $SrTiO_3$ films under tensile strain.[19]

5.3 Experimental Procedure

$SrTiO_3$ films were grown by reactive molecular beam epitaxy (MBE) using a shuttered growth technique on (101) $DyScO_3$ substrates. These films were grown at 650 °C with an ozone background pressure of 3×10^{-6} Torr. The $SrTiO_3$ stoichiometry was calibrated using reflection high-energy electron diffraction oscillations.[20] After growth the films were annealed in air at 700 °C for 1 h to fully oxidize them. The orientation and epitaxy of the films were then examined using a Phillips X'Pert MRD diffractometer.

The dielectric properties were examined with Au/Cr interdigitated electrodes between 100 and 425 K from 500 Hz to 1 MHz using a HP 4284a high precision LCR meter with a Delta Design 9000 oven. The in-plane dielectric constant ($K_{in-plane}$) was calculated using a partial capacitance approach with three different models.[21-23] The only model strictly valid for our interdigitated electrode geometry is the model of Gevorgian *et al.*[23] Due to the much higher permittivity of the film than the substrate, all three models yielded similar results ($K_{in-plane}$

varied by ±111). The measured dielectric loss was ascribed to the film, since the substrate tan δ was typically <0.002, and weakly frequency dependent. Hysteresis loops were then measured on an Aixacct TF2000 analysis tool with a maximum field of 330 kV/cm.

Ceramic materials were also made to determine the effect of Sc on the ferroelectric transition. These ceramic pellets were made using a standard mixed oxide route from $SrCO_3$, TiO_2 and Sc_2O_3 fine grain powders. These powders were mixed with varying amounts of Sc_2O_3 such that the stoichiometry was $Sr(Ti_{1-x}Sc_x)O_3$ with x ranging from 0.0002 to 0.01. These powders were then ball milled for 24 h using 0.125" alumina balls in ethanol. The powders were dried and calcined at 800 °C for 4 h. The $Sr(Ti_{1-x}Sc_x)O_3$ powder was then pressed into 0.5" pellets ~2 mm thick under 200 MPa. These pressed pellets were sintered at 1250 °C for 20 h. After sintering the density of the pellets were found to be ~92 % dense by Archimedes method. The pellets surfaces were then polished to removed any impurities and create smooth parallel surfaces. The chrome-gold electrodes were evaporated onto the samples and then annealed at ~400 °C for 5 h.

5.4 Results and Discussion

5.4.1 Film Epitaxy

X-ray diffraction was performed to check the orientation and epitaxy of the film. The out-of-plane lattice constant was determined to be 3.8833±0.0005 Å (Fig. 5.1(a)). The rocking curve full width at half maximum (FWHM) of the $SrTiO_3$

200 peak was ~7 arc sec in ω, identical to the underlying DyScO$_3$ substrate and

the resolution of the diffractometer (Fig. 5.1(b)). This compares favorably to the

narrowest rocking curves reported for films of SrTiO$_3$ (540 arc sec)[12] or

(Ba,Sr)TiO$_3$ (72 arc sec)[24] and is about an order of magnitude narrower than

SrTiO$_3$ single crystals.[24-26] Off-axis scans confirmed cube-on-cube epitaxy and an

average in-plane lattice constant of 3.946±0.003 Å for all the films, indicating that

the SrTiO$_3$ film is coherent with the substrate within the resolution of this

measurement. This corresponds to a biaxial tensile strain in the film of

approximately 1%. According to thermodynamic analysis the ferroelectric

transition should occur near 220 K for a specific choice of Landau and property

coefficients from SrTiO$_3$ single crystals;[16] if the range of relevant coefficients

reported for SrTiO$_3$ single crystals are used in the thermodynamic analysis, the

ferroelectric transition is predicted to occur at 300±100 K for this strain state.[17,27]

5.4.2 Dielectric Properties

The dielectric data is shown in Fig. 5.2 and shows two interesting features,

a large peak in the dielectric constant and frequency dispersion. The peak

permittivity near 20,000 at 250 K, is much higher than any previously reported for

SrTiO$_3$ films,[12,15,28-30] and close to the values of unstrained SrTiO$_3$ single crystals

at 4 K.[1,2] The temperature of the permittivity, maximum (T_{max}) is ~250 K and

frequency dependent. This value is in reasonable agreement with the transition

temperature predicted by thermodynamic analysis,[16,17] and ~100 K
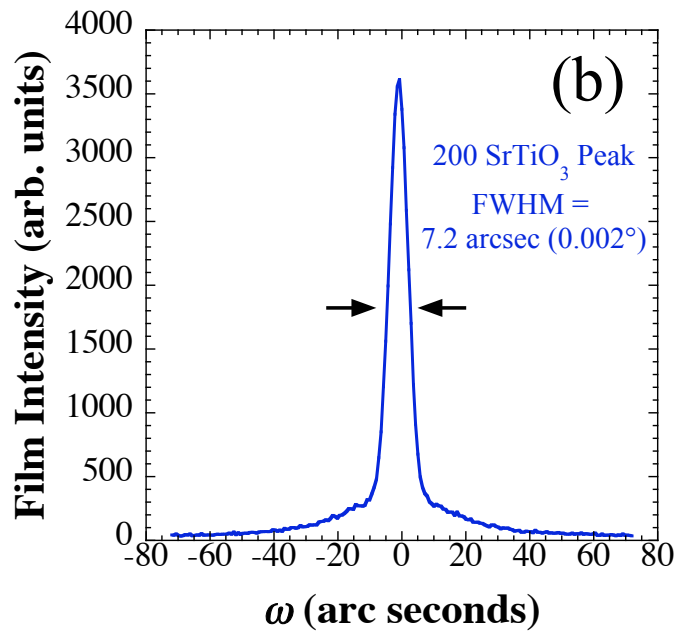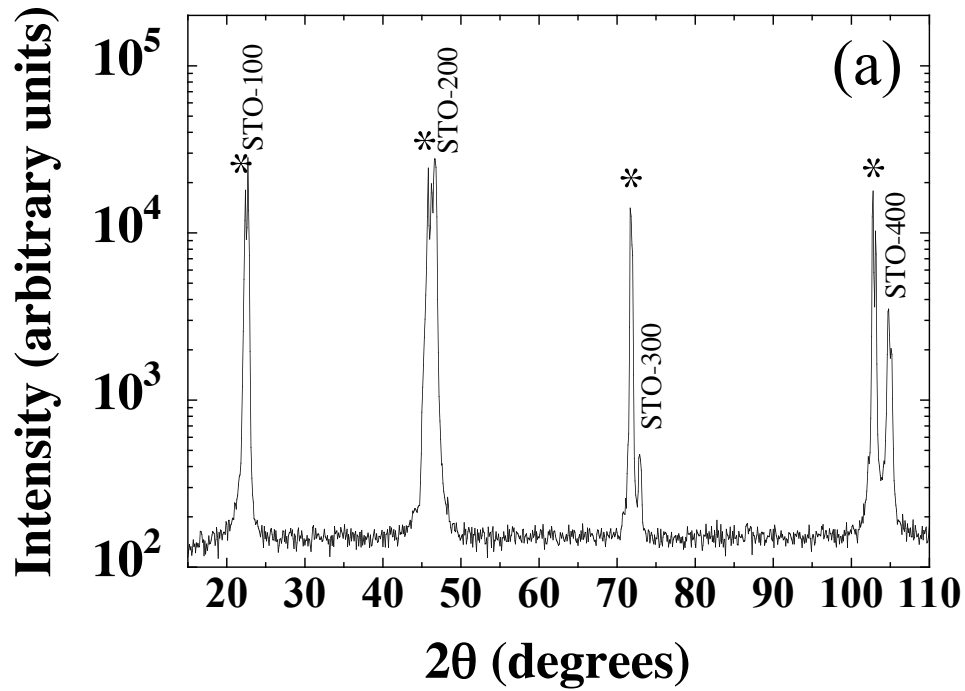
Fig. 5.1(a) θ-2θ scan of 500 Å thick SrTiO₃ on (101) DyScO₃ showing good epitaxy of the film to the substrate. The substrate peaks are denoted with *. (b) *ω*-scan of the SrTiO₃ 200 peak showing good crystallinity with a FWHM of 7.2 arcsec.
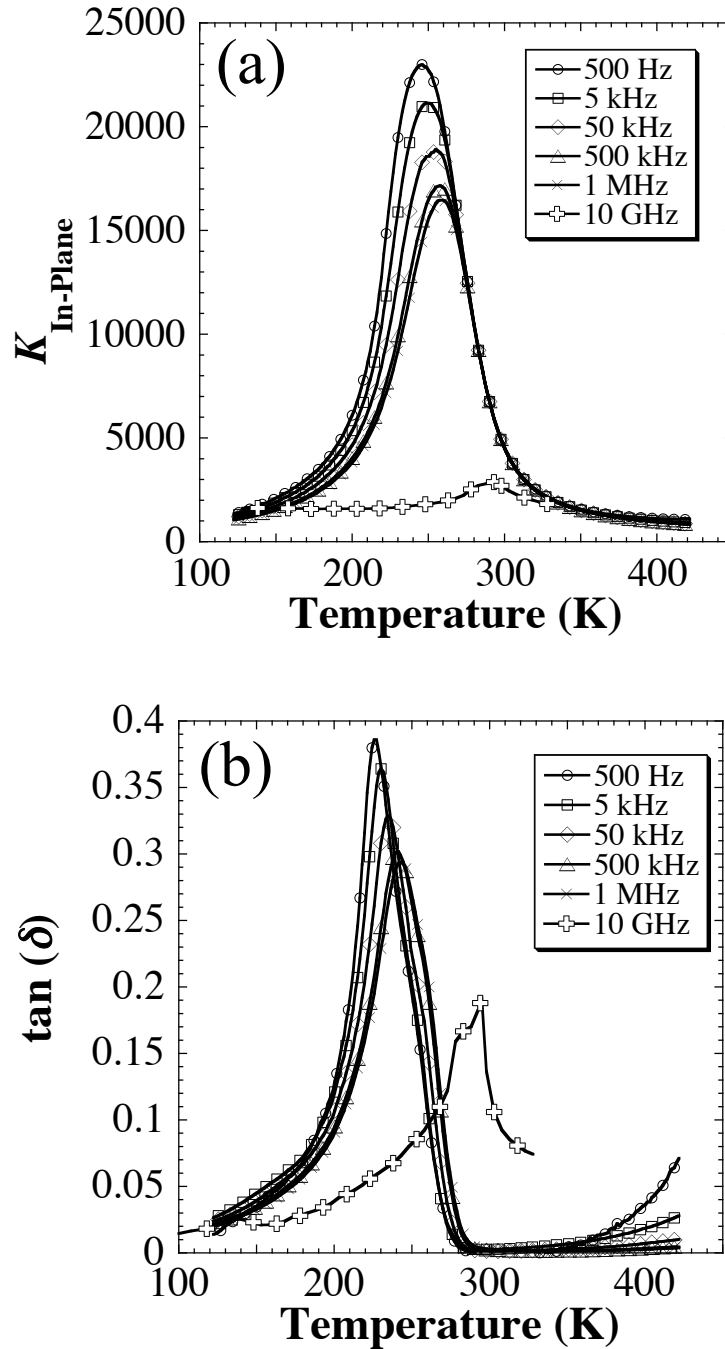
Fig. 5.2 (a) In-plane dielectric constant ($K_{\text{In-Plane}}$) and (b) tan δ as a function of

temperature of a 500 Å thick strained SrTiO$_3$/DyScO$_3$ film. The 10 GHz data from

Ref. 17 of a strained SrTiO$_3$/DyScO$_3$ film grown under similar conditions is included in

the plots.

103
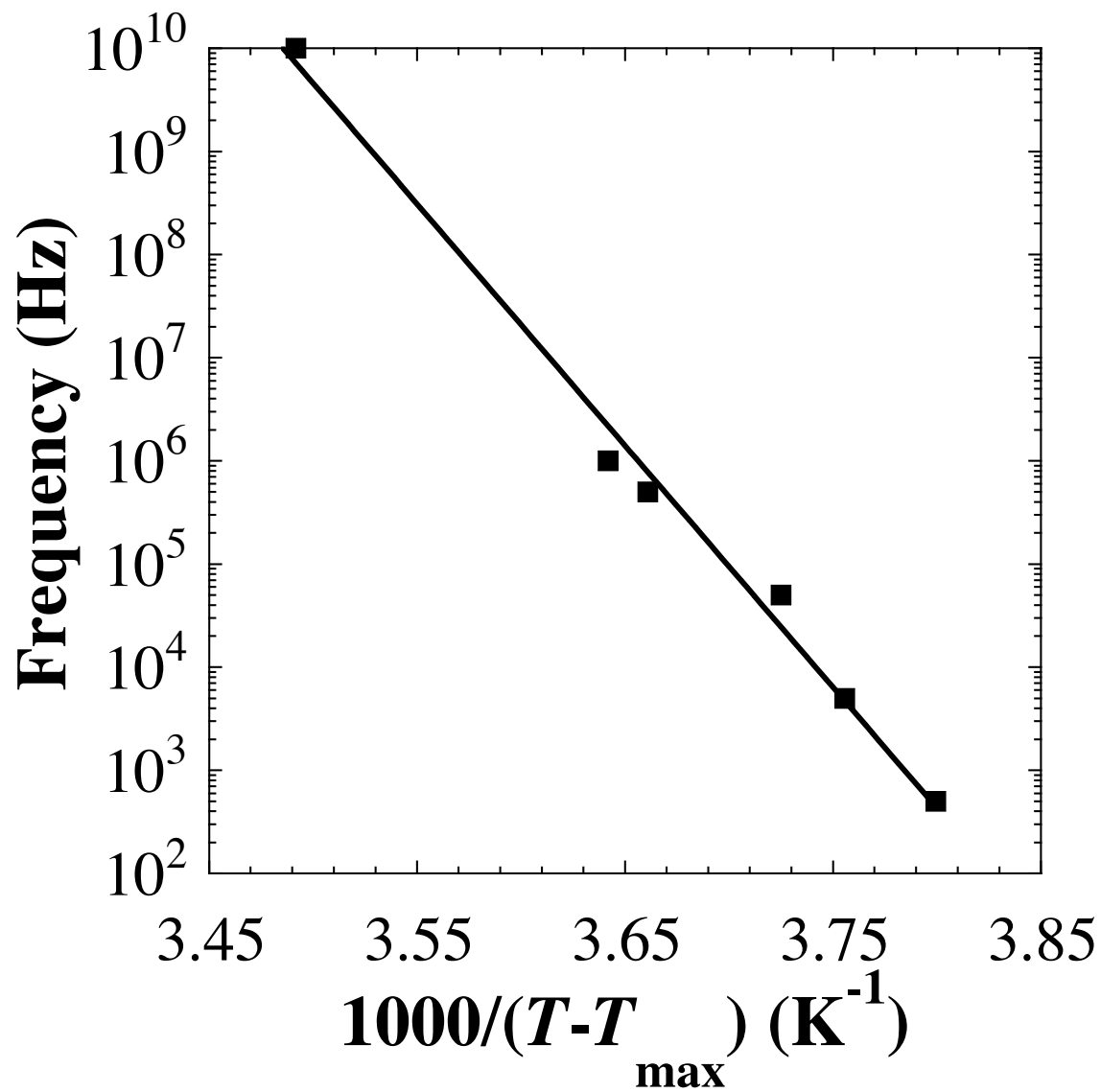
Fig. 5.3 Vogel-Fulcher fit to the tan δ data in Fig. 5.2(b) with a very good fit from 500 Hz to 10 GHz.

above the highest transition temperature previously reported for $SrTiO_3$ films.[12,15,30,31]

The frequency dispersion in the dielectric constant suggests relaxor behavior. The convergence of the permittivity data above T_{max} demonstrates that the dispersion is not an artifact associated with space charge polarizability. The frequency dependence of the maximum in the loss tangent could not be fit to an Arrhenius equation. Instead, as is characteristic of many relaxor ferroelectrics,[32] the data were well fit (over 7 orders of magnitude in frequency with an R^2 value of 0.996, see Fig. 5.3) by the Vogel-Fulcher equation:[33,34]

$$f(\text{Hz}) = (1.0 \pm 0.36) \times 10^{13} \exp\left[\frac{-50 \pm 3\text{meV}}{k_B(T_{max} - 204 \pm 2\text{K})}\right] \qquad \text{Eq. 5.1}$$

where f is the frequency of the loss tangent maximum and k_B is Boltzmann's constant. The freezing temperature and activation energy are physically reasonable and consistent with observations of other relaxor ferroelectrics.[35] It should be noted that the temperature and frequency dependence of $\tan \delta$ differ somewhat from typical observations on $PbMg_{1/3}Nb_{2/3}O_3$.[35] In particular, the maximum in $\tan \delta$ decreases, rather than increases, with increasing measurement frequency. The data are, however, consistent with the observations of Kleemann *et al.*[40] for Ca-doped $SrTiO_3$.

To check whether the films are ferroelectric, polarization-electric field hysteresis loops were measured using an Aixacct TF2000 analysis tool with a maximum applied field of 330 kV/cm. At room temperature, non-linear dielectric behavior was observed, but when measured at 77 K a hysteresis loop develops with a large remanent polarization (P_r) of 10 μC/cm^2 (Fig. 5.4). The appearance of a hysteresis loop confirms that this
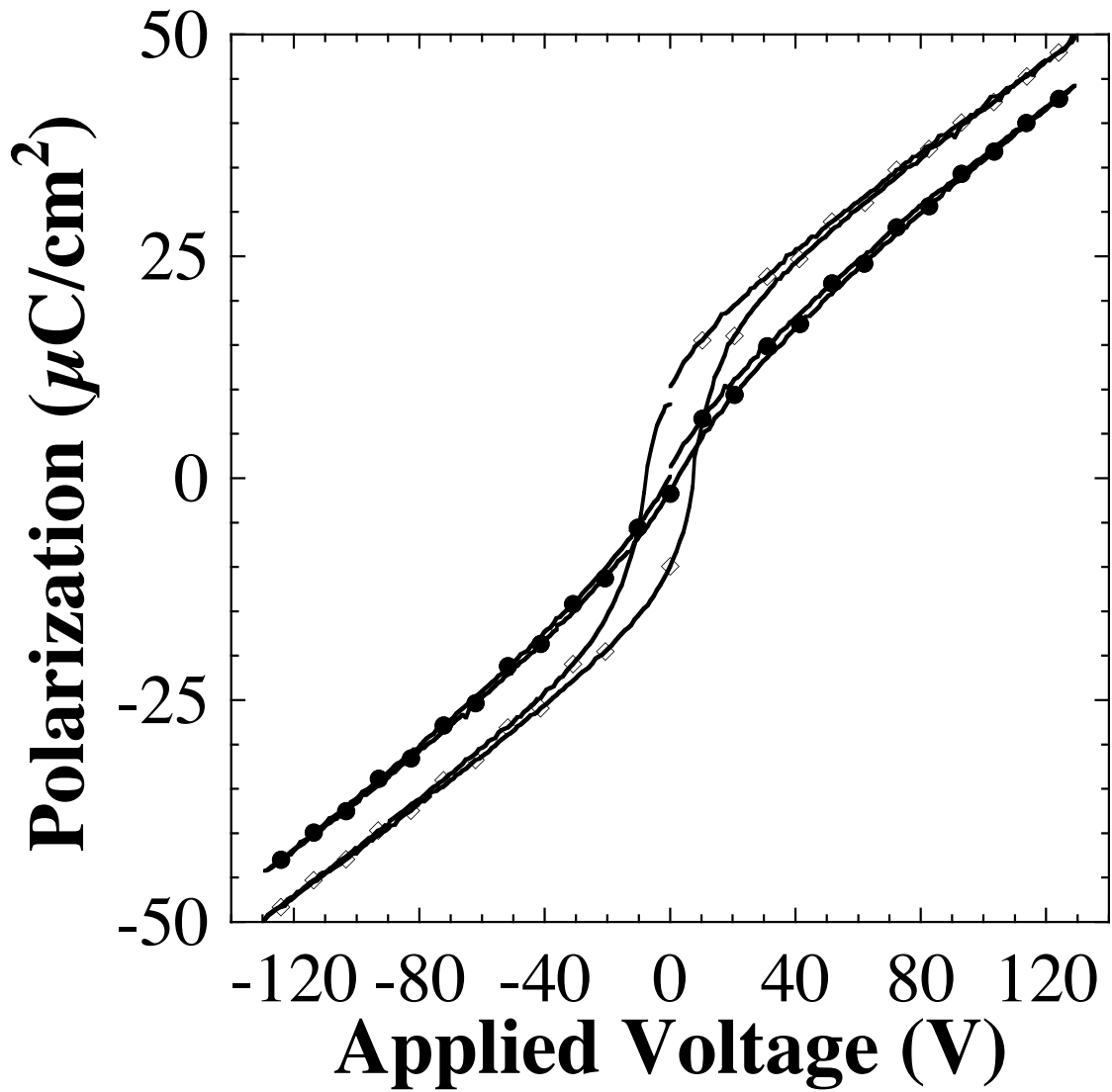
Fig. 5.4 Hysteresis loops measured at room temperature (●) and in liquid nitrogen at 77 K (◊) on the same film as Fig. 5.1. The large slope is due to uncorrected parasitic capacitance.

system is indeed ferroelectric. Fig. 5.5 shows that the dielectric behavior of the film changes smoothly from a non-linear dielectric to a hysteretic one as the temperature is lowered through T_{max}. As expected for a relaxor ferroelectric, polarization hysteresis develops as temperature is lowered through the T_{max}. This confirms the film is a relaxor ferroelectric: a reorientable hysteretic polarization is developed under a sufficiently large applied electric field. The transition temperature to the polar state in Fig. 5.5 is somewhat higher than from the permittivity measurements below. This is probably due to the high electric fields used.

The relaxor behavior was also probed using field cooling studies. The sample was cooled with a dc bias of ~10 kV/cm and then the permittivity was measured during heating. As can be seen in Fig. 5.6, the field cooling induces a much more normal ferroelectric transition. The frequency dependence in the dielectric constant is almost completely removed. This is even more apparent in the loss data where the transition goes from a broad peak into a sharp peak (Fig. 5.6(b)). Thus the films are clearly relaxor ferroelectrics.

In these $SrTiO_3$ films, the ferroelectricity at high temperatures stems from the biaxial strain.[16,17] The relaxor behavior is, however, unexpected. Several possible origins of the dielectric relaxation were considered: surface ferroelectricity in the substrate, a small structural coherence length in the film, inhomogeneous strain,[36] and point defects.[5,8,9]

Bulk $DyScO_3$ does not show any phase transitions over the temperature range utilized here. Nonetheless, a surface ferroic transition is possible. Thus, the surface
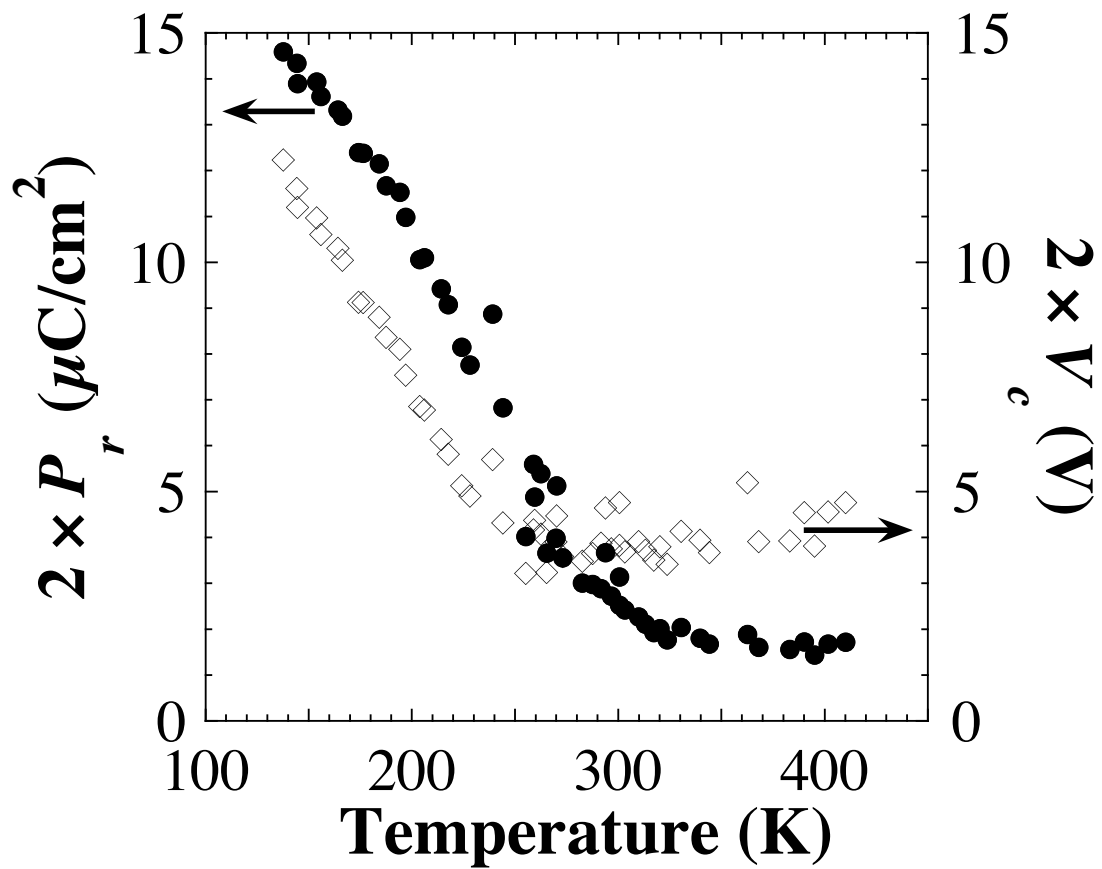
Fig. 5.5 Remanent polarization ($\bullet$) and coercive voltage ($\Diamond$) measured as a function of

temperature on the same film as Fig. 5.1. ($2 \times P_r = P_r(+) + |P_r(-)|$ and

$2 \times V_c = V_c(+) + |V_c(-)|$).
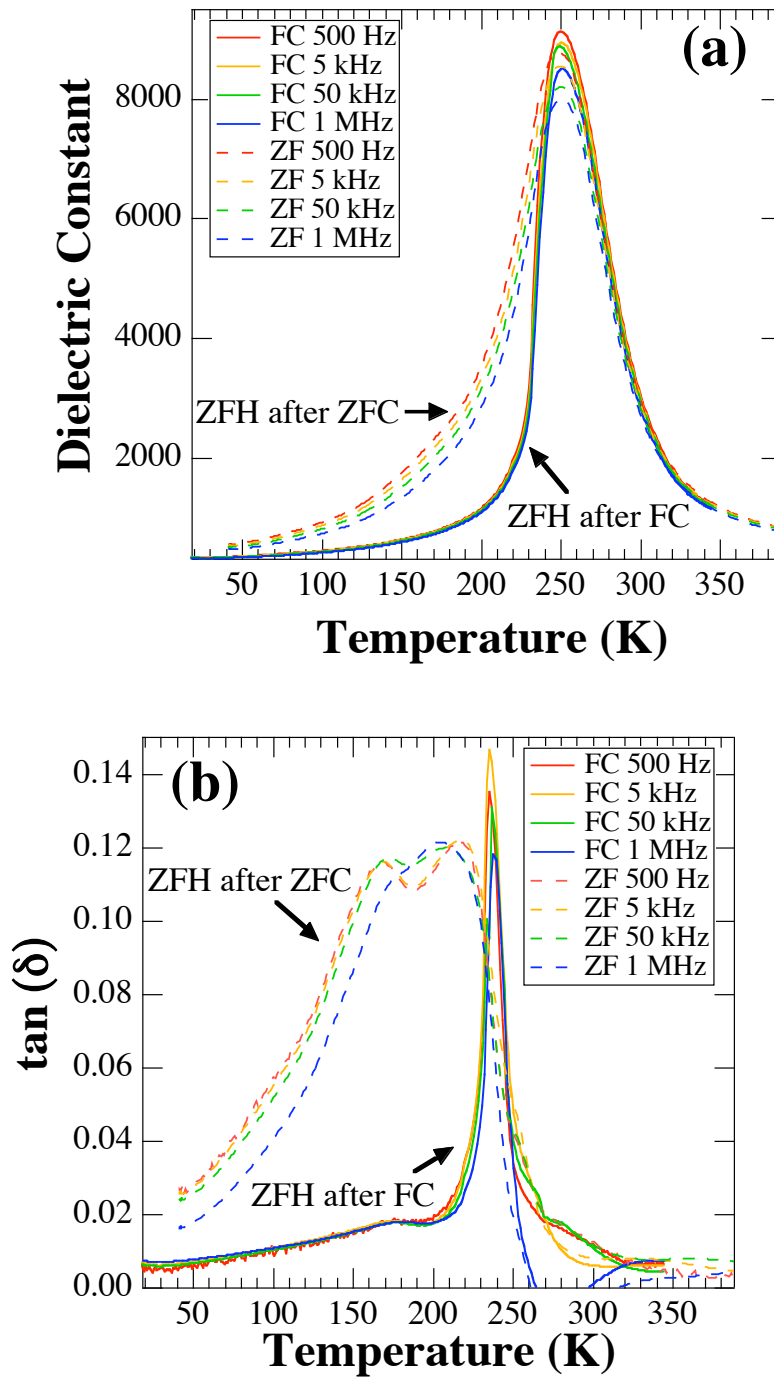
Fig. 5.6 Dielectric permittivity measurement of the (a) dielectric constant and (b) loss for

a 500 Å thick SrTiO₃ grown on DyScO₃ measured on heating without field cooling (ZFH

after ZFC) and after field cooling (ZFH after FC).

dielectric properties of the bare substrate were examined using interdigitated electrodes. No relaxation, phase transitions, or ferroelectric transitions in the substrate were detected over the 100-450 K range, suggesting that the observed behavior is not governed by a surface ferroic transition in the substrate.

While small structural coherence lengths can induce relaxor characteristics in ferroelectric films,[36] the crystalline quality of these films (with rocking curves far narrower than $SrTiO_3$ single crystals[24-26]) suggests that this cannot be responsible for the relaxation. Similarly, partial relaxation in the film could produce an inhomogeneous film strain state, inducing random local fields and relaxor behavior.[37] Again, however, the structural perfection of the current samples argues against this as the dominant mechanism. Dielectric measurements of a 250 Å thick film as a function of temperature (which is far below the critical thickness for the onset of structural relaxation[38]) reveal there is still frequency dispersion of the dielectric data (Fig. 5.7). This indicates that the relaxor behavior is not due to the inhomogeneous strain in the films since it is present for fully coherent films that do not have any inhomogeneous strain.

Point defects, including impurity-oxygen vacancy clusters or anti-site defects, cannot be ignored as a source for the relaxor behavior.[39,40] These point defects could arise from errors in composition control, i.e., the Sr:Ti ratio deviating from precisely 1:1. Unintentional doping from the substrate could also be a source of the point defects. In previous work, $SrTiO_3$ doped with Ca or Bi has been shown to exhibit dielectric relaxation at low doping levels and relaxor ferroelectric behavior at higher doping levels.[5-8] Typical observations include large permittivities, on the order of 10^3-10^5,[5-8]
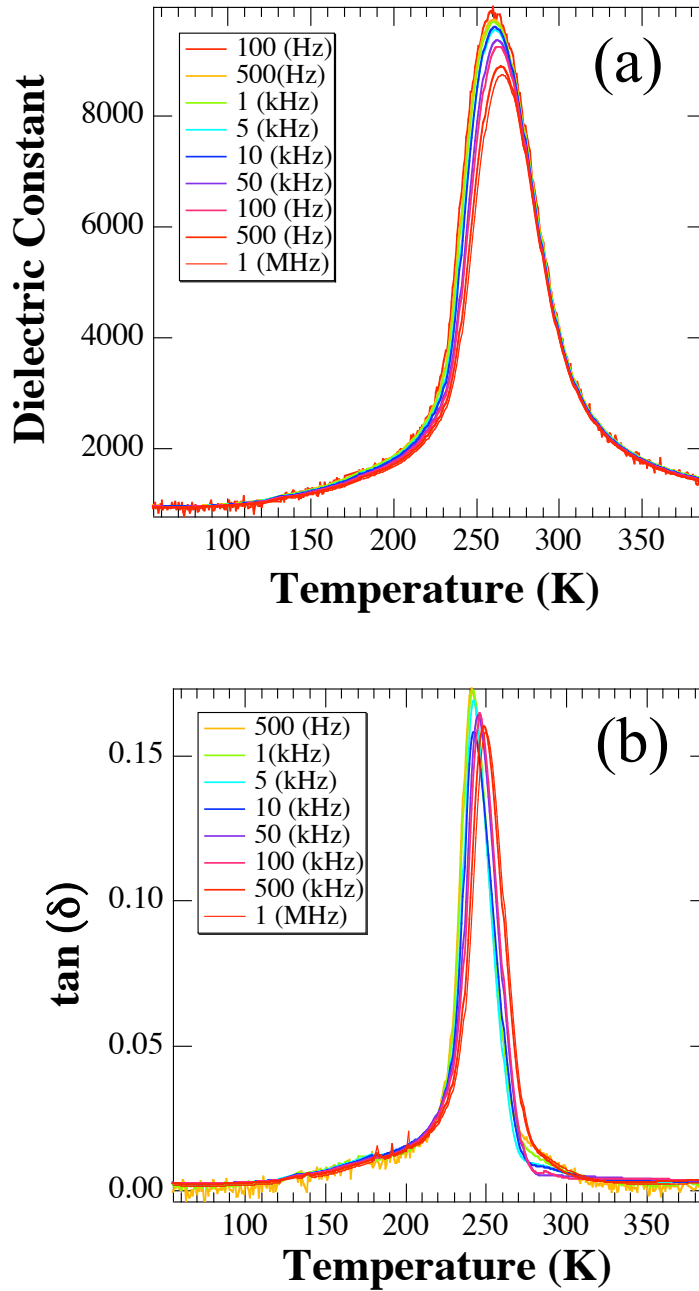
Fig. 5.7 Dielectric permittivity for a 250 Å thick SrTiO$_3$ film grown on DyScO$_3$ showing frequency dispersion of the permittivity. Since 250 Å is far below the critical thickness of the SrTiO$_3$ /(101) DyScO$_3$ system and the film is fully coherent to the substrate, this indicates that inhomogeneous strain is not the source of the relaxor behavior.

dispersion of the low frequency permittivity,[6,8] polarization hysteresis,[5,8] and

permittivity maxima ranging from about 10 to 200 K.[5,6,8]

The films in this investigation are not intentionally doped, however, the samples are held

at 650 °C for hours during growth. This could allow diffusion from the substrate into the

film. Secondary ion mass spectrometry (SIMS) data show that Sc and Dy are present in

the film (Fig. 5.8(a)). It is possible that $Sc^{\bullet}_{Ti}$, defect dipoles involving thedopant, or

defect dipoles from site disorder introduce random local electric fields into the

ferroelectric and highly polarizable strained $SrTiO_3$ matrix, resulting in relaxor

ferroelectricity. There are, however, no reports of relaxor ferroelectric behavior in Sc-

doped $SrTiO_3$;[41] our own measurements on Sc-doped bulk (unstrained) $SrTiO_3$ are also

devoid of relaxor ferroelectric behavior.

SIMS of two $SrTiO_3$ films grown on $DyScO_3$ are shown Fig. 5.8. The 500 Å (Fig.

5.8(a)) thick film has much more Sc than the 800 Å thick film (Fig. 5.8(b)). By

comparing the dielectric permittivity behavior of the 500 Å thick film (Fig. 5.2) to that of

the 800 Å thick film (Fig. 5.9) it can be seen that the higher scandium content is linked to

more pronounced relaxor character. This indicates that the relaxor behavior is correlated

to the scandium diffusion from the substrate into the film. It is unknown if other point

defects also contribute.

To explore the effects of scandium without a superimposed strain, the dielectric

constant of scandium doped $SrTiO_3$ ceramics was measured as a function of temperature.

Fig. 5.10(a) shows no frequency dispersion over the frequency range 100 Hz to 1 MHz.

However, it can be seen that the dielectric constant initially increases as a function of

scandium content until the scandium is no longer being incorporated into the $SrTiO_3$
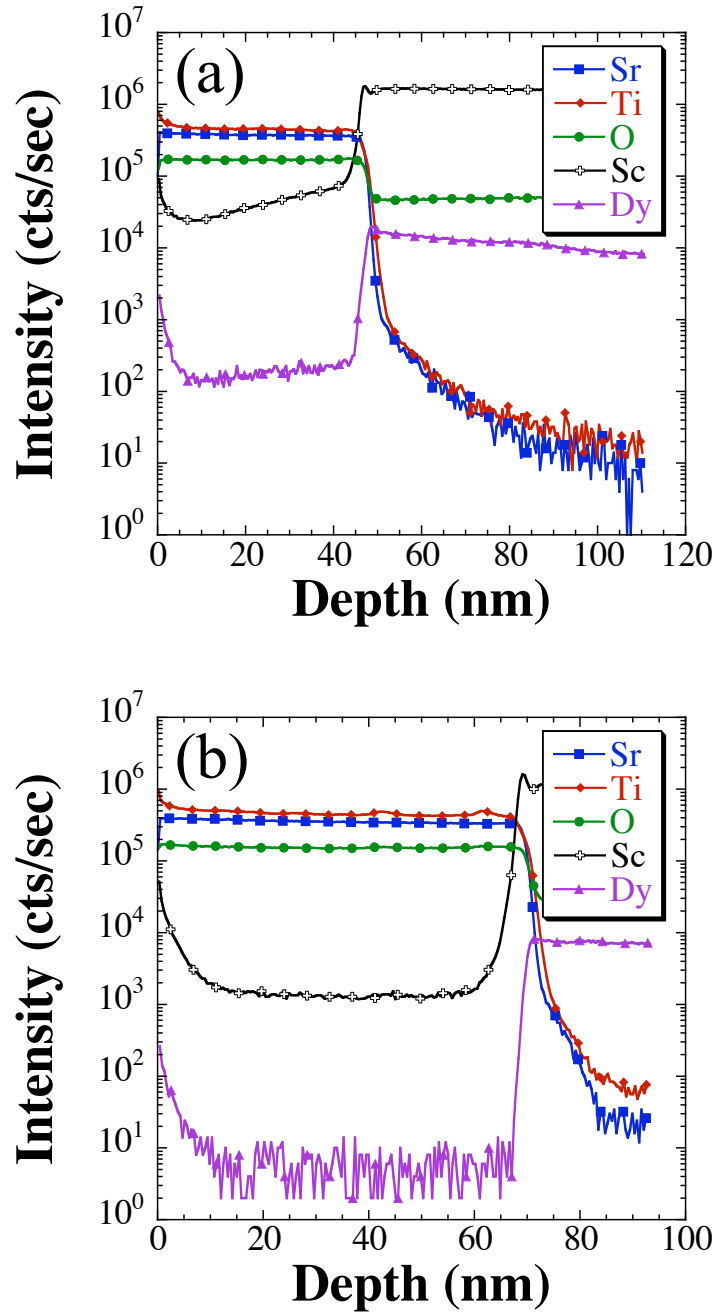
Fig. 5.8 SIMS analysis showing diffusion of Sc and Dy from the substrate into the film

for (a) the 500 Å thick film of Fig. 5.1-Fig. 5.3, and (b) an 800 Å thick SrTiO₃ film.

Dielectric data for the latter film are given in Fig. 5.9
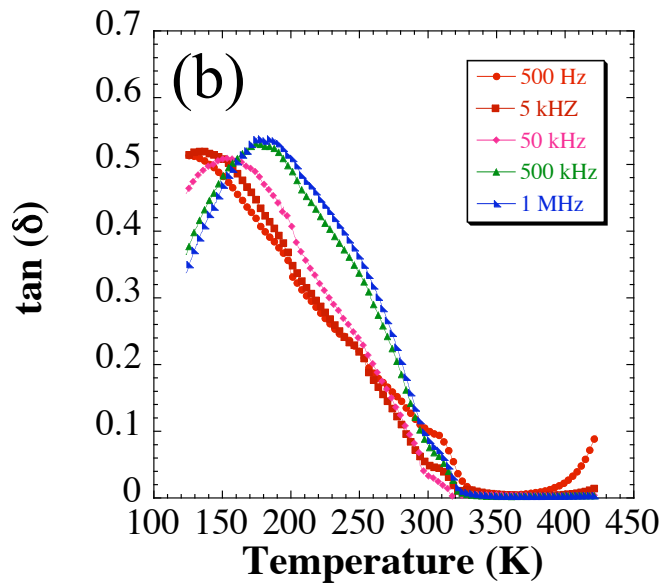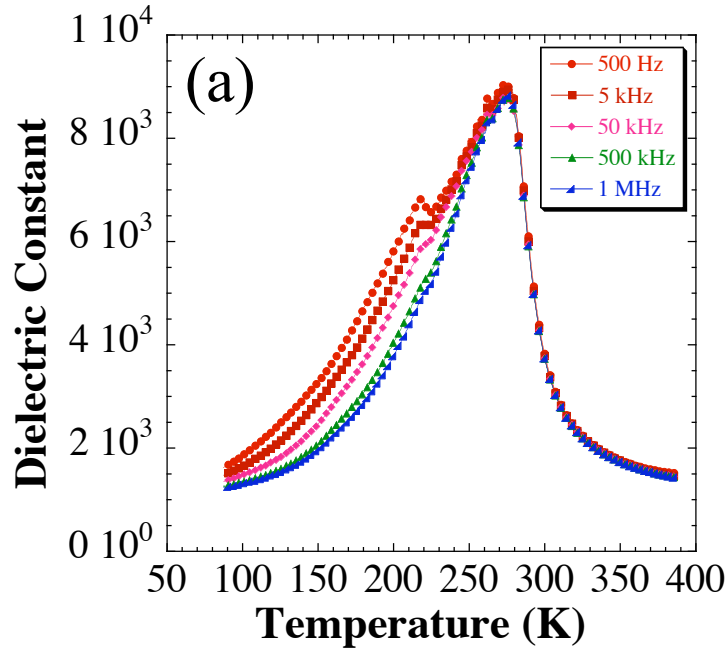
Fig. 5.9 (a) In-plane dielectric constant and (b) tan δ as a function of temperature of a 800 Å thick strained $SrTiO_3/DyScO_3$ film. Less frequency dispersion of the permittivity was observed compared to the 500 Å thick film in Fig. 5.2.
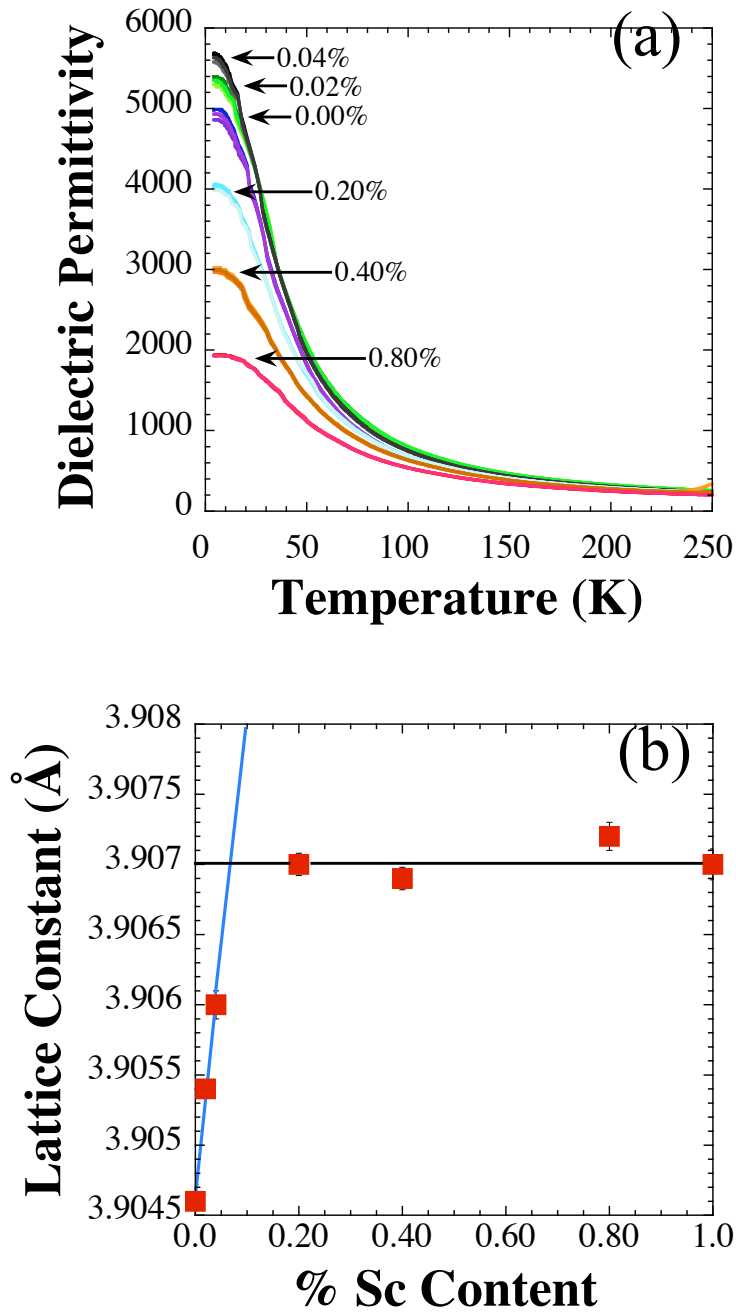
Fig. 5.10 (a) Dielectric constant and (b) lattice constants of Sc doped SrTiO$_3$ ceramics

pellets. (a) The dielectric constant as a function of temperature measured from 100 Hz to

1MHz for each sample. (b) Room temperature lattice constant showing the scandium

solubility limit is approximately 0.06% Sc.

lattice as illustrated by Fig. 5.9(b). Thus the decrease in the dielectric constant after 0.04% scandium is attributed to precipitation of scandium oxide to the grain boundaries. This resulting mixture of low permittivity Sc_2O_3 and high permittivity $SrTiO_3$ dramatically lowering the dielectric constant.[42] Below the solubility limit, however, doping raised the permittivity. This is consistent with reports on Bi and Ca doped $SrTiO_3$ (see Fig. 2.11) where the dopant first increases the permittivity then induces relaxor ferroelectricity at higher doping levels.[5-8] Thus, low levels of scandium, ~0.04 %, appear to introduce random fields which would favor relaxor ferroelectricity. However, since higher levels of scandium incorporation were not achievable in the unstrained ceramics, due to scandium was precipitation of scandium to the grain boundaries, no ferroelectric transition was observed.

To examine the effects of strain further, a 250 Å thick film of $SrTiO_3$ was grown on $GdScO_3$. This film had a much higher strain state (1.6 %), as compared to $SrTiO_3$ on $DyScO_3$ (~0.9 %) with an average in-plane lattice constant of 3.967±0.005 Å (out-of-plane = 3.874±0.001 Å). The $SrTiO_3$ films on $GdScO_3$ exhibit the same epitaxial relationship as described for films on $DyScO_3$. The dielectric permittivity data as function of temperature for $SrTiO_3$ under this higher strain state shows a T_{max} near 360 K (Fig. 5.11). This falls within the range for the thermodynamically predicted transition (290 to 550 K) for 1.6 % strain.[17] A room temperature measurement of the hysteresis loop confirms that the $SrTiO_3$ is ferroelectric (Fig. 5.12). This clearly indicates that the ferroelectricity and the large shift in the transition temperature is predominantly due to the in-plane strain. Also, it is possible that the shoulder in the dielectric constant data is the predicted tilt transition.
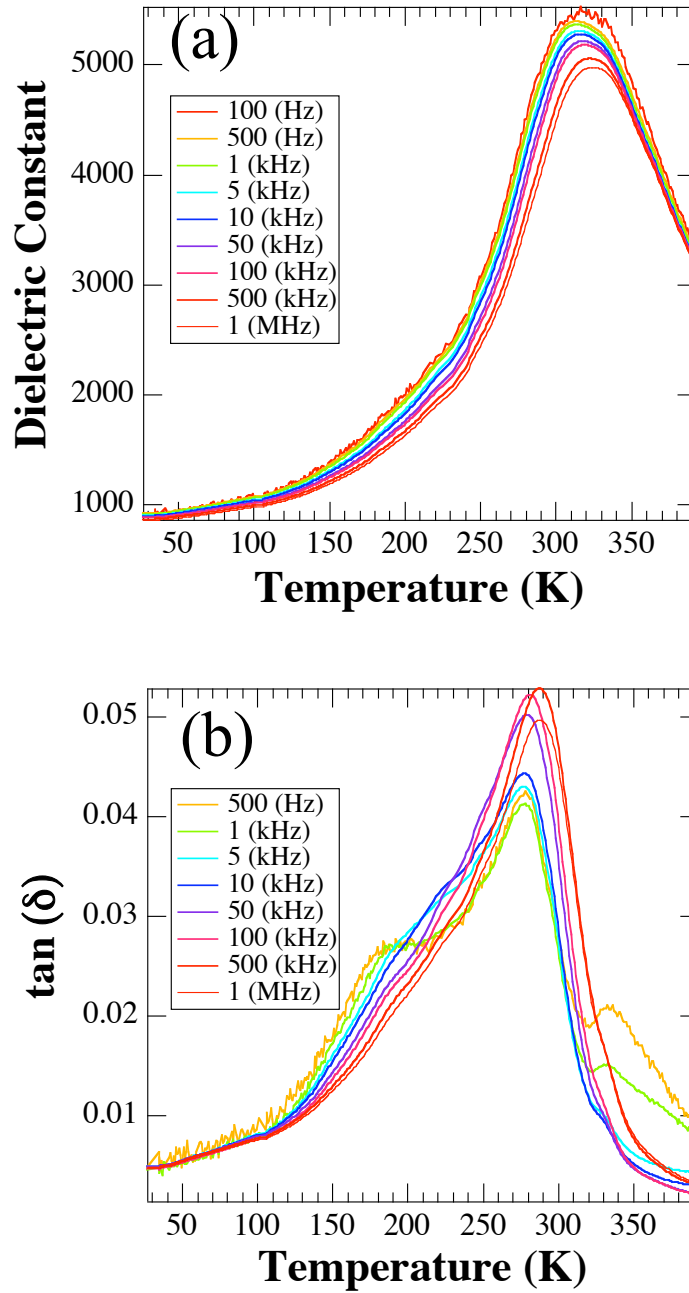
Fig. 5.11 (a) In-plane dielectric constant ($K_{\text{In-Plane}}$) and (b) tan δ as a function of temperature of a 250 Å thick strained $SrTiO_3/GdScO_3$ film.
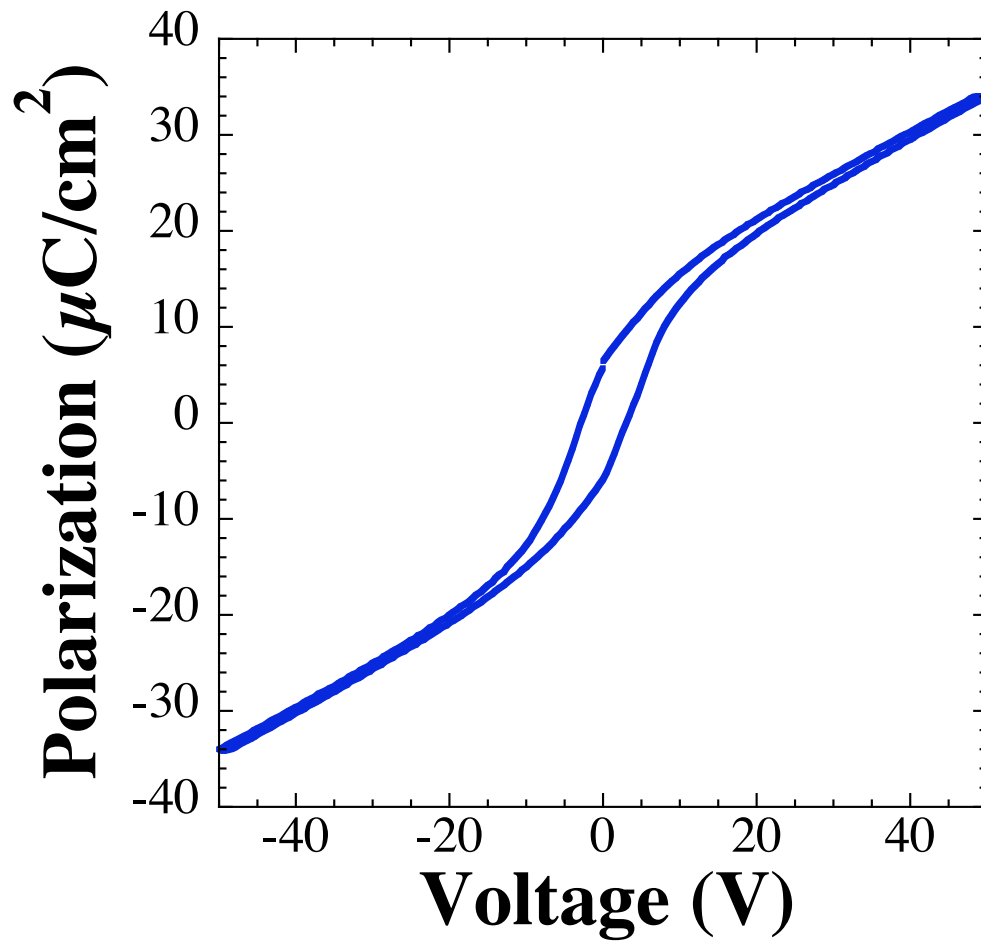
Fig. 5.12 Hysteresis loop measured at room temperature for 250 Å thick SrTiO$_3$ film grown on GdScO$_3$

5.5 Conclusions

In summary, strained epitaxial $SrTiO_3$ films grown on (101) $DyScO_3$ are relaxor ferroelectrics. The maximum permittivity is close to that of pure $SrTiO_3$ single crystals at 4 K, yet the T_{max} of the film is near 250 K in the case of $SrTiO_3$ on $DyScO_3$ and near 360 K for $SrTiO_3$ on $GdScO_3$. This agrees well with thermodynamic predictions of the effect of biaxial strain on ferroelectricity in $SrTiO_3$.[16,17] Well-defined polarization hysteresis is observed at lower temperatures, indicating that the material is ferroelectric. The frequency dependence of the dielectric constant was well described by the Vogel-Fulcher equation. This, coupled with the observation of a more normal ferroelectric transition after the sample was cooled under a dc field, indicates the material is relaxor ferroelectric. The induction of the high ferroelectric transition temperature is attributed to the high strain levels, while the relaxor behavior is likely due to scandium being present in the film.

References.

[1] K. A. Muller, W. Berlinger, and H. Bukard, Phys. Rev. B **19**, 3593 (1973).

[2] R. C. Neville, B. Hoenisen, and C. A. Mead, J. Appl. Phys. **43**, 2124 (1972).

[3] O. Tikhomirov, H. Jiang, and J. Levy, Phys. Rev. Lett. **89**, 147601 (2002).

[4] A. Yamanaka, M. Kataoka, Y. Inaba, K. Inoue, B. Hehlen, and E. Courtens, Europhys. Lett. **50**, 688 (2000).

[5] J. G. Bednorz and K. A. Müller, Phys. Rev. Lett. **52**, 2289 (1984).

[6] W. Kleemann, J. Dec, Y. G. Wang, P. Lehnen, and S. A. Prosandeev, J. Phys. Chem. Solids **61**, 167 (2000).

[7] C. Ang, Z. Yu, P. M. Vilarinho, and J. L. Baptista, Phys. Rev. B **57**, 7403 (1998).

[8] C. Ang, Z. Yu, and Z. Jing, Phys. Rev. B **61**, 957 (2000).

[9] E. Hegenbarth, Phys. Status Solidi **6**, 333 (1964).

[10] P. A. Fleury and J. M. Worlock, Phys. Rev. **174**, 613 (1968).

[11] J. Hemberger, P. Lunkenheimer, R. Viana, R. Bohmer, and A. Loidl, Phys. Rev. B **52**, 13159 (1995).

[12] D. Fuchs, C. W. Schneider, R. Schneider, and H. Rietschel, J. Appl. Phys. **85**, 7362 (1999).

[13] M. Itoh, R. Wang, Y. Inaguma, T. Yamaguchi, Y.-J. Shan, and T. Nakamura, Phys. Rev. Lett. **82**, 3540 (1999).

[14] H. Uwe and T. Sakudo, Phys. Rev. B **13**, 271 (1976).

[15] H.-C. Li, W. Si, R.-L. Wang, Y. Xuan, B. T. Liu, and X. X. Xi, Mater. Sci. Eng. B **56**, 218 (1998).

[16] N. A. Pertsev, A. K. Tagantsev, and N. Setter, Phys. Rev. B **61**, R825 (2000); **65**, 219901(E) (2002).

[17] J. H. Haeni, P. Irvin, W. Chang, R. Uecker, P. Reiche, Y. L. Li, S. Choudhury, W. Tian, M. E. Hawley, B. Craigo, A. K. Tagantsev, X. Q. Pan, S. K. Streiffer, L. Q. Chen, S. W. Kirchoefer, J. Levy, and D. G. Schlom, Nature **430**, 758 (2004).

[18] J.H. Haeni, J. Lettieri, M. Biegalski, S. Trolier-McKinstry, D.G. Schlom, S-G. Lim, T.N. Jackson, M.M. Rosario, J.L. Freeouf, R. Uecker, P. Reiche, A. Ven Graitis, C.D. Brandle, and G. Lucovsky, (unpublished).

[19] M. D. Biegalski, J. H. Haeni, S. Trolier-McKinstry, D. G. Schlom, C. D. Brandle, and A. J. Ven Graitis, J. Mater. Res. **20**, 952 (2005).

[20] J. H. Haeni, C. D. Theis, and D. G. Schlom, J. Electroceram. **4**, 385 (2000).

[21] G. W. Farnell, I. A. Cermak, P. Silvester, and S. K. Wong, IEEE Trans. Sonics Ultrason. **SU-17**, 188 (1970).

[22] O. G. Vendik, S. P. Zubko and M. A. Nikolskii, Zh. Tekh. Fiz. **69**, 1 (1999) [Sov. Phys. Tech. Phys. **44**, 349 (1999)].

[23] S. S. Gevorgian, T. Martinsson, P. L. Linner and E. L. Kollberg, IEEE Trans. Microwave Theory Tech. **44**, 896 (1996).

[24] S. B. Qadri, J. S. Horwitz, D. B. Chrisey, R. C. Y. Auyeung, and K. S. Grabowski, Appl. Phys. Lett. **66**, 1605 (1995).

[25] H.J. Scheel, Z. Krist. **143** (1976) 417.

[26] P. I. Nabokin, D. Souptel, and A. M. Balbashov, J. Cryst. Growth **250**, 397 (2003).

[27] Y. L. Li, S. Choudhury, J. H. Haeni, M. D. Biegalski, A. Vasudevarao, A. Sharan, H. Z. Ma, J. Levy, V. Gopalan, S. Trolier-McKinstry, D. G. Schlom, and L. Q. Chen (unpublished).

[28] H. C. Li, W. Si, A. D. West, and X. X. Xi, Appl. Phys. Lett. **73**, 190 (1998).

[29] M. Lippmaa, N. Nakagawa, M. Kawasaki, S. Ohashi, Y. Inaguma, M. Itoh, and H. Koinuma, Appl. Phys. Lett. **74**, 3543 (1999).

[30] L. D. Madsen, C. N. L. Johnson, S. N. Jacobsen, U. Helmersson, S. Rudner, I. Ivanov, L.-D. Wernlund, L. Ryen, and E. Olsson, Microelectron. Eng. **29**, 123 (1995).

[31] T. Ostapchuk, J. Petzelt, V. Zelezny, A. Pashkin, J. Pokorny, I. Drbohlav, R. Kuzel, D. Rafaja, B. P. Gorshunov, M. Dressel, C. Ohly, S. Hoffmann-Eifert, and R. Waser, Phys. Rev. B **66**, 235406 (2002).

[32] D. Viehland, S.J. Jang, L.E. Cross, and M. Wuttig, J. Appl. Phys. **68**, 2916 (1990).

[33] H. Vogel, Z. Phys. **22**, 645 (1921).

[34] G. Fulcher, J. Am. Ceram. Soc. **8**, 339 (1925).

[35] D. Viehland, S. Jang, L. E. Cross, and M. Wuttig, Phil. Mag. B **64**, 335 (1991).

[36] J-P. Maria, W. Hackenberger, and S. Trolier-McKinstry, J. Appl. Phys. **84**, 5147 (1998).

[37] S. Chattopadhyay, A. R. Teren, J. H. Hwang, T. O. Mason, and B. W. Wessels, J. Mater. Res. **17**, 669 (2002).

[38] M. D. Biegalski, D. D. Fong, J. A. Eastman, P. H. Fuoss, W. Tian, X. Q. Pan, M. E. Hawley, R. Uecker, P. Reiche, S. K. Streiffer, S. Trolier-McKinstry, and D. G. Schlom (unpublished).

[39] G. A. Samara and L. A. Boatner, Phys. Rev. B **61**, 3889 (2000).

[40] W. Kleemann, G. A. Samara, and J. Dec, in *Polar Oxides: Properties, Characterization, and Imaging*, edited by R. Waser, U. Böttger, and S. Tiedke (Wiley-VCH, Weinheim, 2005), pp. 275-301.

[41] V. V. Lemanov, A. V. Sotnikov, E. P. Smirnova, and M. Weihnacht, Fiz. Tverd. Tela (St. Petersburg) **44**, 1948 (2002).

[42] A.J. Moulson and J. M. Herbert *Electroceramcs: Materials•Properties• Applications*, (Chapman & Hall, London, 1990) pp. 76-84.

Chapter 6

Structure and Critical Thickness of Semiconductor Quality SrTiO$_3$ Films Grown on (101) DyScO$_3$[**]

6.1 Abstract

Strained epitaxial SrTiO$_3$ films were grown on (101) DyScO$_3$ substrates by reactive molecular-beam epitaxy. The strain state and structural perfection of films with thicknesses ranging from 50 Å to 1000 Å were examined using x-ray scattering. The critical thickness at which misfit dislocations were introduced was between 350 Å and 500 Å. These films have the narrowest rocking curves (full width at half maximum) ever reported for any heteroepitaxial oxide film (0.0018°). Only a modest amount of relaxation is seen in films exceeding the critical thicknesses even after high temperature annealing at 750 °C. The dependence of strain relaxation on direction is attributed to the anisotropy of the substrate constraint. These SrTiO$_3$ films show structural quality more typical of semiconductor materials, than perovskite materials; their structural relaxation behavior also shows similarity to that of semiconductor materials.

[**] Parts of this chapter are reproduced from M. D. Biegalski, D. D. Fong, J. A. Eastman, P. H. Fuoss, W. Tian, X. Q. Pan, M. E. Hawley, R. Uecker, P. Reiche, S. K. Streiffer S. Trolier-McKinstry, and D. G. Schlom (submitted to J. Appl. Phys).

6.2 Introduction

Strain can have a dramatic effect on the properties of thin films. Strain-induced shifts in magnetic, [1-3] ferroelectric[4-10] and superconducting[11-13] transitions have been reported. For the case of strained $SrTiO_3$, a ferroelectric transition has been induced in the vicinity of room temperature even though pure, strain-free $SrTiO_3$ is not ferroelectric at any temperature.[9] These strained $SrTiO_3$ films grown on (101) $DyScO_3$ substrates[14] show a tunability of the dielectric constant at room temperature of 82% at 10 GHz[9] and dielectric constant maxima near 20,000 at 500 Hz.[17] Presumably, these properties may change with film thickness, as the strain should relax due to dislocation generation in thicker films. In this paper we investigate both the critical thickness at which (001) $SrTiO_3$ films on (101) $DyScO_3$ begin to relax and how this relaxation proceeds as the film thickness increases.

6.3 Experimental Procedure

Untwinned single crystals of the orthorhombic perovskite $DyScO_3$ were grown by the Czochralski method.[18-20] These crystals were oriented along the (101) plane and cut into 10 mm × 10 mm × 1 mm substrates with a surface suitable for epitaxy.[21] $DyScO_3$ is free of phase transitions from room temperature to 1200 K and has thermal expansion coefficients comparable to $SrTiO_3$ and other perovskites.[22] This and the low vapor pressure of its constituents make it a suitable substrate for the epitaxial growth of perovskites, including $SrTiO_3$.

These substrates were cleaned in an ultrasonic bath for 10 min in Micro cleaning solution,[23] followed by acetone, isopropyl alcohol, and deionized water and then spun dry.[24] $SrTiO_3$ films were grown by reactive molecular-beam epitaxy (MBE) in a Veeco

930 growth chamber to thicknesses of 50, 100, 250, 350, 500, 1000, and 2000 Å. These films were grown with a substrate temperature of 650 °C (by optical pyrometer) with a background pressure $3x10^{-6}$ Torr of O_3/O_2 (~10% O_3). Reflection High Energy Electron Diffraction (RHEED) was implemented to monitor the growth[25] and allow for control of the film stoichiometry in real time.

Structural and microstructural characterization of the films was then completed. The 2000 Å thick film was riddled with cracks and was not analyzed by x–ray diffraction. For the remaining films, the lattice parameters and crystalline perfection were examined via x–ray scattering both at the Advanced Photon Source (APS) at Argonne National Laboratory and using a Philips X'pert Material Research Diffractometer.[26] The synchrotron x-ray source was used to examine the in-plane lattice parameter of the thinner films in grazing incident x–ray diffraction with a fixed incident angle of 0.5° (except for the 50 Å, film where higher intensity was needed and an incident angle of 0.3° was used).[27] The lattice parameters of the 100 Å thick $SrTiO_3$ film were monitored *in situ* as a function of oxygen partial pressure at 700 °C in an atmospherically controlled environment.[28] High-resolution transmission electron microscopy was performed on a JEOL 4000 transmission electron microscope[29] to image the dislocations and determine the Burger's vector. In addition, the film surfaces were imaged using Veeco Metrology IIIA scanning probe microscopes[30] in intermittent contact mode at 0.6 Hz.

6.4 Results and Discussion

6.4.1 Critical Thickness Determination by Diffraction

The (101) plane of $DyScO_3$ consists of a rectilinear surface net spanned by the $[\bar{1}01]$ and [010] $DyScO_3$ vectors. This surface is schematically shown in Fig. 6.1 where it can be seen that the $DyScO_3$ $[\bar{1}01]$ axis has a slightly shorter pseudo-cubic lattice parameter of $\frac{1}{2}[\bar{1}01]$ = 3.9474±0.0005 Å, while the pseudo-cubic lattice spacing along the [010] axis is $\frac{1}{2}[010]$ = 3.9513±0.0005 Å. When $SrTiO_3$ is grown on (101) $DyScO_3$ the (001) $SrTiO_3$ plane is parallel to the (101) $DyScO_3$ plane and the (100) $SrTiO_3$ plane aligns parallel to the (010) $DyScO_3$. The epitaxial relationship is (001) $SrTiO_3$ || (101) $DyScO_3$ and [100] $SrTiO_3$ || $[\bar{1}01]$ $DyScO_3$. Commensurate (001) $SrTiO_3$ films grown on (101) $DyScO_3$ substrates are thus strained by $\left(a_{sub} - a_{film}\right)/a_{film}$ = 1.19% along $\left[\bar{1}01\right]$ $DyScO_3$ and 1.09% along [010] $DyScO_3$ (where a_{sub} is the in-plane spacing of the rectilinear surface net of the substrate and a_{film} is the lattice parameter of unstrained $SrTiO_3$). It should be noted that there is some sample to sample variation in the $DyScO_3$ lattice constant. Thus the strain state was calculated on after measuring the film and substrates lattice parameters for each specimen.

The x-ray data in Fig. 6.2(a) show the crystal truncation rod (CTR) around the 206-type $SrTiO_3$ peaks in a 500 Å thick film. The oscillations extend far in reciprocal space from the $SrTiO_3$ peak with a constant period (see Fig. 6.2(b)). The regularity of the oscillations shown is typical for all of the films and indicates the presence of long range structural order and a smooth film surface, since the breadth of scattering of the CTR is
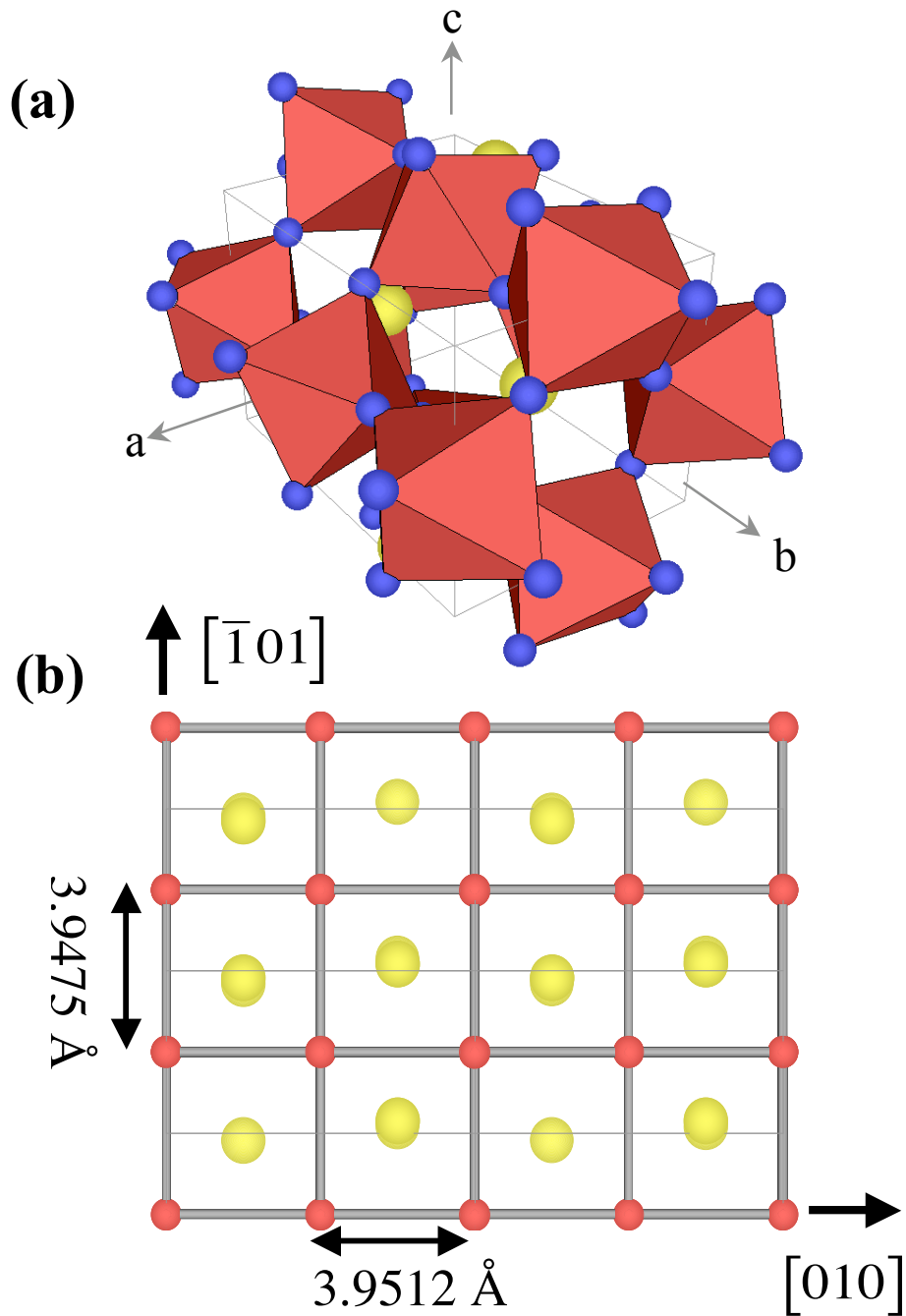
Fig. 6.1 (a) DyScO₃ unit cell in which the ScO₆ coordination polyhedra are shaded, showing the tilts of the octahedra. (b) Schematic of the in-plane rectilinear growth net of (101) DyScO₃ with a slight asymmetry of the two in-plane directions due to the orthorhombicity of the unit cell. (Note: the oxygen atoms were not shown for clarity)
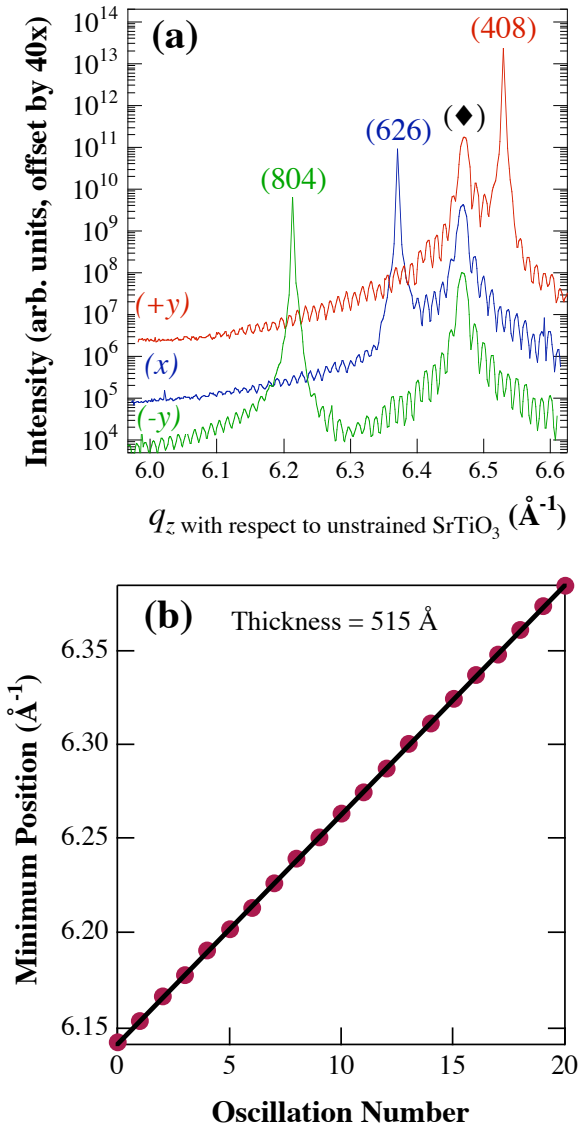
Fig. 6.2 (a) Crystal truncation rod (CTR) of 500 Å thick SrTiO$_3$ 206 peak ($\blacklozenge$) for three different axes showing the 626 (*x*), 408 (+*y*), and 804 (-*y*) DyScO$_3$ peaks. (b) shows the fit of the film thickness to the oscillation period. The regularity of this period of the oscillations over a large region of reciprocal space and thickness oscillations extending far from the Bragg peak along the CTR show the high crystalline quality of the film. (Note: the reciprocal lattice vectors q_z correspond to those of the unstrained SrTiO$_3$ film with $a = 3.905$ Å.)

inversely proportional to the roughness of the surface.[31] This quality of films is typically

found in high quality semiconductor materials like GaAs, but is rarely found for

perovskite oxide materials. As can also be seen in Fig. 6.2(a), there are three distinct

positions for the $DyScO_3$ peak.

The three peaks near the $SrTiO_3$ 206-type peaks are the $DyScO_3$ 646, $6\bar{4}6$, 408,

and 804 peaks. Since the d spacing of the $DyScO_3$ 646 and $6\bar{4}6$ peaks is the same, this

will give a 2-fold symmetry along the [010] $DyScO_3$ axis. Along the orthogonal $[\bar{1}01]$

$DyScO_3$ axis, however, the 408 and 804 $DyScO_3$ peaks do not have the same d spacing

and thus have different positions in Fig. 6.2(a). This can be seen schematically in Fig.

6.3, where the $SrTiO_3$ and $DyScO_3$ lattices are represented in reciprocal space. In this

figure the $DyScO_3$ reciprocal lattice is slightly tilted from the $SrTiO_3$ due to the $[10\bar{1}]$

direction not being parallel to the $[10\bar{1}]$ reciprocal lattice vector in orthorhombic

$DyScO_3$. As the y coordinate of the reciprocal lattice, q_y, is increased from the origin, the

coordinate of the reciprocal lattice, q_z, position of $DyScO_3$ will be higher than that of the

$SrTiO_3$ along the same CTR. (Note: the reciprocal lattice vectors q_y and q_z correspond to

unstrained $SrTiO_3$ with a = 3.905 Å.) This can be seen in the top scan of Fig. 6.2(a),

where the 408 $DyScO_3$ occurs at a larger q_z than the $SrTiO_3$ peak and is labeled as the

$(+y)$ axis. If q_y is negative, then the q_z position of the 804 $DyScO_3$ peak is lower than the

206 $SrTiO_3$ peak along the CTR. This is seen as the lowest scan in Fig. 6.2(a) and is

labeled as the $(-y)$ axis.

The lattice parameters of $SrTiO_3$ were determined to identify the critical thickness

for the onset of relaxation of the strained $SrTiO_3$ thin films. XRD data along the CTR

Fig. 6.3 Schematic of the epitaxy of the SrTiO$_3$ (■) and DyScO$_3$ (●) lattice in reciprocal space. Along SrTiO$_3$ q_y axis the DyScO$_3$ lattice is canted at an angle of ~2° as compared to the SrTiO$_3$ lattice due to the different orientations of the [$\bar{1}$01] DyScO$_3$ and [001] SrTiO$_3$. The tilt in the figure is exaggerated for clarity. The arrow shows the scan direction along the CTRs used for the scans in Fig. 6.2(a). (Note: the reciprocal lattice vectors q_y and q_z are those of the unstrained SrTiO$_3$ film with a = 3.905 Å.)

were fit to determine the thickness of the films and the out-of-plane lattice constant of the SrTiO$_3$.[32] The in-plane lattice constants were then determined from the d spacings of several off axis-peaks. The lattice constants as function of film thickness are illustrated in Fig. 6.4. The out-of-plane lattice constant does not change as a function of film thickness (Fig. 6.4(a)). In Fig. 6.4(b), the in-plane lattice parameter of the SrTiO$_3$ is commensurate for the shorter in-plane axis (the [$\bar{1}$01] DyScO$_3$ direction), but some relaxation is observed for films 500 Å thick and thicker along the longer in-plane axis (the [010] DyScO$_3$ direction). This indicates that onset of relaxation (the critical thickness) for this system is between 350 Å and 500 Å. It is also important to note that even at 1000 Å, the film is still ~90% coherent along the longer axis and nearly 100% coherent along the shorter axis.

The onset of relaxation deduced from the evolution of the RHEED patterns during film growth is consistent with the x-ray diffraction results. At the beginning of the growth, Fig. 6.5(a), the RHEED pattern for the substrate shows spots on an arc. After 180 Å of SrTiO$_3$ has been grown (Fig. 6.5(b)) the RHEED pattern still shows small spots for the first order diffraction rod. This pattern (Fig. 6.5(b)) also shows that the lattice constant of the SrTiO$_3$ is half that of the DyScO$_3$, illustrated by the fact that the first order diffraction spots in Fig. 6.5(b) are in the same position as the second order diffraction spots of the bare DyScO$_3$ substrate in Fig. 6.5(a). This also confirms the epitaxial relationship [100] SrTiO$_3$ || [010] DyScO$_3$, as described previously. At a film thickness of 450 Å the first order diffraction rods have broadened (Fig. 6.5(c)) indicating that the film has started to relax. The exact onset of relaxation by RHEED is difficult to
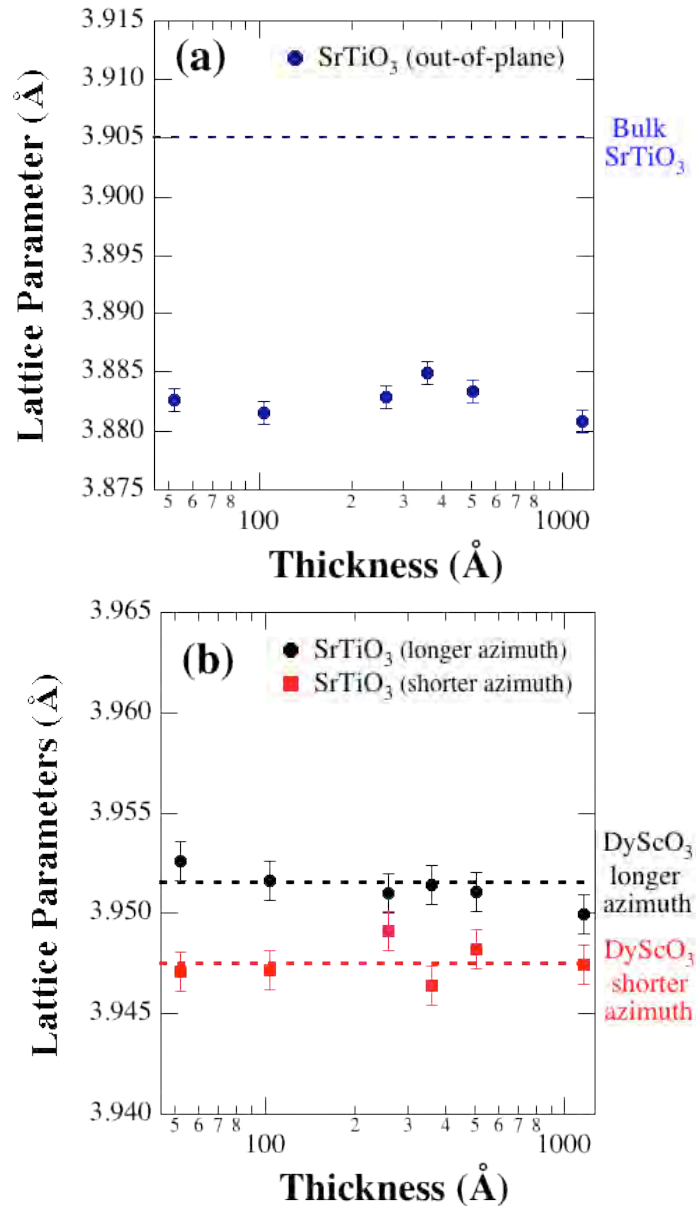
Fig. 6.4 (a) Out-of-plane and (b) in-plane lattice constants of the SrTiO$_3$ films as a function of thickness. The lattice spacing of the substrate and bulk SrTiO$_3$ are indicated by solid lines. This shows little change in the out-of-plane lattice constants, However, the in-plane lattice constants show an anisotropy consistent with the orthorhombicity of the DyScO$_3$.The in-plane lattice spacings show no relaxation along the shorter axis, but along the longer axis relaxation is apparent for films thicker than 350 Å.
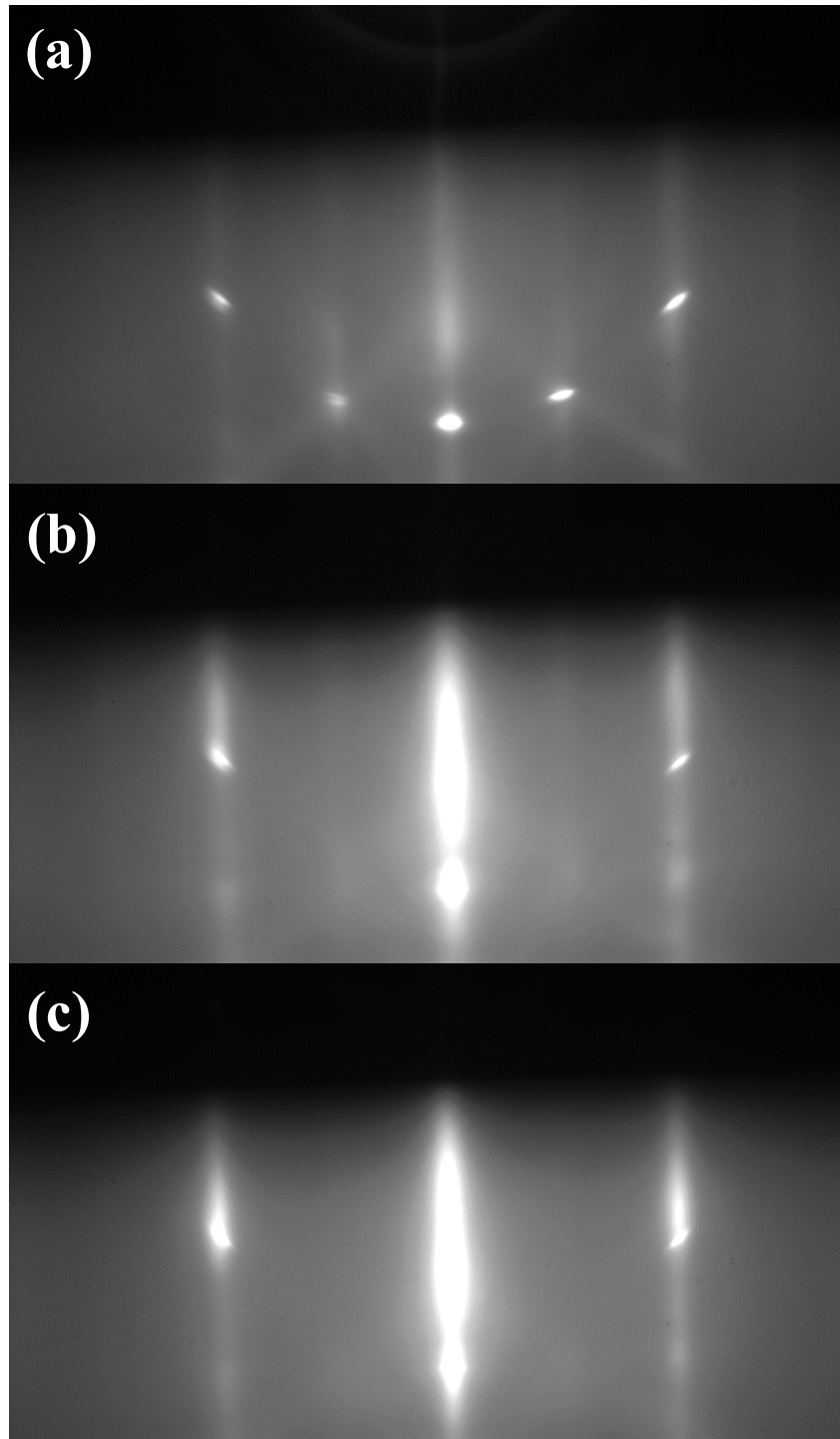
Fig. 6.5 RHEED patterns during the growth of the 500 Å thick SrTiO₃ film on DyScO₃

observed along the [110] SrTiO₃ azimuth for (a) bare DyScO₃ substrate before growth,

(b) after the growth of 180 Å of SrTiO₃, and (c) after the growth of 450 Å of SrTiO₃.

determine since the change is gradual, but by 450 Å the streaking of the first order

diffraction rods is clear. This limits the onset of relaxation to between 180 Å and 450 Å;

thus the agreement between RHEED and XRD is good.

The equilibrium critical thickness was calculated by both mechanical and energy

balance using the formulae corresponding to the equilibrium thickness at which it

becomes energetically favorable to introduce dislocations, as described by

Matthews-Blakeslee (Eq. 2.10).[33]

$$h_c = \frac{(1 - v\cos^2(\theta))}{8\pi} \frac{b}{f(1+v)} \ln\left(\frac{\alpha \ h_c}{b}\right)$$
Eq. 6.1

where h_c is the critical thickness, v is Poisson's ratio, f is the misfit strain between the

film and substrate, θ is the angle between the Burger's vector and the dislocation line of

the misfit dislocation, α is the cut-off radius of the dislocation core (generally between 1

and 4) and b is the Burger's vector. To use Eq 6.1, it is necessary to know more about the

relaxation mechanism, specifically the Burger's vector. From TEM in Fig. 6.6 the

Burger's circuit shows that Burger's vector is in the plane of the film-substrate interface,

and could be either $\frac{a}{2}\langle 110\rangle$ or $a\langle 100\rangle$. The most likely Burger's vector is $a\langle 100\rangle$ since it

is observed in several perovskites, such as $BaTiO_3$.[34,35] The Fourier transformation of the

TEM (Fig. 6.6(b)) shows an extra plane of atoms in the $SrTiO_3$ films, confirming that

these films are under tensile stress. The most likely slip system is $\langle 100\rangle - \{011\}$, which is

typical for a perovskite system. [34-37]
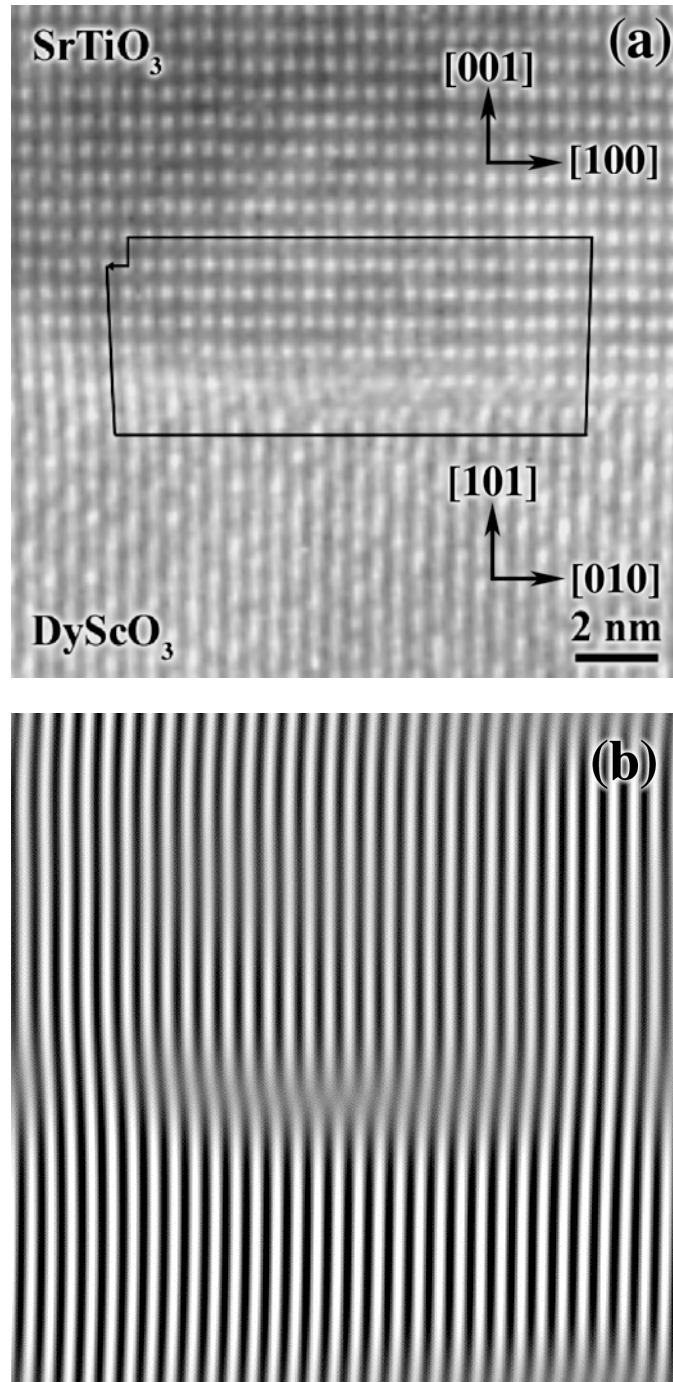
Fig. 6.6 (a) HRTEM of a 500 Å thick SrTiO$_3$ film showing a single dislocation core with

a Burger's vector of $\frac{a}{2}\langle 110 \rangle$ or $a\langle 100 \rangle$ and (b) a lattice fringe (by Fourier-transform

technique) showing the extra half plane in the SrTiO$_3$ film.

This information was used to calculate the thermodynamic critical thickness. The Poisson's ratio (υ) of SrTiO$_3$ was calculated from $\upsilon = -s_{12}/s_{11}$ using the temperature dependent compliances of SrTiO$_3$ from Rupprecht and Winter extrapolated to 700 °C.[38] Using the Matthews-Blakeslee criterion with the $\langle 100 \rangle - \{011\}$ slip system and $\upsilon = 0.23$ gives a critical thickness of 60 Å. The discrepancy between the equilibrium (Matthews-Blakeslee) critical thickness at which it becomes energetically favorable to introduce dislocations and the observed critical thickness is not surprising because the experimentally observed critical thickness is kinetically limited by Peierls-Nabarro stress, dislocation nucleation, dislocation interactions, and other potential barriers impeding dislocation introduction, especially at relatively low growth temperatures.[34-37,39,40]

This relaxation primarily along one direction, observed in Fig. 6.4(b), was initially unexpected. Using the DyScO$_3$ lattice constants reported in the International Centre for Diffraction Data (ICCD) powder diffraction file, a cut along the (101) plane produces an in-plane rectilinear surface net with spacings of 3.9439 and 3.9444 Å along the $\frac{1}{2}[\bar{1}01]$ DyScO$_3$ and $\frac{1}{2}[010]$ DyScO$_3$ directions, respectively.[41] This creates a lattice mismatch of 0.996% along the DyScO$_3[\bar{1}01]$ and 1.009% along the DyScO$_3[101]$ with SrTiO$_3$ (3.905 Å), yielding a biaxial tensile stress with $\varepsilon_{11} \approx \varepsilon_{22}$ in unrelaxed films (where ε_{11} and ε_{22} are in-plane strains). The difference of 0.0009 Å between the two orthogonal directions of the surface net is on the order of the resolution of our x-ray diffractometer. The x-ray data on the DyScO$_3$ single crystal substrates used in this work however, indicate in-plane surface net spacings of 3.9513±0.0004 Å and 3.9474±0.0003 Å along the $\frac{1}{2}[\bar{1}01]$ and $\frac{1}{2}[010]$ DyScO$_3$ directions, respectively. The difference of 0.0039 Å

between the two is much larger than previously reported. This discrepancy may be attributed to differences in stoichiometry between our single crystals and the powder reported in the ICCD powder diffraction file. It is almost certainly the difference in spacings for the two orthogonal in-plane directions ($\varepsilon_{11} \neq \varepsilon_{22}$) that drives the anisotropy in the relaxation of the SrTiO$_3$ films. Relaxation can be seen to occur along the more strained in-plane direction first in Fig. 6.4(b), as expected.

The rocking curves, in ω, for these films show a full width at half maximum (FWHM) of the 002 SrTiO$_3$ peak that ranges from 6.5 to 18 arc sec (0.0018 -0.0050°). As Fig. 6.7(a) shows, the rocking curve FWHM of the 350 Å thick film is just 6.5 arc sec (0.0018°) which is the resolution limit of the diffractometer. This is the narrowest rocking curve reported for any heteroepeitaxial oxide thin film.[42] These high quality crystallinity indicated by the rocking curve is more typical of semiconductors (typically 10's of arc sec) than most perovskites (typically 100's of arc sec).[42,43] Similar peak widths were found off axis and in the grazing incidence diffraction measurements at the Advanced Photon Source, indicating these films have a high degree of uniformity and structural perfection. This high crystalline quality is a consequence of the structural perfection of the DyScO$_3$ substrate, the template for epitaxial growth. If the rocking curve of the film and substrate are overlaid, as is done in Fig. 6.7(b), they have identical shapes and FWHM.

The critical thickness can also be observed in the shape of the rocking curves of these films (see Fig. 6.8). Films thicker than 350 Å have sharp, resolution-limited rocking curve widths. At thicknesses above the critical thickness, the rocking curves have
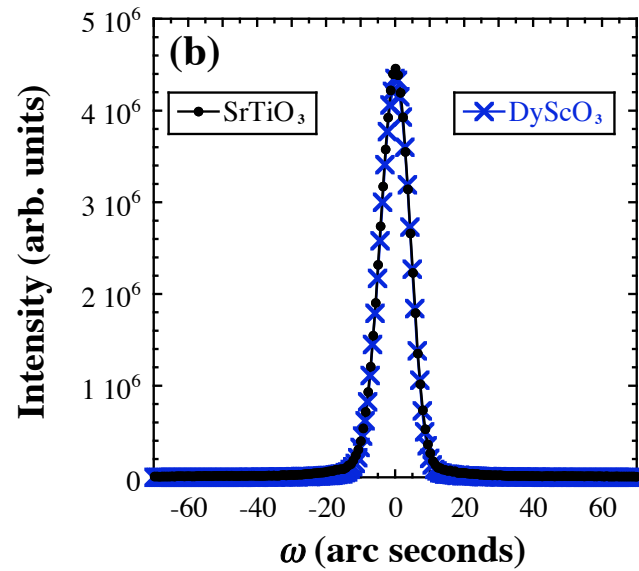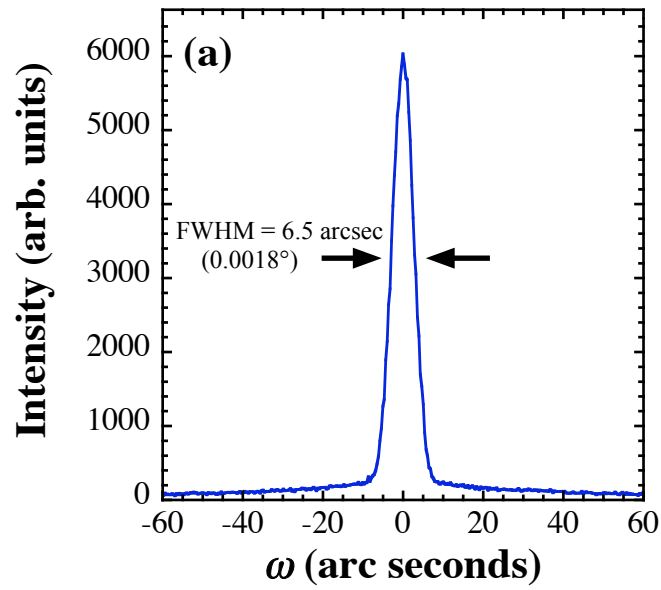
Fig. 6.7 (a) Rocking curve of the SrTiO$_3$ 002 peaks for a 350 Å thick SrTiO$_3$ film, the

FWHM is 6.5 arc sec (instrument-limited). (b) Scaled rocking curves of the 002 SrTiO$_3$

film peak and 202 DyScO$_3$ showing identical shapes. (Note: the number of data points in

for the rocking curves in (b) is actually much greater than the number depicted)
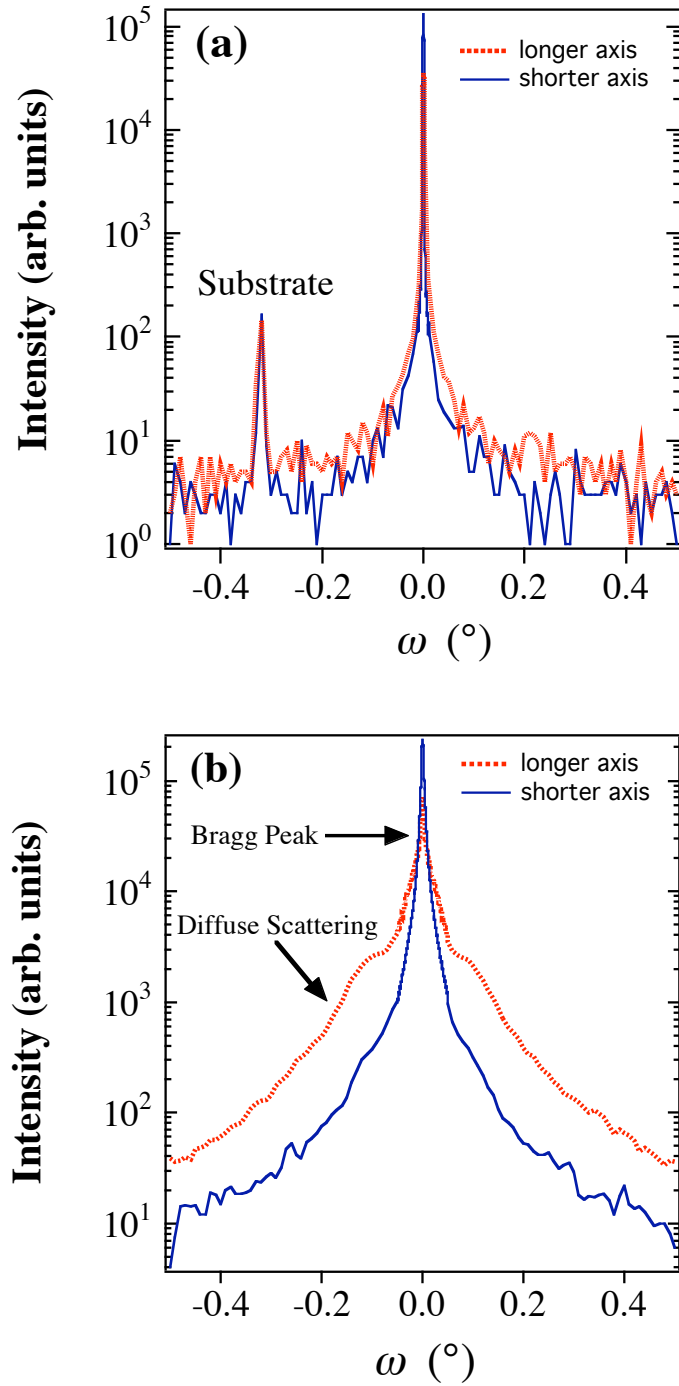
Fig. 6.8 Rocking curves of the 002 SrTiO$_3$ in orthogonal directions for (a) 350 Å and (b) 1000 Å thick films. The longer scan is taken along the [$\bar{1}$01] DyScO$_3$, the shorter axis scan is taken along the [010] DyScO$_3$.

components due to both Bragg and diffuse scattering. The sharp peak is attributed to the long range crystalline order of the unrelaxed portion of the film; the diffuse scattering is consistent with the existence of dislocations and local relaxation of the film as is typically seen in semiconductor films.[44,45] The onset of the diffuse scattering occurs for film thicknesses between 350 and 500 Å and the magnitude of the diffuse component is larger for the 1000 Å film. The rocking curves also reflect the anisotropy of the relaxation. In Fig. 6.8(a) the rocking curves along the two perpendicular in-plane axes are almost identical for the coherent films. In contrast, the 1000 Å film shows different shapes in the two orthogonal directions (Fig. 6.8(b)). As expected, the rocking curve along the longer axis shows more diffuse scattering than the rocking curve along the shorter axis, while both curves have the same integrated areas. This is consistent with the relaxation occurring preferentially along the longer in-plane axis, were the film is under higher strain, in full agreement with the in-plane relaxation seen first along the more strained direction in Fig. 6.4(b).

6.4.2 Effects of Oxygen Annealing on Relaxation

To lower the dielectric loss of the $SrTiO_3/DyScO_3$ films, these films were annealed in 1 atm of flowing oxygen for 1 hr prior to electrical measurements[17]. To determine the effect of this reoxidation anneal on the film relaxation, the 006 peak of a 100 Å thick $SrTiO_3$ film was heated to 750 °C and was monitored *in-situ* at the Advanced Photon Source while the oxygen partial pressure was changed from 10^{-8} to 10^{1} torr. Each time the pressure was changed, the film was allowed to equilibrate for 15 min. The position of the 006 $SrTiO_3$ peak did not change during the experiment (Fig. 6.9(a)). This
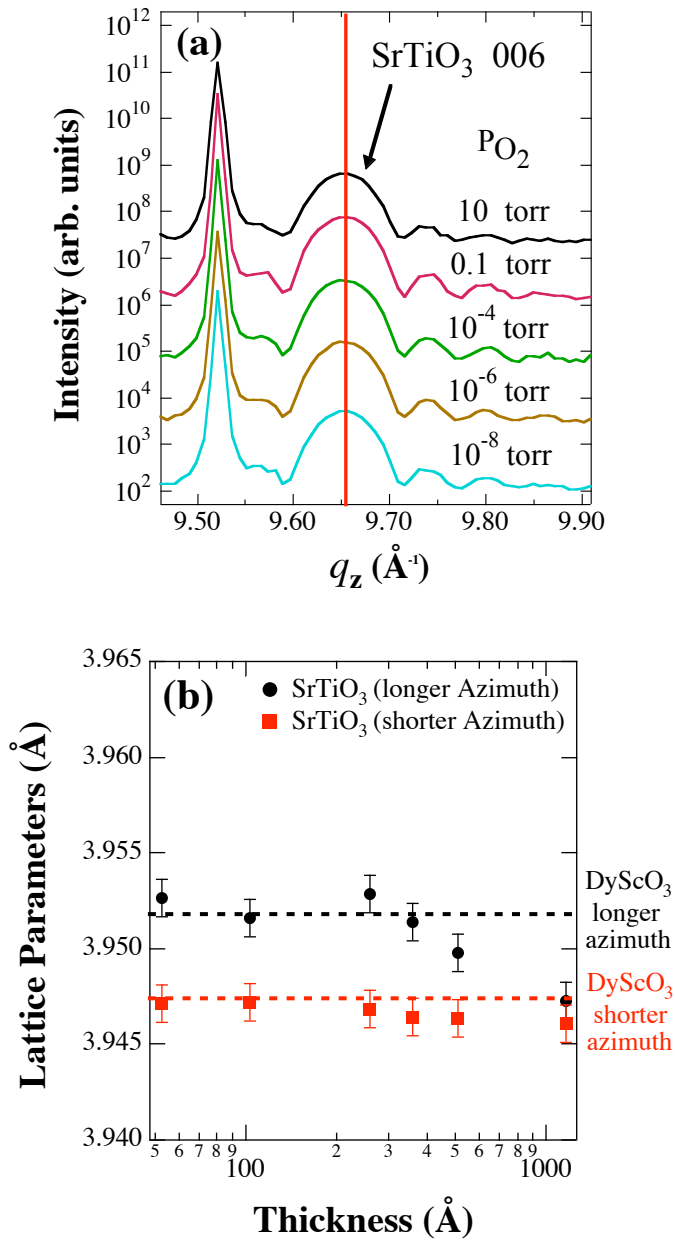
Fig. 6.9 (a) Scans of the 006 peak of a 100 Å thick SrTiO$_3$ film showing no discernable changes due to annealing the film at 750 °C in different in oxygen partial pressures and (b) in-plane lattice parameters of the films after a reoxidation anneal in 1 atm of flowing oxygen for 1h at 700 °C showing a slight increase in the relaxation of the films thicker than the critical thickness.

shows that the oxygen vacancy concentration did not affect the lattice parameter of these films. Similar insensitivity of the lattice constant of the $SrTiO_{3-x}$ to oxygen vacancies has been noted in other experiments on bulk, thin film and single crystalline $SrTiO_{3-x}$.[46,47] For films below the critical thickness, no change in the strain state during the reoxidation anneal was observed. The rest of the samples were annealed at 700 °C for 1 h in flowing oxygen (1 atm) and the lattice parameters of these films were re-measured. For the thinner films the lattice constants do not change after annealing (Fig. 6.9(b)). In contrast, the 500 and 1000 Å thick films relaxed further on annealing. This is not unexpected since the relaxation is kinetically limited; annealing would enable these films to relax and approach their thermodynamic equilibrium. It should be noted, however, that the amount of additional relaxation is modest even for the 1000 Å thick film, so that that the film is still ~80% coherent with the substrate.

6.4.3 Surface Structure Analysis

The relaxation can also be seen in AFM images of the surface structure of the films. AFM images of all the films show terraces separated by 4 Å high steps. Two examples are show in Fig. 6.10. The regular spacing of the steps indicates that films grow by the lateral propagation of their step edges (step flow). The film surfaces have an RMS roughness around 2.5 Å. Even the 2000 Å thick film, which was visibly cracked, showed step flow growth regions between the cracks (Fig. 6.10(b)).

When imaged over a longer lateral scale, it was found that the coherent films are very smooth (Fig. 6.11(a)). Once these films reach a sufficient thickness and begin to relax, the surfaces begin to form surface undulations (Fig. 6.11(b) and 11(c)). This
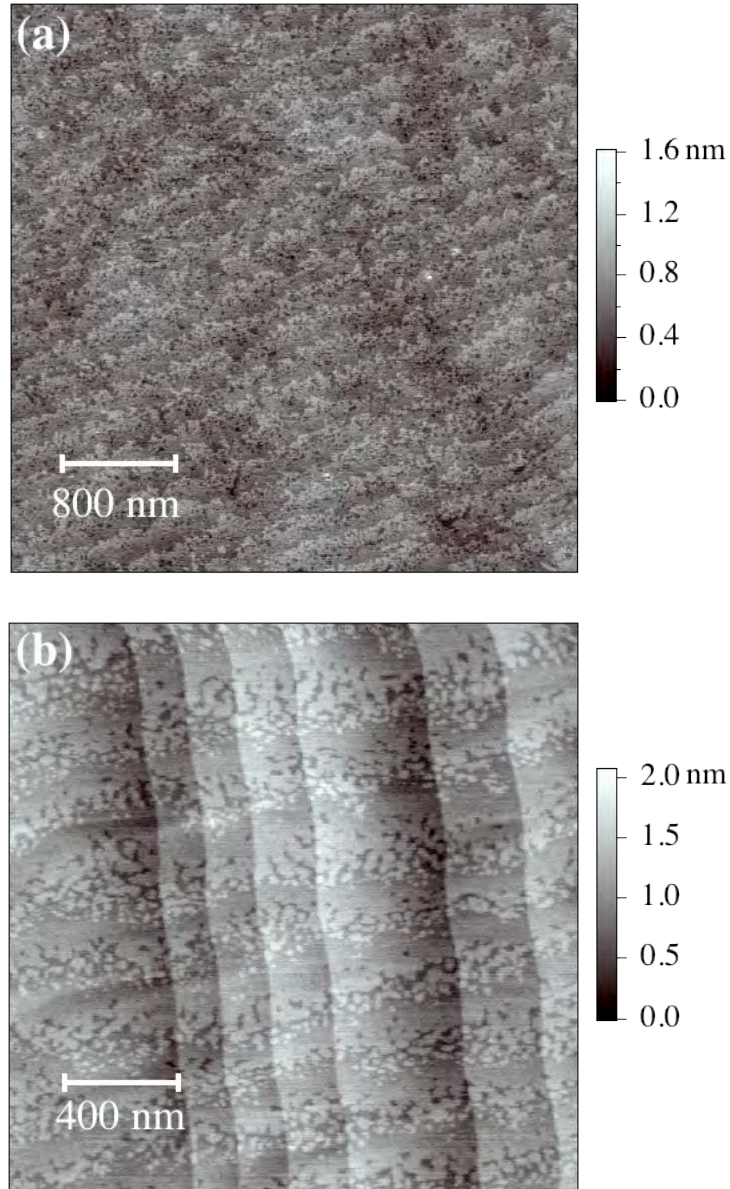
Fig. 6.10 AFM height images of (a) 250 Å and (b) 2000 Å thick films both films have ~4 Å high steps, indicating the SrTiO₃ films grew in a step flow growth mode. The edges of the AFM images are aligned with ⟨100⟩ SrTiO₃ directions.
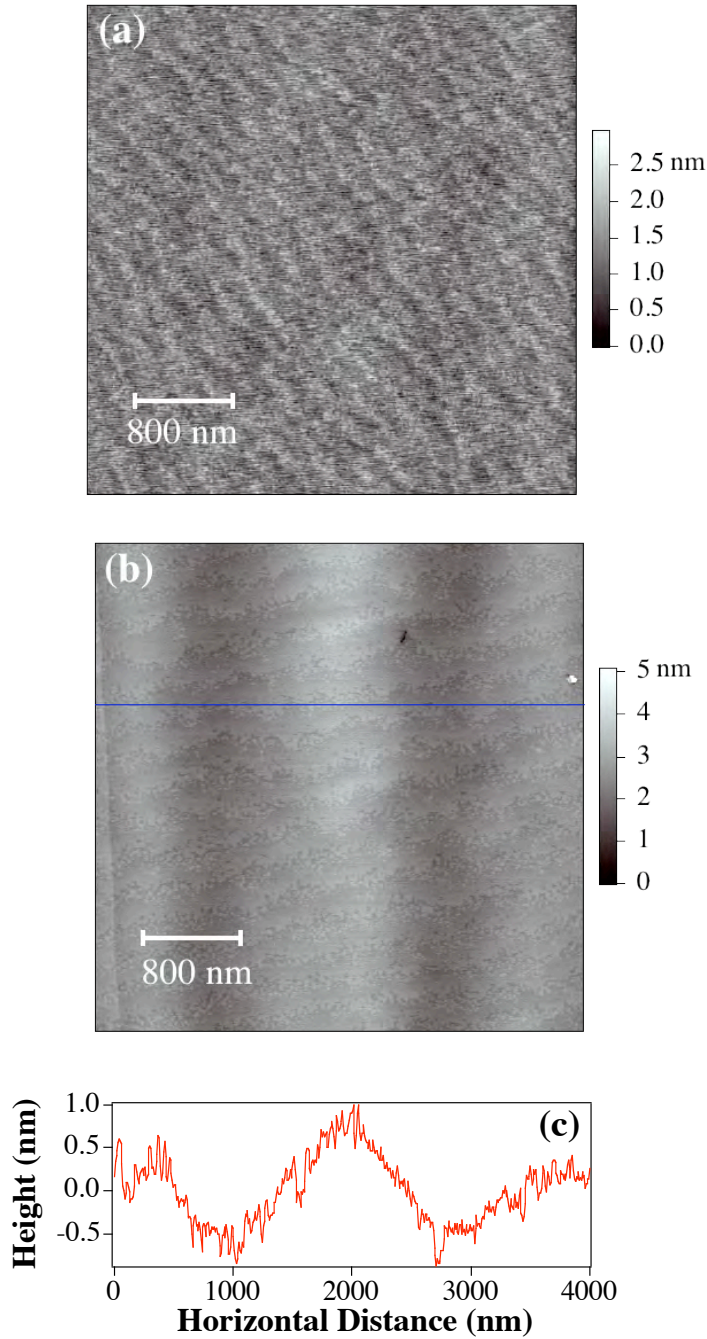
Fig. 6.11 AFM height images of (a) 350 Å thick $SrTiO_3$ film showing a very flat surface, (b) a 2000 Å thick film showing surface undulations seen in the horizontal line scan of the 2000 Å thick film. The line scan in (c) is along the longer $DyScO_3$ azimuth in which the $SrTiO_3$ film is more strained (the $[\bar{1}01]$ in-plane direction of the $DyScO_3$ substrate).

sinusoidal shape is commonly seen in strained semiconductor materials, and has been predicted and observed in films under both biaxial tensile and compressive stresses.[48-56] This surface roughening mechanism also shows the anisotropy of the stress, in that these surface undulations are only in one direction, whereas three-dimensional mounds are typically observed for uniform in-plane strain.[52]

The thicker films also show two additional features that are not seen in films below the critical thickness. There are protrusions above the surface of the film and also small steps resulting from dislocation motion (cross-hatch) that appear as depressions in the surface; both can be seen in Fig. 6.12. On closer examination the protrusions above the surface are found to be cracks (Fig. 6.13). Near these cracks the $SrTiO_3$ juts above the surface of the films. In its strained form, the out-of-plane lattice constant of $SrTiO_3$ on $DyScO_3$ is approximately 3.880 Å for all film thicknesses investigated, but the unrelaxed bulk lattice constant for $SrTiO_3$ is 3.905 Å at room temperature. Thus, when the lattice constant of the $SrTiO_3$ changes from 3.880 to 3.905 Å at the edge of the crack, the relaxed portion of the film should be thicker. If the expansion of the lattice constant was the only cause of the crack height, the film near the crack should expand by 0.6% of the thickness. The cracked areas, however, protrude ~30 Å for the 500 Å thick film and nearly 60 Å for the 1000 Å thick film, indicating a change of nearly 6%. A likely explanation is that that the film has delaminated from the substrate near the crack to attain this height (See Fig. 6.13(c)). Another possibility is that surface diffusion leads to the cracks as described by Grinfeld[57] and by Srolovitz.[58] It has been shown in several systems that crack like features with cusps can develop in strained materials though
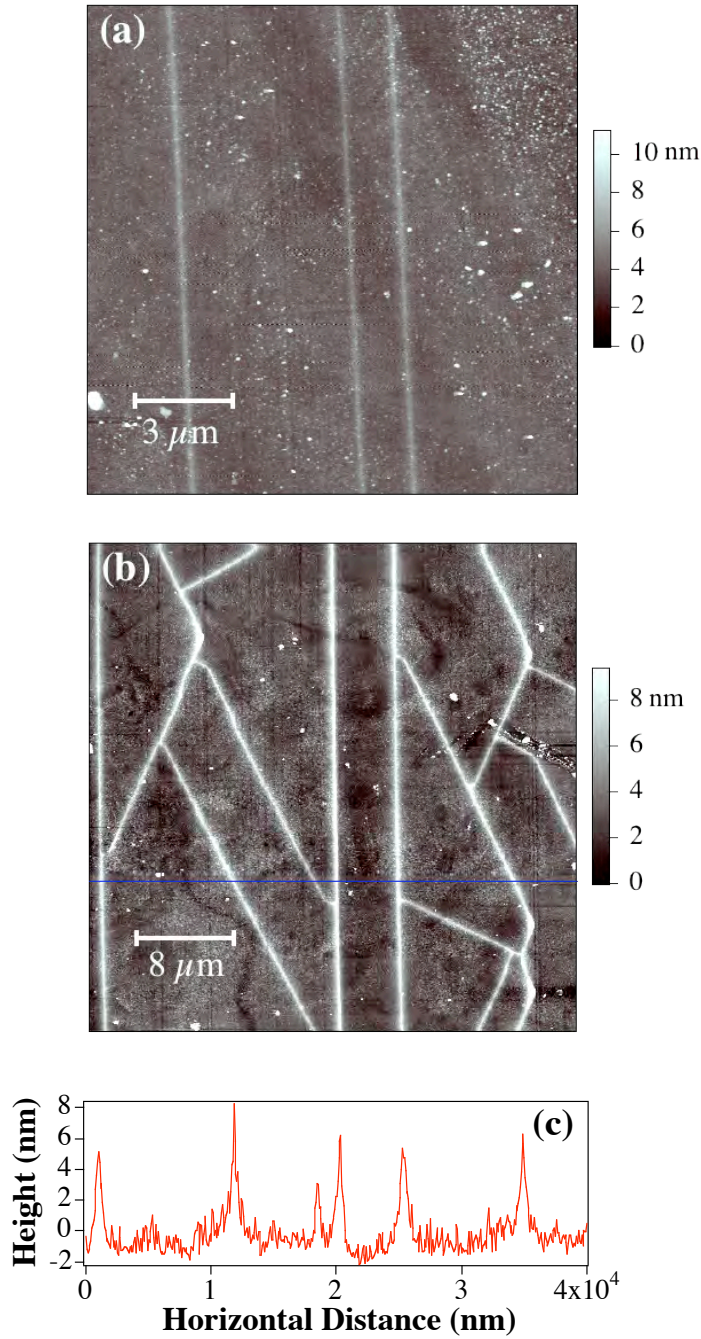
Fig. 6.12 AFM height image of (a) 500 Å and (b) 1000 Å thick films showing surface cracks; The line scan in (c) is along the longer DyScO$_3$ azimuth in which the SrTiO$_3$ film is more strained (the $\left[\bar{1}01\right]$ in-plane direction of the DyScO$_3$ substrate).
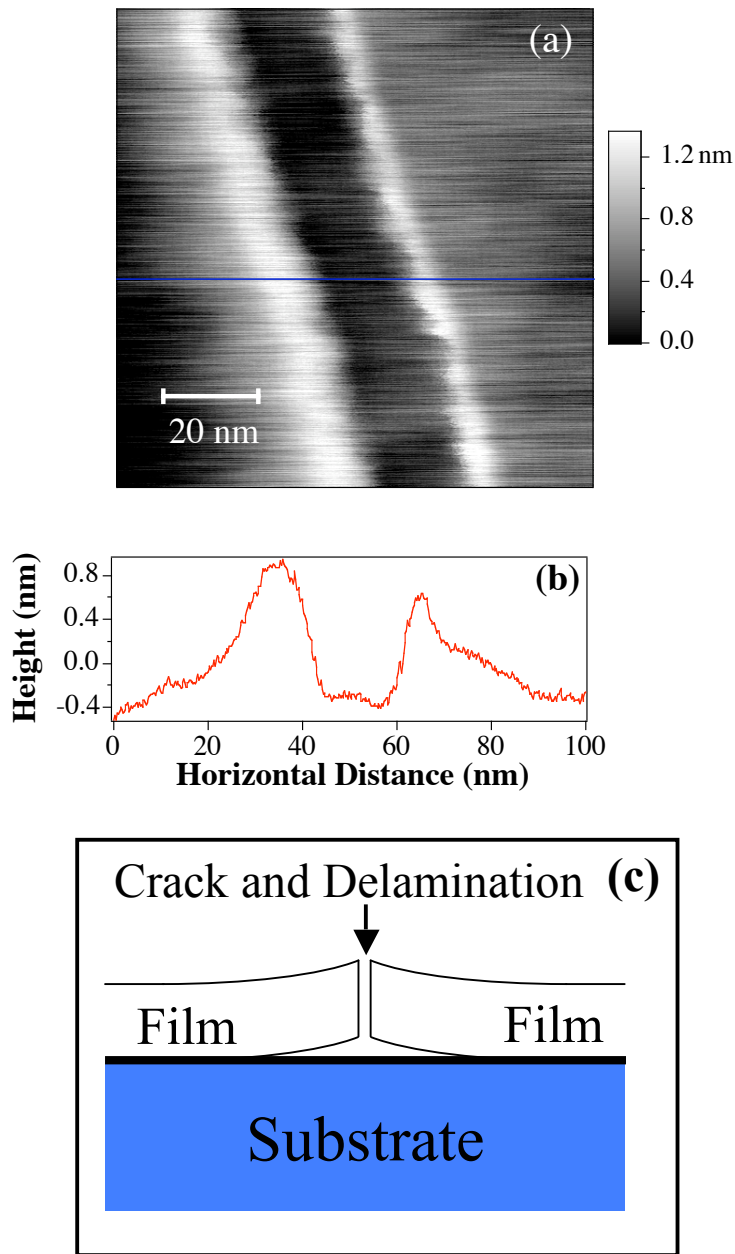
Fig. 6.13 (a) Enlarged AFM image of cracks featured in Fig. 6.12 showing that the area near the crack is above the surface of the film. (b) Line scan along the longer in-plane direction (the $[\bar{1}01]$ in-plane direction of the DyScO$_3$ substrate) showing the height of the crack region. (c) Schematic of crack and delamination necessary to explain the height of the regions near the crack.

surface diffusion.[59,60] The features of these cracks are very similar to those pictured in Fig. 6.12. However, this mechanism is usually associated with Stranski-Krastanov growth mode (or island-on-layer growth) rather than the step-flow growth observed here.[61]

In the 500 Å thick film (just above the critical thickness), the surface features are all perpendicular to the longer axis (the axis with higher strain) and aligned along the $[\bar{1}01]$ DyScO$_3$ (Fig. 6.12(a)). In the 1000 Å and 2000 Å thick films, the cracks are no longer limited to the more strained in-plane direction and appear at more random angles, though they are still mostly aligned perpendicular to the longer axis (Fig. 6.12(b)). The surface steps resulting from the movement of the dislocations form a cross hatch pattern along the [100] and [010] SrTiO$_3$ directions (Fig. 6.12(b)). Imaging of an intersection between the crack and dislocations shows that some of the dislocation lines end at the cracks and do not appear on the other side of these cracks (Fig. 6.14). This means that the cracks form during growth of the film and not during the cooling of the sample. This strongly suggests that the primary mechanism through which the films relieve stress is through cracking, not through dislocation motion.

6.5 Conclusions

MBE-grown epitaxial SrTiO$_3$ films on DyScO$_3$ have the highest reported crystal quality of any heteroepeitaxial oxide thin film (or perovskite) with rocking curves as narrow as 6.5 arc sec and extremely smooth surfaces, comparable to high quality semiconductor materials. The critical thickness at which strain was first observed in the SrTiO$_3$/(101) DyScO$_3$ system, for the MBE growth conditions, was between 350 Å and
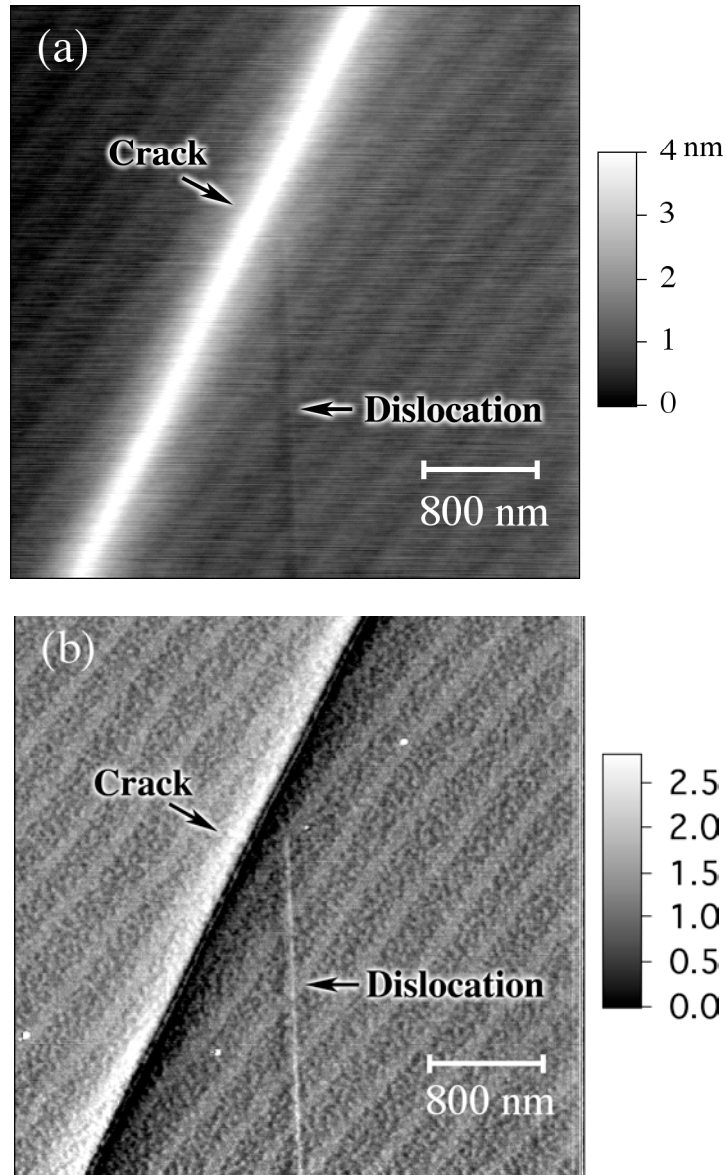
Fig. 6.14 Detailed AFM (a) height image and (b) phase image of the intersection between a crack and a dislocation line for an 800 Å thick $SrTiO_3$ film illustrating that the dislocation does not extend across the crack. Thus the cracks must appear during the growth of the film. The scan direction is along the $[\bar{1}01]$ in-plane direction of the $DyScO_3$ substrate, the longer in-plane direction

500 Å. Step flow growth was found for films above and below the critical thickness by AFM. The relaxation in this system was found to be anisotropic with almost all the relaxation in the 1000 Å thick film occurring along the longer in-plane direction. This is associated with the in-plane anisotropy in the substrate. The relaxation in these films proceeds in a manner more similar to semiconductor materials such as GaAs and $Si_{1-x}Ge_x$, rather than typical perovskite materials (that contain much higher concentrations of structural defects). The introduction of dislocations in this system appears to be difficult, resulting in the films cracking to relieve the strain energy from the epitaxial mismatch. This cracking of the film leads to raised surface features.

References

[1] G. A. Gehring and K.A. Gehring, Rep. Prog. Phys. **38,** 89 (1975).

[2] R. S. Beach, J. A. Borchers, A. Matheny, R. W. Erwin, M. B. Salamon, B. Everitt, K. Pettit, J. J. Rhyne, and C. P. Flynn, Phys. Rev. Lett. **70**, 3502 (1993).

[3] Q. Gan, R.A. Rao, C.B. Eom, J.L Garrett, and M. Lee, Appl. Phys. Lett. **72**, 978 (1998).

[4] A. F. Devonshire, Phil. Mag. Suppl. **3**, 85–130 (1954).

[5] G. A. Samara, Ferroelectr. **2**, 277 (1971).

[6] G. A. Rossetti, K. Kushida, and L. E. Cross, Appl. Phys. Lett. **59**, 2524 (1991).

[7] K. Abe, N. Yanase, K. Sano, M. Izuha, N. Fukushima, and T. Kawakubo, Integr. Ferroelectr. **21**, 197 (1998).

[8] S. K. Streiffer, J. A. Eastman, D. D. Fong, C. Thompson, A. Munkholm, M. V. Ramana Murty, O. Auciello, G. R. Bai, and G. B. Stephenson, Phys. Rev. Lett. **89**, 067601 (2002).

[9] J. H. Haeni, P. Irvin, W. Chang, R. Uecker, P. Reiche, Y. L. Li, S. Choudhury, W. Tian, M. E. Hawley, B. Craigo, A .K. Tagantsev, X. Q. Pan, S. K. Streiffer, L. Q. Chen, S. W. Kirchoefer, J. Levy, and D.G. Schlom, Nature **430**, 758 (2004).

[10] K. J. Choi, M.D. Biegalski, Y. L. Li, A. Sharan, J. Schubert, R. Uecker, P. Reiche, Y. B. Chen, X. Q. Pan, V. Gopalan, L.-Q. Chen, D. G. Schlom, and C. B. Eom, Science **306**, 1005 (2004).

[11] J. M. Lock, Proc. Roy. Soc, **A208**, 391 (1951).

[12] H. Sato and M. Naito, Physica C **274**, 221 (1997).

[13] I. Bozovic, G. Logvenov, I. Belca, B. Narimbetov, and I. Sveklo, Phys. Rev. Lett. **89**, 107001 (2002).

[14] Throughout this manuscript we use the standard setting of space group #62, *Pnma*, to describe the crystallography of $DyScO_3$. Although some authors use this setting (Ref. 15), many others use the non-standard setting *Pbnm* to describe the crystallography of $DyScO_3$ and other perovskites with the $GdFeO_3$ crystal structure (Ref. 16), The conversion from axes *a,b,c*, directions [*a b c*], or planes (*a b c*) in *Pnma* to *a′,b′,c′*, [*a′ b′ c′*], or (*a′ b′ c′*) in *Pbnm* is given by *a′=c*, *b′=a*, and *c′=b*.

[15] *International Tables for Crystallography, Vol. A: Space Group Symmetry,* 5th edition*,* edited by T. Hahn (Kluwer, Dordrecht, 2002), p. 66.

[16] *Landolt-Börnstein: Numerical Data and Functional Relationships in Science and Technology*, edited by K.-H. Hellwege and A.M. Hellwege (Springer-Verlag, Berlin, 1976), New Series, Group III, Vol. 7e, pp. 11-13.

[17] M. D. Biegalski, J. Haeni, S. K. Streiffer, V. Sherman, R. Uecker, P. Reiche, D. G. Schlom, and S. Trolier-McKinstry, (Accepted, Appl. Phys Lett.).

[18] R. Uecker and P. Reiche (unpublished).

[19] P. Reiche, B. Heroneit, and D. Schulze, Cryst. Res. Technol. **20**, 845 (1995).

[20] R. Uecker, P. Reiche, V. Alex, J. Doerschel, and R. Schalge, J. Cryst. Growth **137**, 278 (1994).

[21] CrysTec GmbH, Berlin, Germany.

[22] M. D. Biegalski, J. H Haeni, C. D. Brandle, A. J. Ven Gratis, S. Trolier-McKinstry, and D. G. Schlom, J. Mater. Sci. **20**, 952 (2005).

[23] International Products Corporation, Burlington, NJ.

[24] PM80 Headway Research Inc., Garland, TX.

[25] J.H. Haeni, C.D. Theis, and D.G. Schlom, J. Electroceram. **4**, 385 (2000).

[26] PANalytical B.V, Almelo, Netherlands.

[27] G. B. Stephenson, D. D. Fong, M. V. Ramana Murty, S. K. Streiffer, J. A. Eastman, O. Auciello, P. H. Fuoss, A. Munkholm, M. E. M. Aanerud, and C. Thompson, Physica B: Conden. Matter, **336**, 81 (2003).

[28] J. A. Eastman, P. H. Fuoss, L. E. Rehn, P. M. Baldo, G.-W. Zhou, D .D. Fong, and L. J. Thompson, Appl. Phys. Lett. **87**, 051914 (2005).

[29] JEOL Ltd., Tokyo, Japan.

[30] Veeco Metrology, LLC, Santa Barbara, CA.

[31] C. Thompson, C. M. Foster, J. A. Eastman, and G. B. Stephenson, Appl. Phys. Lett. **71**, 3516 (1997).

[32] I. K. Robinson and D. J. Tweet, Rep. Prog. Phys. **55**, 599 (1992).

[33] J. W. Matthews and A.E. Blakeslee, J. Cryst. Growth **27**, 118 (1974).

[34] H. P. Sun, W. Tian, X. Q. Pan, J. H. Haeni, and D. .G. Schlom, Appl.Phys. Lett. **84**, 3298 (2004).

[35] T. Suzuki, Y. Nishi, and M. Fujimoto, Philos. Mag. A **79**, 2461 (1999).

[36] Y. L. Zhu, X. L. Ma, D. X. Li, H. B. Lu, Z. H. Chen, and G. Z. Yang, Acta Mater. **53**, 1273 (2005).

[37] T. Matsunaga and H. Saka, Philos. Mag. Lett. **80**, 597 (2000).

[38] R. Rupprecht and M. Winter, Phys. Rev. **155**, 1019 (1967).

[39] B. Dodson and J. Tsao, Appl. Phys Lett. **51**, 1391 (1987).

[40] R. People and J. Bean, Appl. Phys. Lett. **47**, 322 (1985).

[41] *Powder Diffraction File: Sets 27 to 28*, edited by W. F. McClune, M. E. Mrose, B. Post, S. Weissmann, H. F. McMurdie, E. Evans, and W. Wong-Ng (International Centre for Diffraction Data, Swarthmore, 1986), p. 78. Card 27-220.

[42] Y. Shibata, N. Kuze, M. Matsui, M. Kanai, and T. Kawai, in *Epitaxial Oxide Thin Films II*, edited by J.S. Speck, D.K. Fork, R.M. Wolf, and T. Shiosaki, Vol. 401 (Materials Research Society, Pittsburgh, 1995), pp. 273-278.

[43] A. T. Macrander, Annu. Rev. Mater. Sci., **18**, 283 (1988).

[44] P. F. Miceli and C. J. Palmstrøm, Phys. Rev. B **51**, 5506 (1995).

[45] C. Kim, T. Spila, J. E. Greene, and I. K. Robinson, J. Appl. Phys. **83**, 7608 (1998).

[46] M. Kestigian, J. G. Dickinson, and R. Ward, J. Am. Chem. Soc. **79**, 5598 (1957).

[47] T. Ohnishi, M. Lippmaa, T. Yamamoto, S. Meguro, and H. Koinuma, Appl. Phys. Lett. **87**, 241919 (2005).

[48] R. J. Asaro and W. A. Tiller, Metall. Trans. **3**, 1789 (1972).

[49] B. J. Spensers, P. W. Voorhees, and S. H. Davis, Phys. Rev. Lett. **67**, 3696 (1991).

[50] L.B. Feund and F. Jonsdottri, J. Mech. Phys. Solids **41**, 1245 (1993).

[51] C.S. Ozkan, *Studies of morphological instabilities and defect formation in heteroepitaxial Si$_{(1-x)}$Ge$_x$ thin films via controlled annealing experiments*, Ph.D. Thesis Stanford Univ. (1997).

[52] C.-P. Liu, J. M. Gibson, T. I. Kamins, D. P. Basile, and R. S. Williams, and D. G. Cahill, Phys. Rev. Lett. **84**, 1958 (2000).

[53] A. Vailionios, B. Cho, G. Glass, P. Desjardins, D. Cahill, and J. Greene, Phys. Rev. Lett. **85**, 3672 (2000).

⁵⁴ C. W. Snyder, B. G. Orr, D. Kessler, and L. M. Sander, Phys. Rev. Lett. **66**, 3032–3035 (1991).

⁵⁵ B. G. Orr, D. Kessler, C. W. Snyder and L. Sander, Europhys. Lett. **19**, 33 (1992).

⁵⁶ H. Gao and W.D. Nix, Annu. Rev. Mater. Sci, **29**, 173 (1999).

⁵⁷ M.A. Grinfeld, Dokl. Akad. Nauk SSSR **290**, 1358 (1986) [Sov. Phys. Dokl. **31**, 831 (1986)].

⁵⁸ D.J. Srolovitz. Acta. Metall. **37**, 621 (1988).

⁵⁹ R. J. Asaro and W.A. Tiller, Metall. Trans. **3**, 1789 (1972).

⁶⁰ B. J. Spencer, P. W. Voorhees, and S. H. Davis, Phys. Rev. Lett. **67**, 3696 (1991).

⁶¹ M. A. Grinfeld and D. J. Srolovitz, "Stress Driven Morphological Instabilities and Islanding of Epitaxial Films", in *Properties of Strained and Relaxed Silicon Germanium*, ed. E. Kasper (INSPEC, IEE, 1994), pg. 3-16.

Chapter 7

Asymmetric Dielectric Properties of SrTiO$_3$ Thin Films

on DyScO$_3$ Substrates[††]

7.1 Abstract

The dielectric properties of coherent, highly strained SrTiO$_3$ thin films grown on orthorhombic (101) DyScO$_3$ substrates were examined in-plane as a function of angle. The dielectric permittivity revealed two distinct transitions along the [100] and [010] SrTiO$_3$ directions. For angles between the two principal directions, both transitions were sampled. The onset of the switchable polarization shows different critical temperatures for the [100] and [010] directions. These factors, coupled with the asymmetry in the thermal hysteresis behavior of the permittivity and the asymmetry of field cooling data confirm that these are two separate transitions with different character. The in-plane anisotropy is attributed to the non-uniform biaxial strain present in these films.

[††] Parts of this chapter appear in M. D. Biegalski, R. Uecker, P. Reiche, S. K. Streiffer, D. G. Schlom, and S. Trolier-McKinstry (submitted to Appl. Phys. Lett.)

7.2 Introduction

The onset of polarization in ferroelectric materials is accompanied by a spontaneous strain. As a result, applied strains can influence the stability of the ferroelectric phases, the transition temperature, the observed domain state and a variety of other properties. [1-,11] High strain levels have been shown to move the ferroelectric transition by hundreds of degrees, in accordance with thermodynamic theory.[6-11] The existing thermodynamic predictions for thin films assume a uniform in-plane bi-axial strain state, which is reasonable for films on cubic substrates or films with a significant level of relaxation. However, it was found that many $SrTiO_3$ films on (101) $DyScO_3$ substrates are not subject to uniform in-plane biaxial tension.[12] This discrepancy is due to the difference in the lattice constants between the $DyScO_3$ substrates used in our studies and those previously reported in the literature.[13,14] In this work the effects of the asymmetric biaxial strain state on the dielectric properties of the $SrTiO_3$ thin films are examined experimentally.

7.3 Experimental Procedure

Films of $SrTiO_3$ were grown on (101) $DyScO_3$ substrates by reactive molecular beam epitaxy (MBE) to thicknesses of 250 and 500 Å. The films were deposited using a shuttered growth technique. The stoichiometry was optimized *in-situ* using reflection high-energy electron diffraction.[12,15] The structure, including the lattice parameters of the $SrTiO_3$ thin films was characterized using a Phillips X'pert MRD four-circle diffractometer. The strain states of these films were calculated from their lattice constants using 3.905Å as the fully relaxed lattice constant of $SrTiO_3$.[16]

In order to investigate the asymmetry of the dielectric properties, interdigitated electrodes (IDT) were employed (see section 3.2). The orientation of the electric field for these electrodes is largely perpendicular to the finger length. By varying the orientation of the interdigitated electrodes, properties can be probed at various angles in the plane of the film. These IDT electrode structures were patterned photolithographically with Cr/Au using a lift-off process. The dielectric measurements were made using an HP4284a LCR meter with a Desert Cryogenics probe station and the dielectric constants were extracted using a conformal mapping technique.[13-17] The polarization switching was also measured using the same probe station with an Aixacct TF2000 ferroelectric analyzer PUND measurement with leakage compensation.

7.4 Structure and Epitaxy

The films show extremely high crystal quality with rocking curves of less than 7 arc sec (0.0019°). Due to slight variability in the $DyScO_3$ substrate lattice parameters this work will focus on two films (a 250 Å and a 500 Å thick film) though the data presented here is consistent with all samples measured. The 250 Å thick films were fully coherent with the substrate with a strain state of 1.06±0.03% along the longer in-plane direction and 1.03±0.03% along the shorter in-plane direction. The 500 Å thick films show slight structural relaxation with a strain state of 1.01±0.03 % and 0.99±0.03% for the longer and

shorter axes, respectively. Both films exhibit (001) out-of-plane oriented $SrTiO_3$ with an epitaxial relationship (100) $SrTiO_3$ || (010) $DyScO_3$ and (010) $SrTiO_3$ || ($\bar{1}$01) $DyScO_3$.[‡‡]

7.5 Dielectric Properties

7.5.1 Orientational Dependence of Dielectric Properties

Using IDT electrodes with various orientations the dielectric properties were probed along different in-plane directions. As discussed in chapter 5, the dielectric constants were dispersive below T_{max} (the temperature corresponding to the maximum permittivity). This behavior is consistent with relaxor ferroelectric behavior. The fact that dielectric dispersion appears in these films both above and below the critical thickness (see chapter 5) makes it clear that the dielectric relaxation is not a consequence of the structural relaxation.

Fig. 7.1 shows the dielectric constant at 5 kHz as a function of temperature for several angles. Intriguingly, two distinct dielectric maxima along the two principal [100] in-plane directions are observed. These two peaks appear near 260 K (labeled T_1) along the longer in-plane direction (0°) and 210 K (labeled T_2) for the shorter in-plane

---

[‡‡] Throughout this manuscript we use the standard setting of space group #62, *Pnma*, to describe the crystallography of $DyScO_3$. Although some authors use this setting,[18] many others use the non-standard setting *Pbnm* to describe the crystallography of $DyScO_3$, and other perovskites with the $GdFeO_3$ crystal structure.[16] The conversion from axes *a,b,c*, directions [*a b c*] or planes (*a b c*) in *Pnma* to *a′,b′,c′*, [*a′ b′ c′*], or (*a′ b′ c′*) in *Pbnm* is given by *a′*=*c*, *b′*=*a,* and *c′*=*b*.
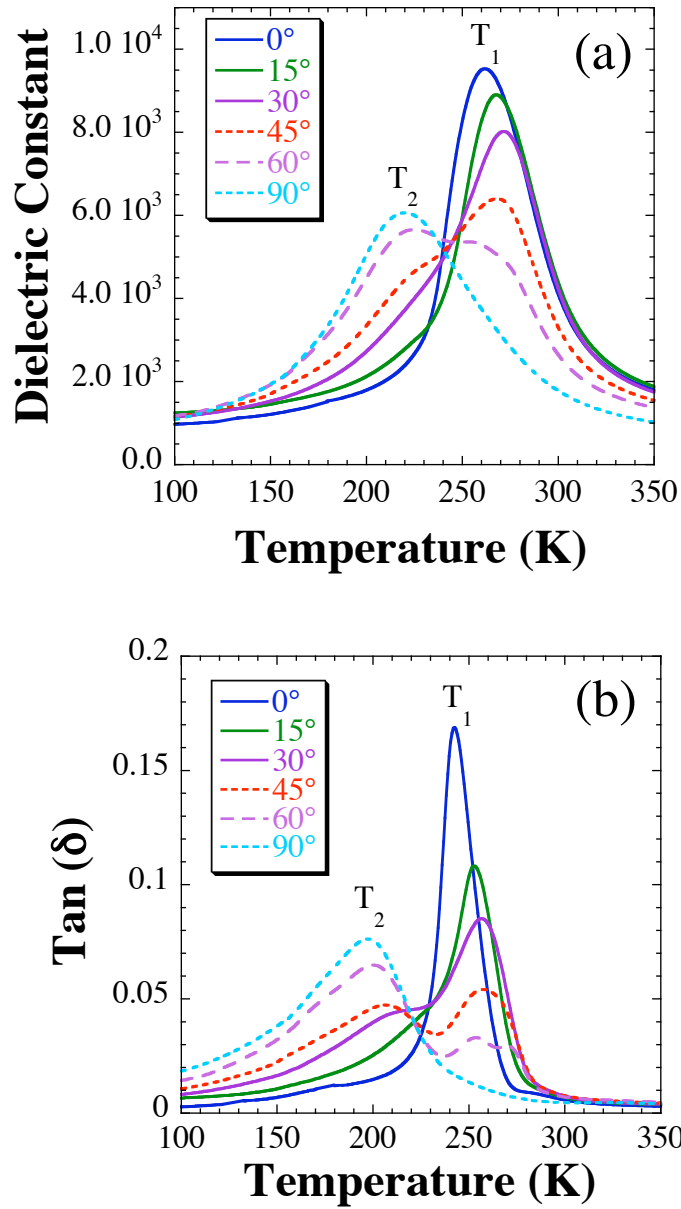
Fig. 7.1 Dielectric permittivity at 5 kHz of a 250Å thick $SrTiO_3$ thin film measured as a function of temperature for several angles showing two distinct peaks (T_1 and T_2) sampled as a function of angle. 0° is aligned with the longer [010] $SrTiO_3$ axis and 90° is aligned along the shorter [100] $SrTiO_3$.

directions (90°). Data at intermediate angles sample both peaks. Comparable behavior is observed for the dielectric loss, though the $T_{\max}$ (tan δ) are somewhat lower.

The magnitude of the permittivity, the frequency dispersion in this transition, along with the separate peaks in the loss data indicate that both peaks are ferroic in origin. Thermodynamic predictions for the case of equal in-plane tensile strains predict two phase transitions that would affect both principal in-plane orientations in the same way: a ferroelectric transition at higher temperatures with an antiferrodistortive phase transition (AFD) corresponding to the 105 K transition in bulk $SrTiO_3$ at lower temperatures. The antiferrodistortive transition entails a rotation of the TiO_6 octahedra and typically does not have a strong signature in the dielectric properties.[20]

To further probe the nature of T_1 and T_2, the switchable polarization was measured as a function of temperature for the two principal axes (see Fig. 7.2). It is clear that the onset of reversible polarization occurs at two different temperatures along the two principal in-plane directions. The shorter in-plane axis develops a switchable polarization ~40 K below the onset of polarization along the longer axis. Thus, both T_1 and T_2 are ferroelectric in origin. The fact that a switchable polarization develops at different temperatures along the principal in-plane directions and that there are two observed $T_{\max}$ as a function of angle suggests that T_1 corresponds to the development of a ferroelectric phase with the polarization parallel (or nearly so) to the long axis in this fully coherent film. T_2 would then correspond to a ferroelectric-ferroelectric phase transition in which either the polarization rotates away from the longer axis or one in which an independent polarization component develops along the shorter axis.
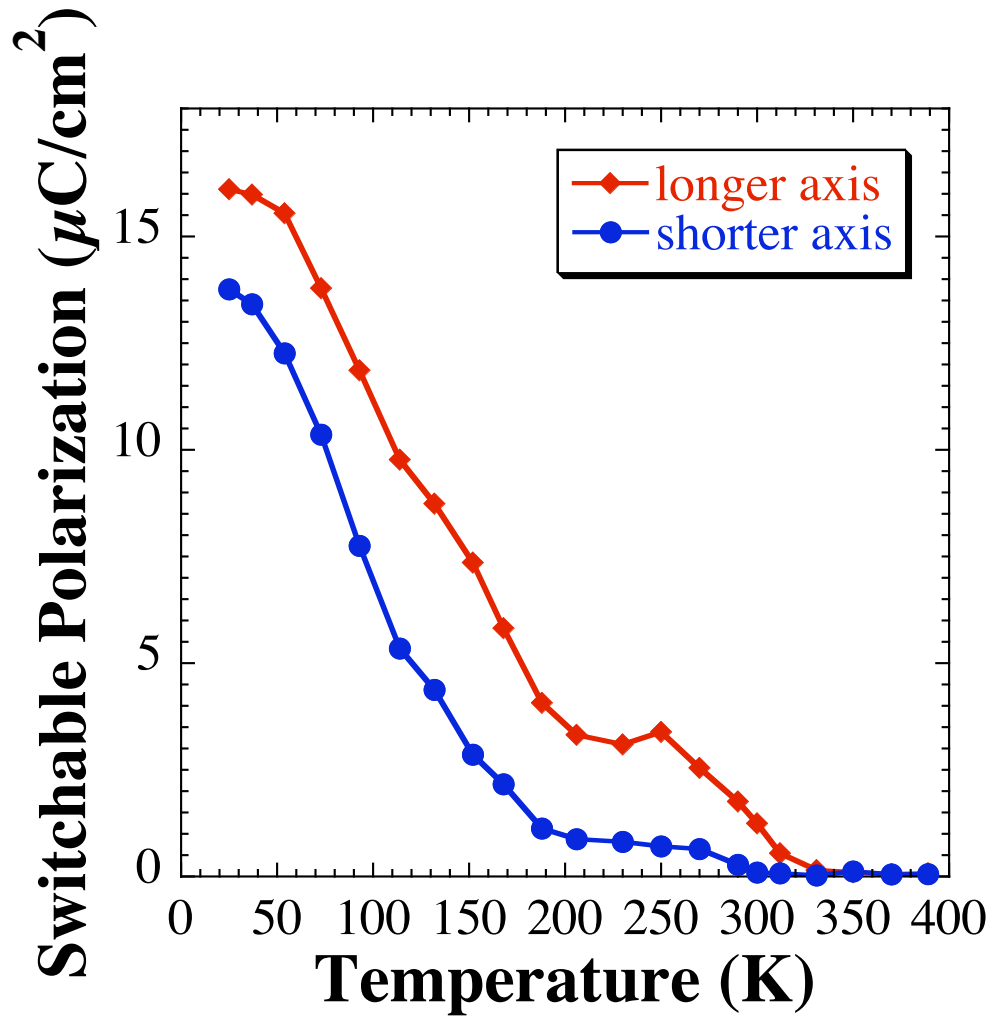
Fig. 7.2 Switchable polarization as a function of temperature for the two principal in-plane directions of the 250 Å thick $SrTiO_3$ film on (101) $DyScO_3$.

To examine this in more depth, the dependence of the switchable polarization as a function of orientation was studied at 70 K, where both principal axes are ferroelectric (see Fig. 7.3). A peak in the switchable polarization appears approximately 45° away from either principal axis. This is clearly inconsistent with <100> as the polar axis if complete a_1-a_2 in-plane switching is allowed. Such a scenario should have maxima in the switchable polarization at 0° and 90° with a minima near 45°. Thus, other possibilities were considered. Fig. 7.3 compares the experimentally measured dependence of the switchable polarization to two models. One model assumes that the polar direction is parallel to <100>, but with two different polarizations along [100] and [010]. In this case, to get the polarization maxima near 45° it was assumed that the volume fractions of a_1 and a_2 domains were equal and that little a_1-a_2 switching is possible. The polarization components along the two principal in-plane directions are taken from the experimental data. The other model assumes that the polarization at low temperatures is along <110> and that a_1-a_2 switching is possible. Again the polarization along [110] is taken from the experimental data. As can be seen in Fig. 7.3, both models describe the angular dependence of the switchable polarization equally well. Second harmonic generation measurements on partially relaxed $SrTiO_3$ films on $DyScO_3$, where the strain state is approximately uniform in-plane ($\varepsilon_{100} = 0.93\pm 0.02$ % and $\varepsilon_{010} = 0.95\pm 0.02$ %), suggest that the polarization was parallel to the <110>.[10] Comparable measurements need to be performed on coherent films, where the strains state is not uniform in-plane.

Chang *et al.*[21] also reported a difference in T_{max} between the two principal in-plane axes for $SrTiO_3$ thin films on $DyScO_3$, though only a ~5 K difference was observed
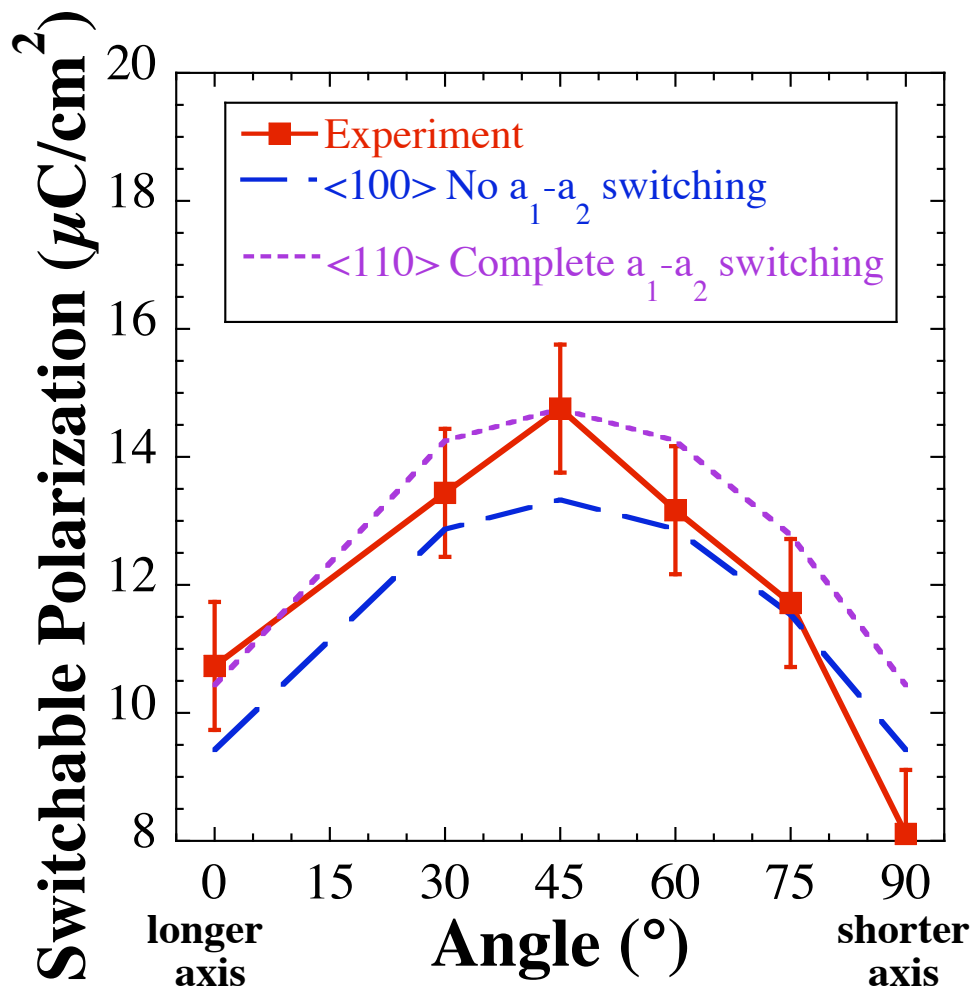
Fig. 7.3 Switchable polarization measured as a function of angle from the longer axis at 70 K for a 250 Å thick SrTiO₃ film. The experimental data (■) is show with the solid line and the models are shown with dashed lines.

in that work. The discrepancy can be attributed to two factors. First, the initial batch of

DyScO$_3$ substrates on which their film was grown was observed to have a small

percentage of twins. This would complicate any determination of orientational

dependence. Second, the structural quality of the initial DyScO$_3$ substrates is much lower

than that of the substrates used in this study. The films on the early crystals have rocking

curve widths of 0.04° (as described in reference 21), whereas the rocking curve widths

here were 0.0019 ° and 0.0018° for the 500 and 250 Å films respectively. Given the pre-

existing defects, it is not surprising that the stain state of the films in reference 21 would

be closer to thermodynamic equilibrium. For films thicker than the critical thickness

(~100 Å by Matthews Blakeslee criterion[22]) films on defective substrates should be more

relaxed.[23] In general, it is observed that the strain along the longer axis relaxes more

rapidly than the strain in the shorter in-plane direction. Haeni *et al.*[8] and Chang *et al.*[21]

report homogeneous strains states for their SrTiO$_3$ films. The asymmetry between the two

<100> in-plane lattice parameters was determined to be 0.0005±0.0004 Å for the 500 Å

thick film in references 8 and 21. However, the 500 Å thick film examined in this work

has an asymmetry of 0.0014±0.0004 Å. The asymmetry of the dielectric tunability

reported by Chang *et al.*[21] is consistent with a lower dielectric maximum along the

shorter in-plane direction, since tunability is generally higher near the peak permittivity.

Ba$_{0.60}$Sr$_{0.40}$TiO$_3$[24] and Pb$_{0.35}$Sr$_{0.65}$TiO$_3$ on (101) NdGaO$_3$ (isostructural to DyScO$_3$) have

also been shown to posses asymmetry in the dielectric properties. [25]

7.5.2 Evidence for Three Transitions

The temperature dependence of the real part of the dielectric constant of $\varepsilon'(T)$

shows considerable thermal hysteresis (Fig. 7.4). On zero-field cooling (ZFC) below
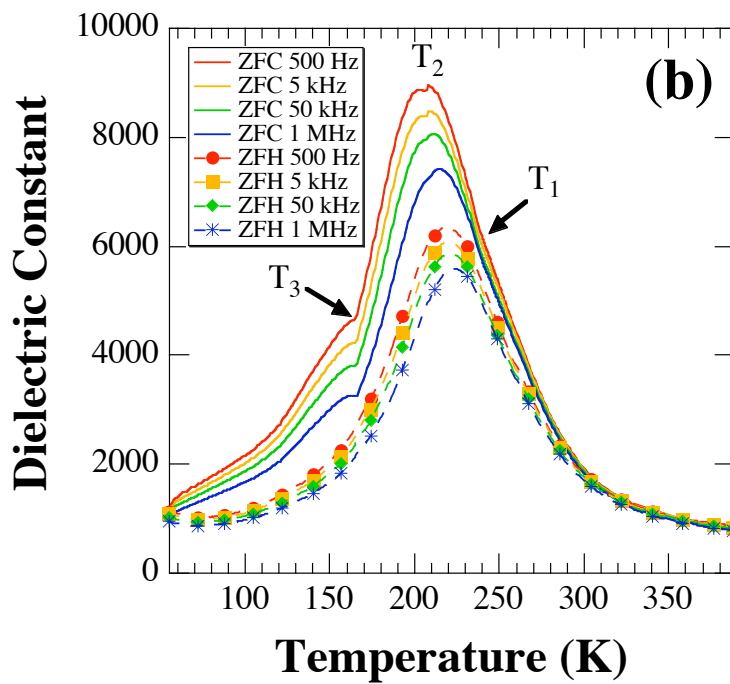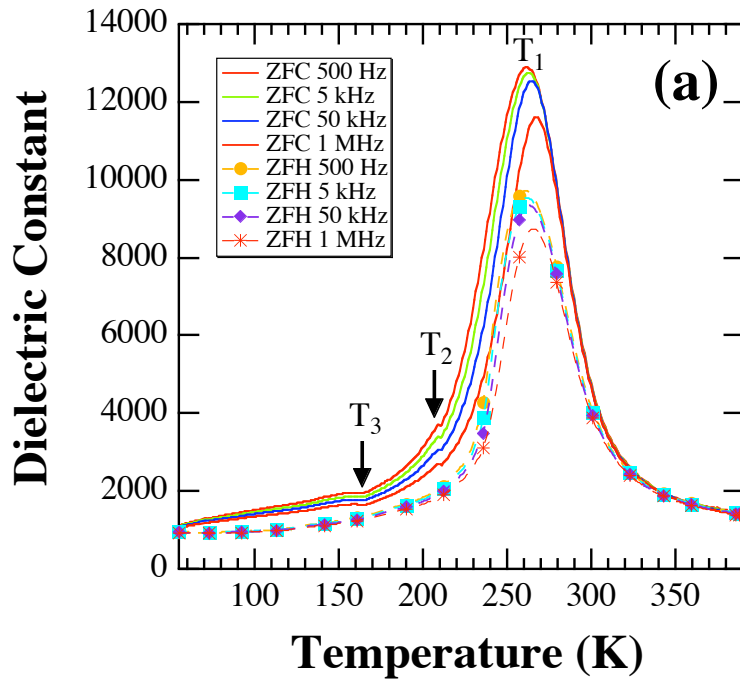
Fig. 7.4 Dielectric constant of 250Å thick film measured on heating and cooling for longer in-plane direction (a) and shorter in-plane direction (b) showing signatures of three transitions in both principal directions.

T_{max}, the SrTiO$_3$ shows much more frequency dispersion in the permittivity and a larger dielectric constant than when measured on zero-field heating (ZFH). This suggests that these SrTiO$_3$ films spontaneously develop (at least partially) a ferroelectric macrodomain state at low temperatures. The result of the appearance of a more normal ferroelectric state is reduced dielectric dispersion, a reduced magnitude of the permittivity, and a shift of the peak in the permittivity to slightly higher temperatures, all of which are present in Fig. 7.4. The spontaneous development of a normal ferroelectric state without the application of a dc bias field does not occur in all relaxors, but has been previously reported for lead scandium tantalate ceramics with low point defect concentrations.[26] It is also reasonable that the permittivity data for ZFC and ZFH converge above T_{max} where the ferroelectric phase is destabilized.

From Fig. 7.4 it can be seen that there are dielectric anomalies for measurements along both in-plane <100> directions. This indicates that all the transitions occur regardless of the direction of the small signal electric field implemented in the measurement. This is contrary to the theory suggested by Chang *et al.*,[21] that the differences in T_{max} for the two orthogonal in-plane axis is due to the coupling of the electric field used in the measurement to a x_6 shear tensor. Their theory predicts only a 5 K difference in transition temperature and can could not explain the ~40 K splitting observed in our data.

The permittivity data also has a third anomaly at 165 K (labeled T$_3$) that is present in measurements along both in-plane orthogonal directions. Unlike the transitions at T$_1$ and T$_2$, the transition at T$_3$ shows a relatively small signature in the permittivities. This feature may correspond to the antiferrodistortive transition, predicted by

thermodynamics to be between 120 and 175 K for an average strain state like that shown by these films.[7,10] Additional structural confirmation of this should be undertaken.

7.5.3 Relaxor Nature of Transitions

The dielectric relaxor behavior along the two directions also exhibits an asymmetry. To compare the relaxor behavior of the two principal in-plane directions, the power relation described by Martirena and Burfoot was used to fit the permittivity data above T_{max}:[27]

$$\frac{1}{\varepsilon(T)} = \frac{1}{\varepsilon_{max}} \left[1 + \frac{[T - T_{max}]^{\gamma}}{2\delta^2} \right]$$

Eq. 7.1

where ε_{max} is the maximum real permittivity, T_{max} is the temperature at which ε_{max} occurs and γ and δ are fitting constants that describe the relaxor behavior. γ is a measure which describes to which degree of a relaxor ferroelectric character; for $\gamma = 1$, Eq. 1.1 simplifies to the Curie-Weiss law for normal ferroelectrics, and for $\gamma = 2$, Eq. 7.1 becomes the quadratic relation given by Smolensky[28] for ferroelectric relaxors. Thus the closer γ is to 2 the more "relaxor character" the transition has. Fig. 7.4 shows data taken during cooling. For the transition measured along the larger in-plane direction, the fit to Eq. 7.1 yields $\gamma = 2.00\pm0.03$, while $\gamma = 1.78\pm0.03$ for the shorter in-plane axis. Somewhat smaller differences in γ values were observed in other films. However, in all cases more relaxor character was observed along the long axis.

This anisotropy of the relaxor character is also present in the field cooling data (Fig. 7.5). The samples were cooled under an applied DC bias of 3 kV/cm (FC) and the permittivity was measured on heating (ZFH after FC). Upon heating, the dielectric
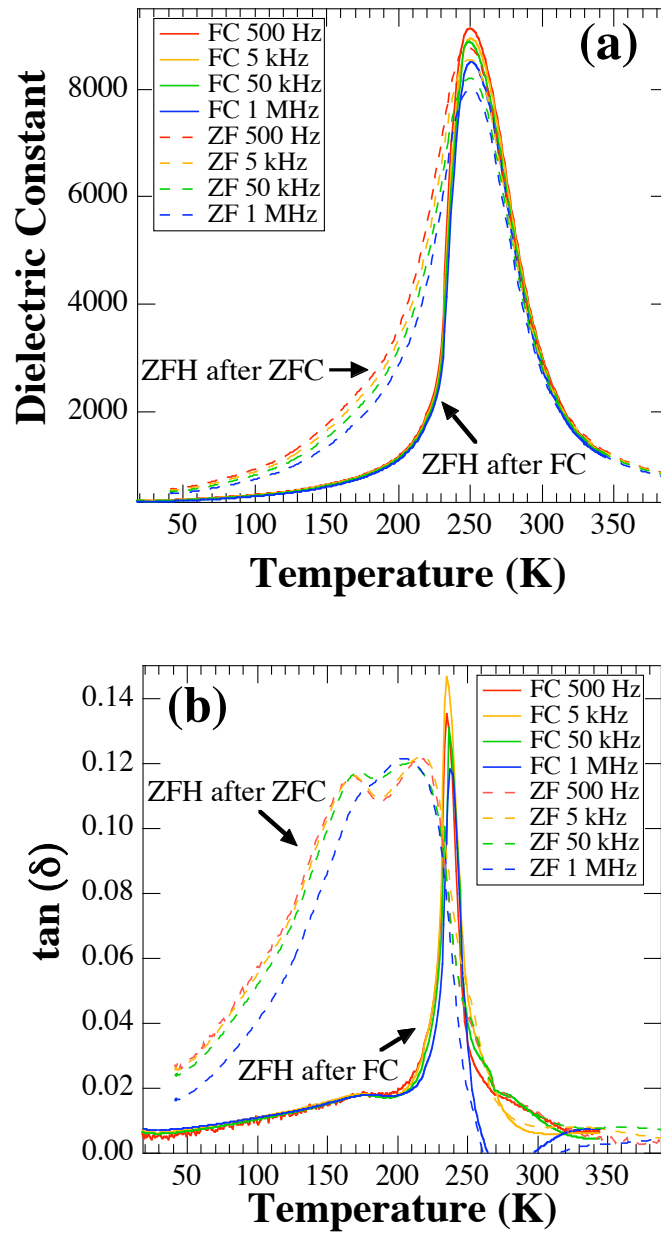
Fig. 7.5 (a) Dielectric constant and (b) loss for 500 Å thick film measured along the shorter in-plane axis on heating films cooled without dc bias (ZF-zero field) represented by dashed lines and under 3 kV/cm dc bias (FC-field cooled) represented by solid lines. All the frequencies collapse above after field cooling indicating a more normal ferroelectric state.

constant shows less frequency dispersion and a slightly higher transition temperature as shown in Fig. 7.5(a) and Fig. 7.6(a). This indicates that a macrodomain state is induced, which is typical for relaxor materials. Measurements of the field cooled sample along the shorter axis show the sharpest peak in the loss data observed (Fig. 7.5(b)). This is coupled with a collapse of the frequency dependence. The ability to stabilize a more normal ferroelectric state along the shorter in-plane is consistent with the measured γ's showing a stronger relaxor character along the longer in-plane direction.

7.6 Conclusions

In summary, asymmetrically strained $SrTiO_3$ shows two distinct permittivity maxima along the $SrTiO_3$ [100] and [010] directions. Both transitions are sampled at intermediate angles. Measurements of the switchable polarization as a function of temperature, relaxor character and permittivity after field cooling confirm that that these two transitions are distinct and are not an artifact of the electric field direction during the measurement as has previously been proposed.[21] A smaller dielectric signature that may correspond to the antiferrodistortive transition near 165 K has been observed along both axes. New theoretical predictions accounting for the non-uniform in-plane strain state present in these films are needed.
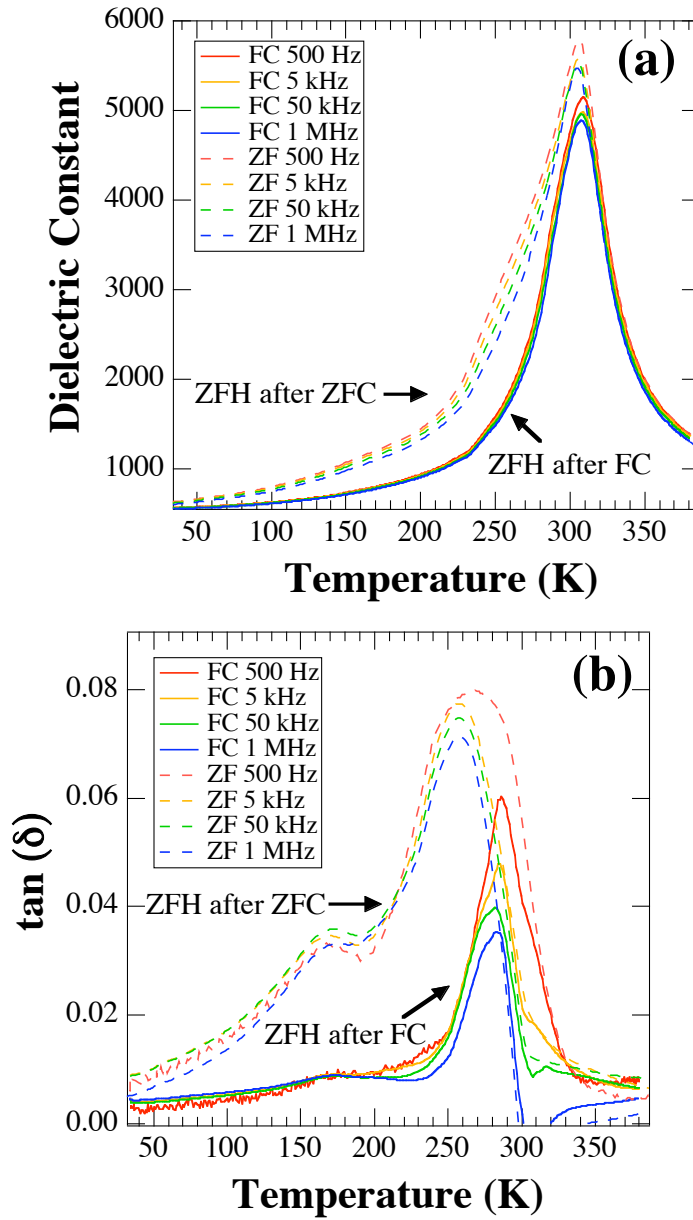
Fig. 7.6 Dielectric constant (a) and loss data (b) measured along the longer axis on heating for a 500 Å thick film cooled without dc bias (ZF-zero field) shown as dashes and under 3 kV/cm dc bias (FC-field cooled) represented by solid lines. There is much less frequency dispersion in the measurement after field cooling indicating a more normal ferroelectric transition

References

---

[1] A. F. Devonshire, Phil. Mag Suppl. **3**, 85–130 (1954).

[2] D. Bancroft, Phys. Rev. **53**, 587 (1938).

[3] G. A. Samara, Ferroelectr. **2**, 277 (1971).

[4] G. A. Rossetti, K. Kushida, and L. E. Cross, Appl. Phys. Lett. **59**, 2524 (1991).

[5] K. Abe, N. Yanase, K. Sano, M. Izuha, N. Fukushima, and T. Kawakubo, Integr. Ferroelectr. **21**, 197 (1998).

[6] S. K. Streiffer, J. A. Eastman, D. D. Fong, C. Thompson, A. Munkholm, M. V. Ramana Murty, O. Auciello, G. R. Bai, and G. B. Stephenson, Phys. Rev. Lett. **89**, 067601 (2002).

[7] N. A. Pertsev, A. K. Tagantsev, and N. Setter, Phys. Rev. B **61**, R825 (2000); **65**, 219901(E) (2002).

[8] J. H. Haeni, P. Irvin, W. Chang, R. Uecker, P. Reiche, Y. L. Li, S. Choudhury, W. Tian, M. E. Hawley, B. Craigo, A. K. Tagantsev, X. Q. Pan, S. K. Streiffer, L. Q. Chen, S. W. Kirchoefer, J. Levy, and D. G. Schlom, Nature **430**, 758 (2004).

[9] N. A. Pertsev, A. G. Zembilgotov, and A. K. Tagantsev, Phys. Rev. Lett. **80**, 1988 (1998).

[10] Y. L. Li, S. Choudhury, J. H. Haeni, M. D. Biegalski, A. Vasudevarao, A. Sharan, H. Z. Ma, J. Levy, V. Gopalan, S. Trolier-McKinstry, D. G. Schlom, and L. Q. Chen (unpublished).

[11] K. J. Choi, M. D. Biegalski, Y. L. Li, A. Sharan, J. Schubert, R. Uecker, P. Reiche, Y. B. Chen, X. Q. Pan, V. Gopalan, L.-Q. Chen, D. G. Schlom, and C. B. Eom, Science **306**, 1005 (2004).

[12] M. D. Biegalski, D. D. Fong, J. A. Eastman, P. H. Fuoss, R. Uecker, P. Reiche, W. Tian, X. Q. Pan, M. E. Hawley, S. K. Streiffer, S. Trolier-McKinstry, and D. G. Schlom (unpublished).

[13] M.D. Biegalski, J.H Haeni, C.D. Brandle, A.J. Ven Gratis, S. Trolier-McKinstry, and D. G. Schlom, J. Mater. Sci **20**, 952 (2005).

[14] R. P. Liferovich and R. H. Mitchell, J. Solid State Chem. **177**, 2188 (2004).

[15] C. D. Theis and D. G. Schlom, J. Vac. Sci. Technol. A **14**, 2677 (1996).

[16] *Thermophysical Properties of Matter Vol. 13: Thermal Expansion of Nonmetallic Solids*, edited by Y. S. Touloukian, R. K. Kirby, R. E. Taylor, and T. Y .R. Lee (Plenum, New York, 1977), p. 288.

[17] O. G. Vendik, S. P. Zubko and M. A. Nikolskii, Zh. Tekh. Fiz. **69**, 1 (1999) [Sov. Phys. Tech. Phys. **44**, 349 (1999)].

[18] *International Tables for Crystallography, Vol. A: Space Group Symmetry,* 5th edition*, edited by T. Hahn (Kluwer, Dordrecht, 2002), p. 66.

[19] *Landolt-Börnstein: Numerical Data and Functional Relationships in Science and Technology*, edited by K.-H. Hellwege and A.M. Hellwege (Springer-Verlag, Berlin, 1976), New Series, Group III, Vol. 7e, pp. 11-13.

[20] K. A. Müller and H. Bukard, Phys. Rev. B **19**, 3593 (1979).

[21] W. Chang, S. W. Kirchoeffer, J. A. Bellotti, S. B. Qadri, J. H. Haeni, D. G. Schlom, and J. M. Pond, J. Appl. Phys. **98**, 024107 (2005).

[22] J. W. Matthews and A. E. Blakeslee, J. Cryst. Growth **27**, 118 (1974).

[23] L. B. Freund and S. Suresh *Thin Films Materials: Stress, Defect Formation and Surface Evolution*, (Cambridge University Press, Cambridge, 2003) pp. 464-488.

[24] W. K. Simon, E. K. Akdogan, J. A. Bellotti, and A. Safari, Appl. Phys. Lett **87**, 082906 (2005).

[25] Y. Lin, X. Chen, S. W. Liu, C. L. Chen, J.-S. Lee, Y. Li, Q. Q. Jia and A. Bhalla, Appl. Phys. Lett. **84**, 577 (2004).

[26] F. Chu, I. Reaney, and N. Setter, J. Appl. Phys. **77**, 1671 (1995)

[27] H. T. Martirena and J. C. Burfoot, Ferroelectrics **7**, 151 (1974).

[28] G. A. Smolensky, J. Phys. Soc. Jpn. Suppl. **28**, 26 (1970).

Chapter 8

Conclusions and Future Work

8.1 Conclusions

8.1.1 DyScO$_3$ and GdScO$_3$ Substrates

The first step in this work was to examine the rare earth substrates DyScO$_3$ and GdScO$_3$. These materials have the GdFeO$_3$ structure, a derivative of the prototype perovskite crystal structure. In this crystal structure the small A site ion leads to rotation of the ScO$_6$ octahedra.[1] The room temperature lattice constants of these materials were found to be a=5.720±0.003 Å, b=7.890±0.003 Å, and c=5.442±0.003 Å for DyScO$_3$ and a=5.755±0.003 Å, b=7.936±0.003 Å, and c=5.489±0.003 Å for GdScO$_3$. This leads to pseudo cubic lattice constants on the (101) plane of 3.9450 and 3.9475 for DyScO$_3$ and 3.976 and 3.697 Å for GdScO$_3$, indicating that these substrates are well lattice matched to SrTiO$_3$ which has a lattice constant of 3.905 Å.[2]

The thermal expansion of these materials was measured and found to be 8.4 ppm/K and 10.9 ppm/K on average for DyScO$_3$ and GdScO$_3$, respectively. This matches the thermal expansion of most perovskite materials which generally have thermal expansions near ~10 ppm/K (SrTiO$_3$ = 9.4 ppm/K). Thus, the substrates will allow for the growth of epitaxial thin films of most perovskite materials.[3] The high temperature x-ray data also revealed that there was no structural transition up to 1200 K for both DyScO$_3$ and GdScO$_3$. This is important because a structural transition in the substrate could

induce large strains, inducing cracking and often delamination of epitaxial thin films. The dielectric properties of these materials were probed as a function of temperature to examine if there were any anomalies or phase transitions between 4 and 450 K. $DyScO_3$ shows a dielectric constant of 19 to 36 depending on orientation with very little temperature dependence. $GdScO_3$ yielded similar results with a dielectric constant of 19 to 32. Both materials show no anomalies, losses less than 0.1% over the whole temperature range and very little temperature dependence of the permittivity (TCC < 0.004 K^{-1}). Thus the measurements of electrical properties for films grown on top of $GdScO_3$ and $DyScO_3$ will not be strongly influenced by artifacts induced by the substrates. That is, interdigitated electrodes can be used measure the dielectric properties of films on these substrates.

The thermal expansion, dielectric properties and, particularly, the lattice match make $DyScO_3$ and $GdScO_3$ very good substrates for the epitaxial growth of $SrTiO_3$ and other perovskite materials.

8.1.2 Dielectric Properties of Strained $SrTiO_3$

The dielectric properties of epitaxially strained $SrTiO_3$ were explored as a function of temperature. These materials show a maximum permittivity of approximately 20,000 near 260 K. Hystereisis develops around 260 K with a remanent polarization of 10 $\mu C/cm^2$ at 77 K. This confirms that the $SrTiO_3$ transforms to a ferroelectric state near 260 K as predicted by thermodynamic theory. However, the dielectric peaks show considerable frequency dependence. This frequency dependence of the loss data was well described by the Vogel-Fulcher equation. This means that the material is not a normal ferroelectric as predicted by phenomenology but is instead a relaxor ferroelectric.

The source of this relaxor ferroelectricy was explored: anomalous behavior of the substrate, small coherency length in the film, inhomogeneous strain, and point defects. The substrates show no dielectric anomalies over the temperature range explored, no signs of ferroelectric behavior, and no structural changes. These facts make it impossible for the substrate to directly induce the relaxor behavior observed for the $SrTiO_3$ thin films.

The possibility of a small coherence length causing relaxor behavior was considered. A small coherence length can lead to the breaking of the long range order that is needed to obtain normal ferroelectric behavior.[4] It was found that rocking curves in-plane are as narrow as the out-of plane rocking curves (FWHM~0.008°). Since the rocking curve is directly proportional to the quality of the long range ordering, this very narrow rocking curve means that the in-plane ordering is very high, and so is unlikely to induce relaxor ferroelectric behavior.

Inhomogeneous strain in the films may also cause relaxor behavior, since most of the films examined were larger than the critical thickness and have misfit dislocations. These dislocations could lead to a range of strains in the material and induce the relaxor ferroelectric behavior. To examine these effects, films with thicknesses below the critical thickness were studied; these films are completely coherent and avoid the inhomogeneous strain state. These films were also found to exhibit the frequency dependence of the dielectric constant characteristic of the relaxor behavior. Thus the relaxor behavior cannot be attributed to inhomogeneous strains.

Point defects have also been found to induce relaxor behavior in many materials. It was found that there was diffusion of the scandium into the film from the substrate.

This scandium concentration was correlated with the amount of dielectric relaxation in the materials. Other sources of point defects may also contribute. To examine the effects of strain a 250 Å thick $SrTiO_3$ film was grown on $GdScO_3$, with a ~50% greater strain than $SrTiO_3$/$DyScO_3$. This film exhibited the same character as the films on $DyScO_3$ except the a T_{max} at ~350 K, indicating that strain is a dominate factor in shifting the T_{max}. Thus, for these systems it was found that the ferroelectric transition was shifted to near room temperature due to strain, and the dielectric relaxation is most likely due to Sc diffusion from the substrate into the film.

8.1.3 Structural Relaxation of $SrTiO_3$ Films on $DyScO_3$ Substrates

The structures of the $SrTiO_3$ films were found to be extremely high quality. X-ray diffraction showed that these films have the narrowest rocking curve of any heteroepitaxial oxide thin film, with rocking curve widths of 6.5 arc sec (0.0018°), indicating the structural perfection of these films. It should be noted that this measurement is at the limit of the instrument used and of most conventional diffraction equipment. Compared to the best bulk single crystal of $SrTiO_3$ the rocking curves of the films are over an order of magnitude narrower, and the quality is far superior to commercially available single crystals. These films also exhibit extremely smooth surfaces as evidenced by a surface roughness of 2.6 Å and thickness oscillations appearing far from the Bragg diffraction peak. Typically this structural quality is only found in very high grade semiconductor materials, not complex oxide materials.

The critical thickness of $SrTiO_3$ thin films grown on (101) $DyScO_3$ was found to be between 350 Å and 500 Å. This was confirmed by reflection high energy electron diffraction (RHEED) measurements made during growth. The RHEED measurements

showed a broadening of the 1st order diffraction rods between 180Å and 450Å indicating the onset of structural relaxation.

By using X-ray diffraction it was found that for film thicknesses greater than 500 Å there were shoulders in the in-plane diffraction peaks and a broad base in the rocking curves that were not present in films 350 Å thick and thinner. This indicates the onset of structural relaxation between 350 Å and 500 Å. The rate at which the structural relaxation occurred was much slower than the typical logarithmic dependence on the film thickness, indicating that it is very difficult to introduce dislocations into the system. Thus, 1100 Å thick films were found to be ~90% coherent on the highest quality substrates. This structural relaxation was also found to be asymmetric with most of the relaxation occurring along the longer in-plane direction.

AFM was also used to examine the structural relaxation. For films 350 Å thick and thinner there were no pronounced surface features, only ~4 Å steps that correlate to unit cell high steps and an RMS roughness of 2.6 Å. This indicates that the films grow in a step flow regime and are extremely smooth. The 500 Å thick films show cracks on these surfaces that are all aligned perpendicular to the longer in-plane direction, indicating that all the relaxation is perpendicular to the longer in-plane direction. The 1000 Å thick film shows more irregular cracking, indicating that the structural relaxation is along both the in-plane directions. However, the majority of the strain relaxation still appears to be along the longer in-plane direction. Though some dislocation lines were visible in the material, the strain in the material appears to reduce by cracking instead of by the introduction of misfit dislocations. This was confirmed by the presence of dislocation lines ending at cracks, which means that the cracking occurred during growth

and not during cooling. These cracks also had the unusual feature of appearing above the surface of the film. This was due to the fact that strained $SrTiO_3$ has a smaller lattice constant than the unrelaxed $SrTiO_3$. Thus when the strain is relaxed it causes the material to expand in the out of plane direction and appear above the surface. However, to account for the full height of the surface features the films must also delaminate near the crack edges.

Since the $SrTiO_3$ films are typically annealed to reduce the oxygen vacancy concentration, the effects of a thermal anneal at 700 °C on the structural relation were examined. It was found that the reoxidation in these films had little effect on the lattice parameters of the films. For films thicker than the critical thickness there was a slight increase in the structural relaxation. For films below the critical thickness, no change in the structural relaxation was observed. This was expected since the amount of relaxation in the system is most likely kinetically limited at these growth temperatures.

Using RHEED, XRD and AFM the critical thickness at which strain begins to be relieved in the $SrTiO_3$-(101) $DyScO_3$ system was found to be ~400Å. This strain relaxation occurs mostly along the longer in-plane direction. The rate of strain relaxation is much slower than the typical logarithmic dependence (on film thickness) as described by thermodynamic theory. This is explained by the difficulty in introducing misfit dislocations in the films that is evidenced by the cracking of the films at growth temperature. These $SrTiO_3$ thin films were found to have extremely high structural quality with the narrowest rocking curves of any heteroepeitaxial oxide thin film. This accompanied by the extremely smooth film surface puts these complex oxide materials

into the same structural quality as most high-grade semiconductor materials for the first time.

8.1.4 Asymmetry of In-Plane Dielectric Properties

The asymmetry of the relaxation indicated that the strain state was not equal in both in-plane directions for the strained $SrTiO_3$, as previously assumed. The dielectric properties of the strained $SrTiO_3$ were probed using interdigitated electrodes with different orientations. By changing the orientation of the electrodes the orientation of the electric field was changed and the properties could be mapped. The dielectric data showed that there were two distinct transitions, along the [100] and [010] $SrTiO_3$ directions of the film. These two transitions were sampled as a function of angle as the field was changed from [100] and [010]. The presence of two distinct in-plane transitions was confirmed by the onset of switchable polarization at two different temperatures for the two principal axes. The degree of relaxor behavior was also found to be higher along the longer in-plane direction. Field cooling along the longer in-plane direction shifted the transition temperature to slightly higher temperatures and reduced the frequency dependence, consistent with the induction of a stable ferroelectric domain structure. Field cooling along the shorter in-plane direction yielded similar results, but the relaxor character was almost completely suppressed with almost no frequency dependence in the dielectric constant data. The most significant change was in the loss data where there was a change from a broad peak to a very sharp peak. The observed asymmetry is not correctly described by existing thermodynamic models

8.2 Future Work

Future work in this topic can be broken into three main thrusts: measurement of structural transitions in $SrTiO_3$; the role of Sc in the relaxor behavior; and effects of strains on the electronic properties.

From the dielectric data it has become clear that there is more than one transition in this strained $SrTiO_3$. The structural origins of these transitions need to be studied. A combination of neutron diffraction and x-ray diffraction as a function of temperature, would allow a complete determination of the positions of all the atoms in the unit cell. Neutron diffraction data is important since it is the only way to measure the positions of the oxygen atoms in $SrTiO_3$. Typically very thick samples are mandated due to the small cross section for neutrons. However, the new high flux Spalation source at Oak Ridge National Laboratory will have high enough intensity to measure even thin films. This data coupled with high-resolution x-ray data will enable a complete determination of the symmetry of the system and the structural changes. The data can also be used to determine the position of atoms in the unit cell with high precision. This can directly determine the polarization directions in the unit cell and the onset of the antiferrodistortive transition (AFD). This would clear up the role of strain states in moving the AFD transition and the effects of asymmetry.

These neutron and x-ray diffraction techniques could also be employed to determine the electrostrictive coefficients of $SrTiO_3$. It has been shown that there is a wide spread in the reported values for the electrostrictive coefficients of $SrTiO_3$.[5] This leads to large error bars on the possible transition temperatures by phenomological modeling. Through application electric fields on a single crystal of $SrTiO_3$ and

determining the strain state though these diffraction techniques the electrostrictive coefficients could be directly measured.[6] This would dramatically improve the abilities of phenomology theory to predict the phase transitions in $SrTiO_3$.

The exact role of Sc in the relaxor ferroelectric properties still needs to be determined. There are several routes to explore this further. The most direct way to analyze this would be in bulk form. Sc could not be incorporated into the $SrTiO_3$ lattice through traditional oxide powder processing techniques. One alternative to the standard processing using powders of Sc_2O_3, TiO_2 and Sr_2CO_3 is to create powders of $SrTiO_3$ that are doped with Sc. This would eliminate any possible mixing problems involved in the standard mixed oxide route and ensure the thermodynamic equilibrium concentration is reached. There are several routes to accomplish this; using sol-gel would be one of the easiest since the chemistry is very flexible. This will ensure that Sc is stabilized within the $SrTiO_3$ lattice to the thermodynamic limits and allow for direct control of the Sc doping levels. Thus, this experiment would also allow for the determination of the thermodynamic solid solubility limit of Sc in $SrTiO_3$. This could be determined from x-ray diffraction measurements of the lattice constant for various doping levels. The doping level of Sc at which the lattice constant no longer changes would indicate the maximum solid solubility limit.

One approach to get beyond the thermodynamic limits would be to grow single crystals of Sc doped $SrTiO_3$. Single crystal growth would allow for the Sc to incorporated from the molten state at the liquidus, where typically the solid solubility is much higher. Once in the solid phase, diffusion is very limited and a higher concentration of Sc could be stabilized in the $SrTiO_3$ lattice. Ideally this material would be quenched down to lower

temperatures in order to limit diffusion. This type of crystal would be difficult to grow using the standard flame fusion method used for growth of most bulk $SrTiO_3$ crystals because the incorporation of Sc could not be regulated easily. A better crystal growth approach would be float zone. However, the exact doping levels will be hard to control since the crystal growth will most likely create a doping gradient in the crystal. This will necessitate the use of calibrated secondary ion mass spectroscopy (SIMS) for each of the samples examined. These standards could be made using ion-implantation of Sc into $SrTiO_3$ single crystal substrates.

An alternative to the bulk approach would require the deposition of intentionally Sc doped strained $SrTiO_3$ films. This could be done by co-deposition of Sc and Ti during the growth of $SrTiO_3$ by molecular beam epitaxy. In order to maintain the strain state, the same $DyScO_3$ substrates would be required. In order to characterize the Sc content SIMS will also have to be performed in this case since stoichiometry control by MBE is on the order of 1% and low doping levels are often even harder to control.

A different approach could also be taken along these same lines. A Sc doped $SrTiO_3$ film could be grown on $SrTiO_3$.Homoepitaxy would remove biaxial strain imparted by lattice mismatch of the substrate, and may allow for much larger amounts of Sc to be stabilized in the $SrTiO_3$ as compared to the ceramic. This experiment would enable determination of whether Sc^{3+} perturbs the quantum paraelectric state of SrTiO3. In particular it should be determined if there a peak in the dielectric constant at finite temperatures. It should be noted that it would be difficult to extract dielectric data from the sample using IDT electrodes, since there is no sharp boundary with a large dielectric contrast. The exact Sc profile would be dependent on the diffusion of the Sc between the

film and substrate; since they are the same material it presumably would be perceptible. A negative result in this case (no detectible change in the dielectric behavior of $SrTiO_3$) would not signify that Sc has no effect. In this case it could be that the IDT electrodes are not measuring the film but are averaging the film and substrate, and it would be impossible to separate the two.

Another possibility to determine examine the effects of Sc on $SrTiO_3$ is to perform Z-contrast TEM. This technique employs EELS with the atomic resolution of TEM to image a single atom and determine the composition of the atoms. This would enable the determination of the site occupancy of Sc. Sc has an ionization state of 3+ which falls between Sr^{2+} and Ti^{4+}, so it could be stabilized on either the A or B site in $SrTiO_3$. The size of the Sc atom is closer to the Ti atom suggesting that Sc should be on the B site of the atom. The Z-contrast TEM could directly image the site occupancy of the Sc atom and the distribution of the Sc in the $SrTiO_3$.

Strain has been shown to greatly affect the transition temperature of $SrTiO_3$ and other ferroelectric materials. With the advent of newer substrates, the ability to probe the shift in the transition temperature of other ferroelectric materials will be possible at several different strain states. Recently $SmScO_3$ and $NdScO_3$ have been made in single crystal form and presumably other ReScO_3 materials will be produced in the near future.[7] Other novel substrates are also being developed, such as $Sr(Li, Ta)O_3$ and $Sr(Al,Li,Ta)O_3$ (SALT) which have a pseudo cubic lattice constant that can be adjusted from 3.96 to 4.02 by adjusting the composition. This will allow for the systematic examination of the effects of strain on the dielectric properties. Through epitaxial growth the different strain state of many ferroelectric materials such as $BaTiO_3$ $BiMnO_3$, and $PbTiO_3$ can be

explored. With a range of substrates, the exact dependence of the ferroelectric transition temperatures on strain can be determined. Other incipient ferroelectric systems such as $CaTiO_3$ and $KTaO_3$ can also be investigated to determine the effects of strain on the ferroelectric properties of these materials.

The role of the asymmetric strain states on the ferroelectric property needs to be determined. In order to examine this, $SrTiO_3$ films need to be grown on two systems, one with a cubic and one with an orthorhombic lattice. Two substrates that satisfy this case are $KTaO_3$ and $SmScO_3$. $KTaO_3$ is a cubic crystal with a lattice parameter of 3.9883 Å and would yield a strain of 2.1%.[8] These $KTaO_3$ lattice constants are bracketed by the in-plane lattice constants for (101) $SmScO_3$, which are 3.9837 and 3.9943 Å and have an average strain of 2.1%. By growing films of $SrTiO_3$ on different substrates and comparing the properties as a function of angle for both films, a direct comparison of the effects of the anisotropic strain can be determined. This should yield a tetragonal prototype $SrTiO_3$ on $KTaO_3$ and a orthorhombic prototype $SrTiO_3$ film on $SmScO_3$. The difference in properties of these films would be interesting to investigate if polarization direction is changed as it typically does for a tetragonal to orthorhombic phase transition. However, these growths will not be straightforward. In order to use $KTaO_3$, a low growth temperature is needed to keep the volatile potassium in the crystal. An amorphous layer of $SrTiO_3$ could be deposited at low temperatures to "seal" the surface to prevent the loss of potassium from the substrate. It could subsequently be recrystalized when it is heated to growth temperature. Another problem is the larger lattice mismatch of $SrTiO_3$ and these substrates. Though $SrTiO_3$ was grown on $GdScO_3$ with a misfit strain of 1.6%, this mismatch is even larger with a strain of 2.1%. This will require the minimum growth

temperature be used and the film thickness to be kept low, probably below 250 Å.

Otherwise misfit dislocations will reduce the strain state of the films, making a direct

comparison difficult. Another option is to use $(Ba_{1-x}Sr_x)TiO_3$, through adjustment of the

Ba to Sr ratio the lattice parameter could be adjusted. Though, the Ba/Sr ratio be carefully

chosen so that the temperature of the phase transition is not shifted to high to be

measured and the lattice constant is big enough to allow for the growth of coherent films.

References

[1] S .N. Amanyan, E. V. Antipov, V.A. Antonov, P. A. Arsen'ev, Kh. S. Bagdasarov, A. M. Kevorkov, L. M. Kovba, and A. V. Rakhmatuli, Russ. J. Inorg. Chem. **32**, 1225 (1987) [Zh. Neog. Khim. **32**, 2087 (1987)].

[2] Landolt-Börnstein: Numerical Data and Functional Relationships in Science and Technology, edited by O. Madelung, M. Schulz, and H. Weiss (Springer, Berlin, 1982), New Series, Group III, Vol. 7b, p. 22.

[3] D. Taylor: Thermal expansion data VIII. Complex Oxides, ABO_3, the perovskites *Trans. J. Br. Ceram. Soc.* **84**, 181 (1985).

[4] J. P. Maria, Ph.D. Thesis, The Pennsylvania State University, 1998.

[5] J. H. Haeni, P. Irvin, W. Chang, R. Uecker, P. Reiche, Y. L. Li, S. Choudhury, W. Tian, M. E. Hawley, B. Craigo, A. K. Tagantsev, X. Q. Pan, S. K. Streiffer, L. Q. Chen, S. W. Kirchoefer, J. Levy, and D. G. Schlom, Nature **430**, 758 (2004).

[6] S. T. Misture, J. C. Hicks, E. A. Payzant, C. R. Hubbard, C. T. Blue, and S. M. Pilgrim, Appl. Phys. Lett. **72**, 1042 (1998).

[7] Private communication D.G. Schlom and R. Uecker.

[8] E. A. Zhurova, Y. Ivanov. V. Zavodnik, and V. Tsirelson, Acta. Crys. **B56**, 594 (2000).

VITA

Michael David Biegalski

Michael David Biegalski was born in Silver Spring, Maryland on Octorber 24th, 1976 to

Robert and Sharron Biegalski.

EDUCATION:

➢ *Doctor of Philosophy*, Materials Science and Engineering, (May 2006)
   The Pennsylvania State University

➢ *Master of Science*, Materials Science and Engineering, (2001)
   The Pennsylvania State University
   Thesis: "Optical Characterization of Reliability in Capacitor Materials"

➢ *Bachelor of Science*, Ceramic Engineering, (1998)
   University of Illinois, Champaign-Urbana;
   Thesis: "Synthesis of Barium Orthotitanate Through New Complex
   Polermization Route"

SELECTED PUBLICATIONS:

1. **M.D. Biegalski**, W. Tian, M. E. Hawley, D.D. Fong, J.A. Eastman, P.H. Fuoss, R. Uecker, P. Reiche, W. Chang, S.K. Streiffer, D. G. Schlom, and S. Trolier-McKinstry, "Structure and critical thickness of $SrTiO_3$ films grown on (101) $DyScO_3$," Submitted to J. Appl. Phys.
2. Y.L. Li, S. Choudhury, **M.D. Biegalski**, J.H. Haeni, A. Vasudevarao, A. Sharan, H. Z. Ma, J.Levy, V. Gopalan, S. Trolier-McKinstry, D. G. Schlom, Q. X. Jia, and L. Q. Chen, "Phase transitions and domain structures in strained pseudocubic (001) $SrTiO3$ thin films," submitted to Phys. Rev. B.
3. **M.D. Biegalski**, A.K Tagantsev, R. Uecker, P. Reiche, W. Chang, S. W. Kirchoefer, S.K. Streiffer, D. G. Schlom, and S. Trolier-McKinstry, "Relaxor Ferroelectricity in Strained Epitaxial $SrTiO_3$ Thin Films on $DyScO_3$ Substrates," Accepted in Appl. Phys. Lett.
4. **M.D. Biegalski**, J.H. Haeni, C.D. Brandle, A.J. Ven Graitis, S. Trolier-McKinstry, and D.G. Schlom, "Thermal expansion of the new perovskite substrates $DyScO_3$ and $GdScO_3$," J. Mater. Res. **20**, 952 (2005).
5. **M.D. Biegalski** and S. Trolier-Mckinstry, "Modeling Optical Changes in Perovskite Capacitor Materials Due to dc-Field Degradation," J. Am. Ceram Soc. **88**, 71 (2005).
6. K. J. Choi, **M.D. Biegalski**, Y. L. Li, A. Sharan, J. Schubert, R. Uecker, P. Reiche, Y. B. Chen, X. Q. Pan, V. Gopalan, L.-Q. Chen, D. G. Schlom, and C. B. Eom, "Enhancement of Ferroelectricity in Strained $BaTiO_3$ Thin Films," Science **306**, 1005 (2004).